

3-Dimensional Ultrasound Imaging for Medical Telesonography: Algorithms and Architectures

THÈSE N° 9019 (2018)

PRÉSENTÉE LE 13 DÉCEMBRE 2018
À LA FACULTÉ INFORMATIQUE ET COMMUNICATIONS
LABORATOIRE DES SYSTÈMES INTÉGRÉS (IC/STI)
PROGRAMME DOCTORAL EN GÉNIE ÉLECTRIQUE

ÉCOLE POLYTECHNIQUE FÉDÉRALE DE LAUSANNE

POUR L'OBTENTION DU GRADE DE DOCTEUR ÈS SCIENCES

PAR

Aya Mohamed Naguib Ahmed IBRAHIM

acceptée sur proposition du jury:

Prof. J.-Ph. Thiran, président du jury
Prof. G. De Micheli, Dr F. Angiolini, directeurs de thèse
Prof. M. Ghovanloo, rapporteur
Prof. M. Huebner, rapporteur
Prof. A. Burg, rapporteur



ÉCOLE POLYTECHNIQUE
FÉDÉRALE DE LAUSANNE

Suisse
2018

Strength does not come from physical capacity.

It comes from an indomitable will.

— Mohandas Karamchand Gandhi

To my son Younis,

To my parents.

Acknowledgements

Although the world is full of strife and individuals with deformed ethics, there are always many people who are there to support, encourage, and give delight. During the past 4 years in my life, my Ph.D. journey, I have been blessed meeting many of the later. I truly owe them what I have accomplished. It is all thanks to the *God* will.

My first gratitude goes to *Prof. Giovanni De Micheli (Nanni)*, my thesis director, for his valuable guidance, useful critiques, and precious knowledge gained under his supervision. I would like to express my deep appreciation to *Nanni* not only in giving me the opportunity to conduct that research but also in his strong support and fatherly care during all the challenges I had to overcome.

My second appreciation goes to *Dr. Federico Angiolini*, my co-director, for all what I have learned from him, which are many, and his constant and constructive supervision. He has always been my reference and encyclopedia; from the effective writing to the hardware design.

I would like to thank my thesis jury members; *Prof. Jean-Phillipe Thiran*, *Prof. Andreas Burg*, *Prof. Maysam Ghovanloo*, and *Prof. Michael Huebner*, for accepting being the examiners of my thesis and evaluating my research.

My deep gratitude goes to *Dr. Marcel Arditi* for the rich discussion, precious information, knowledge, and ideas in ultrasound physics. I also thank Marcel for his French translation of the abstract of my thesis. I would like to acknowledge *Ahmet Yüzügüler*, *William Simon*, *Damien Doy*, *Eliéva Pignat*, *Chiara Ercolani*, and *Claudio Loureiro*, the very inspiring and keen students, for their contribution in that work and for what I even learned from them.

I would also like to acknowledge the Swiss Confederation funding of this research through the *UltrasoundToGo* project of the *Nano-Tera.ch* initiative.

Being in a workplace full of scientifically inspiring people with a friendly temperament is a bless. It is the *Integrated Systems Laboratory (LSI)* and its astonishing people. I would like to express my deep gratitude to *Christina Govoni* for all of her administrative effort, motherly care, and distinctive laugh that always gives a lusty feeling. A sincere thankfulness to *Prof. Sandro Carrara* for his precious advices and genuine vision in life. My acknowledgement goes to the recent enthusiastic LSler *Carole Burget*, the administrative manager, for her effort during the

Acknowledgements

last period in my Ph.D.. Thanks should also go to *Rodolphe Buret*, the IT manager, for his hard work in maintaining our servers and machines in order to pave our way for efficient research conductivity. My warm gratitude goes to *Francesca Criscuolo*, my friend and officemate, for all the nice discussions, joyful moments, and even the share of the aging symptoms (a joke). I am very grateful to *Francesca Stradolini*, for her moral support, care, and share of both joyful and difficult moments. I sincerely thank *Tugba Kilic*, for the inspiring discussions and beautiful period we spent. I have not only got few friends from LSI but many. A special thankfulness goes to *Eleonora Testa*, *Maxime Thammasack*, *Ivan Ny Hanitra*, *Giovanni Resta*, *Ioulia Tzouvadaki*, *Eda Mehmeti*, and *Nadezda Pankratova*.

I am extremely grateful to the Arabian community in Switzerland, especially, *Madame Soaad*, *Nesrine*, *Madame Naima*, *Mariam*, *Shereen*, and *Sarah* not only for their friendship that made me feel home but also for their undeniable help with Younis (my son), either by direct care - while I was working until late and traveling for scientific events - or by upbringing advices.

A warm appreciation goes to my family for their love and constant encouragement. A deep "thank you" goes to *Eman Ayman* for her true friendship that eliminates any distance. We are sisters from different parents.

To my mother, *Masrrat Swailam*, the lady who crafted and taught me how to be persistent and strong in following my dreams, a "thank you" is never enough. Her unconditional love, great values, and belief in me are the fuel that never fail on recharging my will, renewing my ambition, and strengthen my patience in facing life. To my father, *Mohamed Naguib*, r.i.p., the person who was my model and inspiration in following the engineering study, thank you and may Allah rest your soul in peace.

Last but not least, I would like to thank the little creature who has brought me happiness and defined me another dimension in love, my son; *Younis (Yoky)*. This little being, who arrived my life few months after the start of my Ph.D., is my renewable motivation and undimmed thrill. Thank you *Yoky* for your smiles that never fail in drawing me smiles.

Lausanne, 14 September 2018

Aya Ibrahim

Abstract

Enabling telemedicine in *Ultrasound (US)* imaging, i.e. *telesonography*, is until today just a wish. Although US has incomparable advantages such as safety in use, lower cost and complexity, and capability to be utilized in many applications (cardiology, obstetrics, angiology, etc.), it is limited in use to hospitals and sonographer cabinets. Medical US has not been available yet in many situations of need. For example, a patient with a cardiac complication on a ship or aircraft may lose his life due to the impossibility to perform a scan on-site and get a remote diagnosis quickly. Even rescue vehicles and helicopters have not been equipped yet with US device that can be operated by a basic trained paramedic. Populations in isolated remote areas seldom enjoy access to sonographers, and are in a serious necessity to unlock telesonography with an affordable (solving the typical low medical-equipment budget) and battery operated (working around the common electricity cut-offs problem or lack thereof) mean.

The high reliance on the presence of a trained sonographer to perform the scan is the main reason behind this shortcoming. A sonographer is required to move the probe on the body based on high experience, fine precision, and learned technique until reaching the diagnosis on-the-spot.

3D US lifts this limitation by imaging the whole volume under the probe at once, and accordingly allows the decoupling of the acquisition from the diagnosis. Therefore, any untrained person on-site can acquire 3D scans and send the reconstructions to a hospital for diagnosis. However, today's 3D systems only suit well-equipped hospitals due to their high requirements in size, power, and cost. In order to solve the root of this vicious cycle, there is a need for a medical US system that supports 3D imaging, is compact and power efficient.

This thesis is a step towards solving this problem. An unprecedented *single-FPGA 3D* medical US imaging system with a *5 W consumption* has been proposed. Our imaging system features: (i) 1024 channel of independent information processing (state-of-the-art), (ii) two input means: realtime data via optical connection with a US transducer, and offline data via Ethernet, (iii) complete digital processing platform from the receive of the digitized raw data until the rendering of the reconstruction on a screen, (iv) three common US imaging modes for image enhancement flexibility at the cost of the frame rate, (v) extreme scalability: downscaling for 2D imaging, or further upscaling on a resources-capable FPGA, and (vi) high-definition live

Abstract

video output of the scans. We have developed a prototype whose size is currently $26.7\text{cm} \times 14\text{cm} \times 0.16\text{cm}$. The material cost is less than 4000\$, with a path to further reduction by implementing a custom board around the FPGA for mass production, instead of the off-the-shelf development board. This compares very favorably to current commercial 3D systems, which cost $\sim 100\text{K}\$$ for the imaging system only.

Moreover, in order to bridge the gap arising from the decoupling of the scanning process from the interpretation by an US radiologist, two solutions have been proposed: (i) automatic probe localization module using gyroscopes and accelerometers, and (ii) a mobile application for probe positioning guidance for common US scans.

Our contributions have been consolidated to successfully achieve the aimed target of a *first* telesonography-capable prototype allowing the usage of medical US anywhere and by any personnel, with major societal benefits.

Keywords: Ultrasound imaging, Volumetric sonography, Image reconstruction, Telesonography, Digital beamforming, Delay calculation, Apodization, Scan-conversion, Field programmable gate arrays (FPGA), Ultrasound quality metrics.

Résumé

L'extension de la télémédecine à l'échographie, qu'on pourrait appeler *télésonographie*, reste à ce jour un projet non-réalisé. L'échographie, qui recourt à la technologie des *Ultrasons (US)*, a de nombreux avantages, tels que la sécurité d'emploi (en l'absence de tout rayonnement ionisant), un coût et une complexité faibles, ainsi que la capacité de se déployer dans de nombreuses indications (cardiologie, obstétrique, angiologie, etc.), reste pour l'essentiel cantonnée à l'utilisation en milieux hospitalier et des cabinets d'imagerie médicale. L'échographie n'a pas encore trouvé sa place dans de nombreuses situations où elle s'avérerait utile. Par exemple, un patient présentant une complication cardiaque à bord d'un navire ou d'un avion pourrait perdre la vie, en l'absence de matériel permettant une imagerie rapide et un diagnostic à distance par un médecin compétent. Même les ambulances ou hélicoptères d'urgence médicale ne sont pas systématiquement équipés de systèmes d'échographie, qui pourraient pourtant être facilement utilisés par des intervenants para-médicaux ayant reçu un entraînement adéquat. De même, les populations rurales ou en milieu isolé n'ont que très rarement un accès à l'échographie, et bénéficieraient grandement de systèmes de télésonographie de faible coût (en raison de budgets limités) et/ou opérant sur batterie (pour faire face à des coupures de courant dans certaines régions).

La nécessité impérieuse d'un technicien ou médecin spécialisé en échographie, présent au côté du patient, est l'une des raisons de la situation actuelle. L'habileté d'un tel opérateur pour accomplir les gestes exigés par cette modalité d'imagerie est cruciale pour atteindre un diagnostic rapide et précis, et requiert une grande expérience, précision et un long apprentissage.

L'échographie volumétrique (3D US) permet en quelque sorte de contourner cette limitation, en découplant les phases d'acquisition des images et celle de leur interprétation : ainsi, un volume entier sous la sonde peut être enregistré par un opérateur peu qualifié, et les données ainsi acquises peuvent être envoyées à un hôpital pour interprétation et établissement d'un diagnostic par un médecin hautement qualifié. Malheureusement, les systèmes 3D US sont à l'heure actuelle cantonnés à peu de centres médicaux, bien équipés, en raison de leur grande taille, la puissance requise et leur coût élevé. Pour vaincre cet obstacle, il existe un clair besoin d'un système d'échographie médicale permettant une acquisition 3D en temps réel, et qui soit compact, efficace et peu coûteux.

La présente thèse représente un pas vers la résolution de ce problème. Nous y proposons un système d'échographie 3D basé sur *un seul FPGA*, nécessitant une *consommation électrique*

Résumé

de 5W seulement. Les caractéristiques de notre système d'imagerie sont : (i) 1024 canaux indépendants de traitement de l'information (état de l'art) ; (ii) deux moyens d'entrée : données en temps réel par canal optique en provenance d'une sonde d'échographie, et données hors ligne par une connexion Ethernet ; (iii) plateforme complète de traitement numérique, depuis la réception des données brutes d'échos numérisés jusqu'au rendu 2D après reconstruction sur un moniteur de visualisation ; (iv) trois modes d'imagerie échographique, présentant une flexibilité graduée entre une qualité supérieure de reconstruction au prix d'une cadence d'imagerie réduite ; (v) adaptabilité extrême : adaptation aux exigences réduites de la 2D, ou au contraire adaptation à des FPGA aux ressources étendues ; (vi) rendu vidéo haute définition des images en temps réel. Nous avons ainsi développé un prototype dont la taille est actuellement de 26.7 cm × 14 cm × 0.16 cm. Le coût du matériel est inférieur à \$4'000, avec une marge de réduction substantielle par l'implémentation d'une carte customisée autour du FPGA pour une production de masse, en remplacement de la carte standard de développement. Ce prototype se compare donc très favorablement aux systèmes 3D commerciaux existants, dont le coût avoisine \$100K pour l'imagerie seule.

De plus, deux solutions ont été proposées pour pallier les problèmes introduits par le découplage entre l'acquisition des images par un technicien de leur interprétation par un radiologue spécialiste en échographie : (i) un module de localisation automatique de la sonde recourant à des gyroscopes et/ou accéléromètres, et (ii) une application mobile pour le guidage de positionnement de sonde à distance pour les examens les plus répandus.

Nos contributions ont été concrétisées par la réalisation d'un premier prototype échographique compatible avec la télésonographie, ouvrant ainsi la voie à l'utilisation de l'échographie médicale n'importe où et par du personnel non-qualifié, avec des perspectives d'impact sociétal important.

Mots-clés : Échographie, L'échographie volumétrique, Reconstruction d'image, Télésonographie, Beamforming numérique, Calcul de délai, Apodisation, Conversion de numérisation, Circuit logique programmable, Mesure de la qualité des ultrasons.

Contents

Acknowledgements	v
Abstract (English/Français)	vii
List of Figures	xx
List of Tables	xxi
List of Acronyms	xxii
1 Introduction	1
1.1 Ultrasound Imaging Working Principle	3
1.2 Ultrasound System Specifications	5
1.3 Telesonography Challenges	5
1.3.1 Challenge 1: Transducer-Processing System Interfacing, and Input Bandwidth and Memory Requirements for the Samples	6
1.3.2 Challenge 2: Beamforming Resolution	7
1.3.3 Challenge 3: Realtime Beamforming Computation Load	7
1.3.4 Challenge 4: Memory Requirements and Access Bandwidth to The Beamforming Coefficients	8
1.3.5 Challenge 5: Post-Processing Computation Load	8
1.3.6 Challenge 6: Probe Positioning and Scans Labeling By Untrained Operator	8
1.3.7 Challenge 7: Reconstructed Volumes Transmission	9
1.4 Novel Contributions	9
1.5 Thesis Outlines	10
2 Background and Previous Work	13
2.1 Ultrasound Transducers and Beam Profiles	13
2.2 Ultrasound Processing, Reconstruction, and Terminologies	15
2.3 Common Ultrasound Imaging Modes	20
2.3.1 Conventional Imaging	20
2.3.2 Ultrafast Imaging	20
2.3.3 Zone Imaging	20
2.3.4 Compound Imaging	22
2.3.5 Tissue Harmonic Imaging	22

Contents

2.3.6 Synthetic Aperture Imaging	23
2.4 Literature Review and Previous Work	23
2.5 Summary	26
3 Matlab-based Imaging Pipeline and Algorithms Investigation	27
3.1 Active-Elements Pattern in Receive	30
3.2 Phased Arrays and Zone Imaging	32
3.3 3D Reconstruction Resolution and Element Count	34
3.4 Summary	35
4 SHEDA - Steering-based Hardware-Efficient Delay Approximation Calculator	37
4.1 Working Principle	38
4.1.1 Receive Delay	38
4.1.2 Transmit Delay	40
4.2 Accuracy Bound	41
4.3 FPGA Architecture	42
4.4 SHEDA Accuracy Evaluation	44
4.4.1 Accuracy Bound Evaluation	44
4.4.2 Point Spread Function (PSF) Evaluation	46
4.4.3 Fixed-Point Representation Inaccuracy	47
4.4.4 Visual Assessment	47
4.5 Summary	49
5 Pre-Processing Optimization and Other Beamformer Logic	51
5.1 Apodization	52
5.1.1 SCA - SHEDA-Correction Apodization Scheme	53
5.1.2 Static Apodization Scheme	60
5.2 Time-Gain Compensation	61
5.3 Beamformer Processing Order and Input-Memory Mapping	62
5.4 The Beamformer Summation	64
5.5 Summary	64
6 Post-Processing Optimization And Imaging Mode Support	67
6.1 Demodulation	68
6.2 Log-Compression, Cross-Sectional Scan-Conversion, and HDMI Support . . .	68
6.3 Imaging Modes: SIRI, Zone Imaging, and Compound Imaging	70
6.3.1 Single-Insonification Reconstruction Imaging (SIRI)	70
6.3.2 Zone Imaging	70
6.3.3 Compound Imaging	71
6.4 System Quality Evaluation In Different Modes	72
6.4.1 Point-Spread Function (PSF)	72
6.4.2 Peak-Signal-To-Noise Ratio (PSNR)	73
6.4.3 Contrast Ratio (CR)	75

6.4.4	Visual Assessment	76
6.5	Summary	79
7	I/O Interfacing, System Communication, Probe Localization, and Platform Results	81
7.1	Optical Connection With a Probe	82
7.2	Ethernet	83
7.3	Data Representation	84
7.4	FPGA, MicroBlaze, and GUI Communication	85
7.5	Platform Self-Bootability	86
7.6	Probe Positioning Guidance - Bridging the Telesonography Gap	86
7.6.1	Automatic Probe Localization - IMU	87
7.6.2	Android Application For Operator Guidance	88
7.7	Single-FPGA Digital Imager Evaluation	90
7.7.1	FPGA Utilization Results	90
7.7.2	Performance	91
7.7.3	Quality Assessment	91
7.7.4	Platform Portability and Estimated Cost	92
7.8	Summary	93
8	Conclusion and Future Directions	95
8.1	Future Directions	97
	Appendices	99
A	SHEDA Error Bound	101
A.1	Lagrange Error Bound	101
A.2	Finite Error Bound	103
B	SCA Mathematical Model	107
	Bibliography	124
	Curriculum Vitae	125

List of Figures

1.1	Three different contemporary volumetric US scanners. (a) Samsung WS80a, picture from [1]. (b) Philips EPIQ 7, picture from [2]. (c) GE Voluson E10, picture from [3].	2
1.2	The US insonification process. The two-way time-of-flight of US is the time taken by the wave to be transmitted from an origin O to a scatterer S and reflected back to each transducer element D . The transmitted beam is in red, and the backscattered beam is in green.	4
1.3	2D versus 3D imaging. Left: array probe insonifying and acquiring a cross-section of the human body. Right: matrix probe insonifying and acquiring a quasi-pyramidal volume of the human body. Picture from [4].	4
1.4	Workflows enabled by the proposed telesonographic imager.	9
2.1	Examples of US array probes and of their acoustic emission. Left: linear array; center: phased array; right: convex array. Probe pictures from the Philips catalog [5].	14
2.2	3D US imaging probes. Left: matrix probe. Right: mechanically sweeping probe. Probe picture from [6].	15
2.3	Different transmit focusing options. The transducer is at the top of the figures. (a) Plane wave, using a 192-element <i>linear</i> probe. (b) Converging wave, using a 16-element <i>phased</i> probe. (c) Diverging wave, using a 16-element <i>phased</i> probe.	15
2.4	Architectural diagram of a generic ultrasound imaging system, with focus on the beamformer processing the sampled RF radio-frequency signals. N is the number of transducer matrix elements, N_k is the number of voxels per cycle the BFU can produce, and $ V $ is the number of focal points to be computed.	17
2.5	For a synthetic phantom comprising six punctiform scatterers (a), an image can be reconstructed by simulating a linear array and imaging a rectangular region (b), or a phased array and imaging a circular sector (c) and (d). (c) the beamformed sector, still in polar coordinates; (d) the same sector after scan conversion.	19
2.6	Logical processing flowchart of the US image reconstruction pipeline.	19

List of Figures

2.7	A sketch depicting the difference between zone and compound imaging in terms of the reconstruction mechanism. (a) In zone imaging, the output image is reconstructed by stitching the reconstructions of non-overlapping zones of the ROI, while (b) in compound imaging, the image is reconstructed based on compounding multiple reconstructions of the whole ROI, i.e. <i>full overlapping</i> between the contributing zones compared to zone imaging.	21
2.8	Example of possible focused beams for zone imaging, where five zones are insonified in sequence.	22
3.1	Our Matlab-based US imaging pipeline. (a) 2D linear imaging pipeline using <i>1D linear</i> array transducer. (b) 2D/3D phased imaging pipeline using <i>1D/2D phased</i> array transducer.	28
3.2	The workflow between our Matlab-based imaging pipeline and the single-FPGA design. Digital echoes in addition to other pre-defined tables are provided by our Matlab design to the single-FPGA imager. The Matlab pipeline provides a golden reference for the assessment of our single-FPGA imaging quality.	29
3.3	Reconstructions based on different number and pattern of <i>active</i> transducer elements in receive, and the consequent quality impact. (a) 96 out of 96. (b) central 32 out of 96. (c) central 16 out of 96. (d) 1 every 3. (e) 6 every 16. (f) 12 every 32. A 96-element linear array probe is used of $f_o = 3.5$ MHz and the echoes are sampled at $f_s = 200$ MHz. The full aperture is active in transmit.	31
3.4	Phased reconstruction with focused and diverging insonification profiles, for single-zone and multi-zone imaging; (a)-(c): single insonification per frame; (d)-(h): zone imaging of 2-50 zones, each is a circular sector. (a) Focused Tx. (b) Focused Tx, with intensity compensation. (c) Diverging Tx. (d)-(h) Zone imaging of 2, 3, 5, 10, and 50 zones, respectively, while employing focused insonification profiles.	33
3.5	3D imaging with a 16x16 matrix phased array, and a variable number of beam-formed points in the axial direction; (a) 500 points, (b) 100 points, and (c) 50 points. The images show the middle transverse plane (azimuth-radial plane) of the reconstructed 3D volume.	35
3.6	3D imaging with (a) 16x16 and (b) 32x32 matrix phased probes. The images show the middle transverse plane (azimuth-radial plane) of the reconstructed volume.	36
4.1	Logical processing flowchart of the US image reconstruction pipeline.	37

4.2	(a) Propagation delays must be calculated between each S and each element D of the transducer. The reference delays are the delay values for points R on the Z axis. For a point on another line of sight, the delay can be computed from the reference delay table plus an angle-dependent offset. (b) When considering both θ and ϕ steering, the required compensation is a plane, whose inclination around the origin is a function of θ, ϕ . (c) A section of the compensated delay table for a steering angle, where the x-axis indicates the depth in time samples and the y-axis represents the probe elements in the azimuth direction. The color-map represents the two-way delay values.	38
4.3	The SHEDA-based delay-calculation architecture. (a) Rx delays are computed by adding the two steering coefficients c_1 and c_2 to exactly-calculated reference delays. (b) Tx delay calculator, which is based on Xilinx CORDIC IP. The sum of Tx and Rx delays is used to index the input samples in the BRAMs of Figure 5.11.	43
4.4	Graphical depiction of the geometric approximation in SHEDA approach. (a) Geometric inaccuracy of the approach. The inaccuracy is significant only very close to the probe and at broad angles. (b) Geometric inaccuracy after applying dynamic apodization (Section 5.1). The color map represents the percentage (0 = 0% and 1 = 100%) of elements that incur delay inaccuracy of more than the constructive interference threshold of 2 samples.	45
4.5	Locations of scatterers being reconstructed to test PSF contours and projections (Figure 4.6). The locations are overlaid on the inaccuracy map of Figure 4.4(b).	47
4.6	The evaluation for the SHEDA calculation approach based on simulating PSF contours and their projections for different scatterer location, where (a), (f) for a scatterer S_1 at $\theta = 0^\circ$, $\phi = 0^\circ$, $r = 12\text{mm}$, (b), and (g) for a scatterer S_2 at $\theta = -32^\circ$, $\phi = 0^\circ$, $r = 12\text{mm}$, (c) and (h) for a scatterer S_3 at $\theta = 0^\circ$, $\phi = 0^\circ$, $r = 100\text{mm}$, (d) and (i) for a scatterer S_4 at $\theta = -32^\circ$, $\phi = 0^\circ$, $r = 100\text{mm}$, (e) and (j) for a scatterer S_5 at $\theta = -32^\circ$, $\phi = -32^\circ$, $r = 48.1\text{mm}$. The blue curves represent the exact non-optimized delay calculation, while the red ones represent the SHEDA calculation.	48
4.7	2D imaging of a kidney phantom available online on the Field II website [7]. The reconstruction is composed of 8 zones, each insonified by different diverging-beam insonifications. The imaging depth is 10 cm and the azimuth sector is 73° wide. (a) SHEDA calculation method; (b) exact calculation method. On close inspection, the speckle pattern close to the transducer and at the edges of the imaging cone displays only minor differences.	48
5.1	Logical processing flowchart of the US image reconstruction pipeline.	51
5.2	The "dynamic" apodization function plot (i.e. "expanding-aperture" apodization in radial direction). The color coding represents the apodization weighting. The transducer is at the top of the figures. For simplicity and easy visualization, we have plotted the apodization functions for the 64-element probe of the 2D imaging design. The apodization weighting is modeled as a Hanning function.	53

List of Figures

- 5.3 Inaccuracy of the delay calculation towards each element of the probe; the chart represents the probe face, and the color shade describes the calculation inaccuracy at that element D expressed in sampling periods, from a voxel S at ($r = 8\text{ mm}$, $\theta = -28^\circ$, $\phi = -3^\circ$). Blue = error of less than 1 delay sample, red = error of 8 samples. The contour line (magenta) defines the profile of the elements incurring an inaccuracy of ≤ 2 samples, i.e. the split between constructive and destructive contribution. White rectangle: standard expanding apodization window; black rectangle: apodization window derived in this work. Note how the latter window tracks more closely the 2-sample contour. 55
- 5.4 The inaccuracy in delay calculation becomes negligible by discarding all the echoes from elements that incur more than 2 samples of calculation inaccuracy. The plot shows, for each voxel S on the XZ plane of the image, the percentage (0 = 0% and 1 = 100%) of such elements when using the proposed tighter apodization. The color bar A significant inaccuracy reduction can be noticed compared to Figure 4.4(a) and 4.4(b). 57
- 5.5 Evaluation of our SCA scheme versus dynamic apodization in terms of PSF contours and projections for a scatterer at $\theta = -17^\circ$, $\phi = -3^\circ$, $r = 12\text{ mm}$. This is achieved by testing the reconstruction that is based on : (a) and (d) exact delay calculation while using expanding apodization (golden reference), (b) and (e) SHEDA delay calculation while using also expanding apodization, and (c) and (f) SHEDA delay calculation while using the SCA model. The PSF contour colors represent the level in dB, in a range of -5 dB, -10 dB, -20 dB, -30 dB, -40 dB from inside to outside. 58
- 5.6 Evaluation of our SCA scheme versus dynamic apodization in terms of PSF contours and projections for a scatterer at $\theta = -20^\circ$, $\phi = 0^\circ$, $r = 15\text{ mm}$. This is achieved by testing the reconstruction that is based on : (a) and (d) exact delay calculation while using expanding apodization (golden reference), (b) and (e) SHEDA delay calculation while using also expanding apodization, and (c) and (f) SHEDA delay calculation while using the SCA model. The PSF contour colors represent the level in dB, in a range of -5 dB, -10 dB, -20 dB, -30 dB, -40 dB from inside to outside. 59
- 5.7 3D imaging of a fetus phantom provided online while [8] using (a) expanding apodization, or (b) SCA *square* model. 60
- 5.8 The static apodization function plot (the one implemented on our single FPGA) versus the radial-dynamic one depicted in Figure 5.2. The color coding represents the apodization weighting. The transducer is at the top of the figures. For simplicity and easy visualization, we have plotted the apodization functions for the 64-element probe of the 2D imaging design. The apodization weighting is modeled as a Hanning function. 61
- 5.9 TGC function plot (linear scale) for different time samples (i.e. imaging depth). It is an exponential growth representing the relation between the compensation of the signal versus the traveling time (or depth). 62

5.10 Focal point calculation order in a nappe-oriented beamformer: all points at a given depth are calculated; then the depth is incremented. A scanline is also shown for comparison; a scanline-oriented beamformer will reconstruct points along the whole scanline, then move to the next. The 1, 2, and 3 directions represent the radial (i.e. depth), elevation, and azimuth directions, respectively. Figure copied from [9]	63
5.11 An abstracted architecture diagram of the proposed US Imager. The orange blocks represent the beamformer which comprises the TGC, the apodization, the BRAMs containing the input weighted samples, the delay calculator, and the adder tree units. The beamformer blocks are covered in both Chapter 4 and 5. .	64
5.12 The logical processing flowchart of the US image reconstruction pipeline (like Figure 2.6) colored according to the color-map of Figure 5.11.	65
6.1 Logical processing flowchart of the US image reconstruction pipeline.	67
6.2 The block diagram of the simple demodulation method implemented on our single-FPGA imager. The method relies on calculating the absolute value of the beamformed voxels, then buffering them, and finally detecting the envelope by applying a LPF realized as an FIR filter.	69
6.3 A sketch depicting two different ways of dividing <i>virtually</i> the ROI in zone imaging; (a) the 6 zones are in the azimuth direction, and (b) the 6 zones are in the radial direction. This yields lateral or radial resolution improvements, respectively.	71
6.4 Evaluation of our zone imaging implementation versus SIRI in terms of PSF contours and projections for a scatterer at $\theta = 0^\circ$, $\phi = 0^\circ$, $r = 60$ mm. This is achieved by testing the reconstruction when dividing the ROI into, (a) and (e) SIRI, (b) and (f) 2×2 zones, (c) and (g) 4×4 zones, (d) and (h) 8×8 zones. The PSF contour colors represent the level in dB, in a range of -5 dB, -10 dB, -20 dB, -30 dB, -40 dB from inside to outside.	73
6.5 Evaluation of our zone imaging implementation versus SIRI in terms of PSF contours and projections for a scatterer at $\theta = -15^\circ$, $\phi = 0^\circ$, $r = 60$ mm. This is achieved by testing the reconstruction when dividing the ROI into, (a) and (e) SIRI, (b) and (f) 2×2 zones, (c) and (g) 4×4 zones, (d) and (h) 8×8 zones. The PSF contour colors represent the level in dB, in a range of -5 dB, -10 dB, -20 dB, -30 dB, -40 dB from inside to outside.	74
6.6 Our 6-cyst phantom. (a): sketch depicting the geometry of the phantom. (b): phantom reconstruction using phased imaging based on 8 zones diverging insonification.	74
6.7 3D imaging of a fetus phantom available online on the Field II website [8]. The images show the middle azimuth-depth plane (i.e. middle elevation plane) of the reconstructed volume by our imager. The imaging volume is $73^\circ \times 73^\circ \times 10$ cm. (a) is a single-zone image, i.e. SIRI, based on a single diverging beam insonification, while (b) is an 8×8 zone image, where each zone is insonified independently with a more focused beam.	77

List of Figures

6.8	3D imaging of a fetus phantom available online on the Field II website [8]. The images show the middle azimuth-depth plane (i.e. middle elevation plane) of the volume reconstructed by our imager. The imaging volume is $73^o \times 73^o \times 10cm$. (a): single frame, i.e. SIRI. (b) to (d): 3-frame, 5-frame, and 9-frame compounded images, using the <i>average</i> operator. (e): 9-frame compounded image using the <i>average-excluding-the-brightest-voxel</i> operator.	78
7.1	Logical processing flowchart of the US image reconstruction pipeline.	81
7.2	The optical connection between our US digital processor and the LightProbe probe [10], while utilizing a Mezzanine board as an interfacing between the units. The LightProbe is a 1D probe for proof-of-concept and to be replaced with a matrix probe whenever available.	83
7.3	Setup of the design for 2D and 3D US imaging. The components in the dashed box to the left are for development, debugging and verification only.	84
7.4	A screen-shot of our C#-based GUI. Different imaging modes' and SC settings can be specified via the GUI, which then communicates with the MicroBlaze and the FPGA.	86
7.5	The logic of controlling different imaging modes. The communication between the FPGA, the MicroBlaze, and the GUI to handle different options and settings of the processing flow.	87
7.6	Sample shots of the probe positioning charts provided by our android application for common US scans; (a) abdomen scan, and (b) liver scan. The body-view pictures are taken from [11]	89
A.1	The plot of the exact function $\sqrt{1+x}$ (dashed blue) and its first-order Taylor approximation $1 + \frac{1}{2}x$ (solid red) for $x \geq -1$	104
A.2	The plot of the $\sin\theta + \sin\phi\cos\theta$ function versus θ and ϕ	105

List of Tables

1.1	System Specifications	5
3.1	Runtime of the imaging flow (BF and SC) for different elements count in receive and array probe types.	32
3.2	3D BF runtime as a function of the desired axial resolution. 11688 is the maximum possible resolution, by reconstructing a pixel for every time sample of the input echoes, considering the f_s and imaging depth of this experiment (45 mm).	34
5.1	Count of elements that are apodized away by different apodization functions; for the remaining elements, count of the elements that experience accurate or inaccurate delay calculation (threshold = 2 sampling periods of inaccuracy). Memory buffer size required to store the corresponding apodization functions, e.g. 2D Hanning functions, considering a precision of 16-bit representation.	56
6.1	PSNR For Compound Imaging And SIRI. * <i>Reference volume: 9-frame compounding using averaging operator and based on exact delay calculation BF</i>	75
6.2	CR For Compound Imaging and SIRI.	76
6.3	CR For Zone Imaging and SIRI.	76
7.1	Imager Resource Utilization. * <i>Kintex UltraScale KU040 implementation results.</i> ** <i>Virtex UltraScale VU190 extrapolated results.</i>	90
7.2	Imager performance scaling in different imaging modes. * <i>Insonification time for a single emission.</i> ** <i>BF rate for a single ROI, either volume or image, reconstruction.</i> *** <i>SC rate for a single frame.</i>	92

List of Acronyms

A

ADC	Analog-to-Digital Converter
AFE	Analog Front-End
AXI	Advanced Extensible Interface
AHRS	Attitude and Heading Reference System
ASIC	Application-Specific Integrated Circuit

B

BF	Beamforming
BFU	Beamforming Unit
BRAM	Block Random Access Memory

C

CT	Computed Tomography
CS	Compressed Sensing
CR	Contrast Ratio

D

DSP	Digital Signal Processor
DDR	Double Data Rate

F

FP	Focal Point
FPS	Frames Per Second
FOV	Field of View
FPGA	Field Programmable Gate Array
FIR	Finite Impulse Response
FMC	FPGA Mezzanine Card

G

GUI	Graphical User Interface
GPU	Graphics Processing Unit

H

HDMI	High-Definition Multimedia Interface
HLS	High-Level Synthesis

I

IMU	Inertial Measurement Unit
------------	---------------------------

L

LC	Log-Compression
LPF	Low-Pass Filter
LSB	Least Significant Bit
LUT	LookUp Table

M

MRI	Magnetic Resonance Imaging
------------	----------------------------

P

PSF	Point Spread Function
PSNR	Peak-Signal-to-Noise Ratio
PCB	Printed Circuit Board

Q

QSFP+	Quad enhanced Small Form-factor Pluggable
QSPI	Quad Serial Peripheral Interface

R

RF	Radio Frequency
ROI	Region of Interest
RCA	Row-Column Addressed

List of Tables

RTL	Register-Transfer Level
------------	-------------------------

S

SC	Scan-Conversion
-----------	-----------------

SA	Synthetic Aperture
-----------	--------------------

SHEDA	Steering-based Hardware-Efficient Delay Approximation
--------------	---

SCA	SHEDA-Correction Apodization
------------	------------------------------

SIRI	Single-Insonification Reconstruction Imaging
-------------	--

SFP	Small Form-Factor Pluggable
------------	-----------------------------

T

TEE	Trans-Esophageal Echocardiography
------------	-----------------------------------

TOBE	Top-Orthogonal-to-Bottom-Electrode
-------------	------------------------------------

TGC	Time-Gain Compensation
------------	------------------------

U

US	Ultrasound
-----------	------------

V

VPS	Volumes Per Second
------------	--------------------

VDMA	Video Direct Memory Access
-------------	----------------------------

1 - 3

1D	One-Dimensional
-----------	-----------------

2D	Two-Dimensional
-----------	-----------------

3D	Three-Dimensional
-----------	-------------------

1 Introduction

Navigating virtually inside the body, imaging entire structures, and monitoring functions are the main aim of medical imaging techniques; from the size of organs to the neural potentials, for both static and dynamic structures. *Ultrasound (US)* imaging, named sonography, is one of those medical diagnostic techniques. It relies on US beam(s) application to image mainly soft tissues, like the kidneys and the liver, and liquid estimation, like blood flow. US is considered the go-to imaging method in women's health (obstetrics, gynecology), and is prevalently used in many other applications like cardiology, ophthalmology, urology, angiology, etc.. The main assets of US imaging are its avoidance of ionizing radiation (i.e. safety), non-invasiveness, moderate cost, versatility, and precautions-free scanning routine. In contrast, other imaging techniques like X-ray and *Computed Tomography (CT)* are based on ionizing radiation, and *Magnetic Resonance Imaging (MRI)* is more expensive, more oppressive, and requires strict precautions. In other words, US can be seen as a safe and cheap camera that can be used to take several shots of the body at a high rate without any health risk - unlike X-ray and CT - or excessive cost, unlike MRI.

Although medical US has been in use since the 1950s, it is still an active area for research. A main shortcoming in US imaging service is the high dependency on the presence of experienced sonographers to acquire the scan. In other words and following the previous mentioned analogy, the cheap and safe camera cannot be operated by everybody. Most US arrays are uni-dimensional, and insonify a planar body section, of which a *Two-Dimensional (2D)* image can be reconstructed. A consequence is that the observation of specific tissue features requires pinpoint precision in the positioning of the probe, which cannot be achieved unless the operator is a highly trained sonographer. This impedes reaping the benefits of US imaging in many environments where the presence of a sonographer is problematic, by disabling telemedicine approaches in the US domain, a goal that would be called *telesonography*. Telesonography is the remote diagnosis of US scans, by allowing the *decoupling* of acquisition - something that would be done by a lightly-trained nurse, a family doctor, etc. - from actual diagnosis at a hospital by a professional. Telesonography would create the opportunity to enable US diagnosis in rural areas, in rescue situations (e.g. medical helicopters or ambulances), in

enclosed spaces (like aircrafts and ships), and special fields (like oil platforms and battlefields). Furthermore, family doctors will be able to perform US scans, reducing the long queuing on hospitals and saving time and cost. For specialized applications where cost is no concern, e.g. for space stations, solutions have been devised [12–14] to operate a US probe remotely and in realtime via robotic actuators. Such solution is impractically complex for general *on-site* adoption due to the setup requirements (cost, area, and conditions), the probe-movement freedom and accuracy, and the continued fundamental need for an experienced sonographer on the hospital side to operate the scanner which will be a bottleneck [14–17]. Therefore, telesonography has not been enabled yet and, until today, US is only available in hospitals and specialized cabinets, or at least limited to a sonographer presence.



Figure 1.1: Three different contemporary volumetric US scanners. (a) Samsung WS80a, picture from [1]. (b) Philips EPIQ 7, picture from [2]. (c) GE Voluson E10, picture from [3].

Three-Dimensional (3D) US imaging, a technology originally developed and still used mainly for cardiology applications, can solve this problem by acquiring volumetric images at once. The 3D nature of the scans relaxes the precision constraints on the positioning of the probe, potentially allowing untrained or lightly-trained operators, e.g. paramedics, to acquire scans on the field. Either in realtime or subsequently, these volumes could be uploaded to a hospital, where a resident sonographer would reach a diagnosis. Unfortunately, today's 3D US systems are very expensive, stationary and power-consuming, as the result of the enormous computation requirements of volumetric US reconstruction. Figure 1.1 shows three advanced volumetric sonography devices that can be found in today's well-equipped hospitals. The result is that, once again, 3D US is still limited to hospital environments [2, 3, 18, 19]. To solve this vicious cycle, it is necessary to design a 3D US imager that has good image quality but is cheaper and portable, and ideally can operate on batteries. On the other hand, point-of-care devices that feature extreme portability do exist today [20–30] but they are limited to 2D,

which again introduce the strict dependency on having a sonographer available for the scan acquisition, negating the possibility of tele-ultrasonography.

Further, 3D US imaging has additional advantages over 2D imaging, which are; (i) the potential faster acquisition time since a whole volume is acquired at once rather than the 2D sweeping, (ii) the more expressive reconstructions, like in obstetrics application, (iii) the improved clinical assessment, e.g. for cardiac chamber volumetric measurement, and (iv) the easier imaging for large organs, like the liver.

This thesis presents the first tele-ultrasonography-capable prototype. Indeed, we enable the cheap and safe camera (i.e. medical US system) to be used by anyone anywhere by realizing the whole digital processing side of volumetric imaging in a compact embodiment (single-Field Programmable Gate Array (FPGA) and battery powered).

Two initial steps are essential before addressing our tele-ultrasonography-capable platform goal; first is to understand the basic working mechanism of the US reconstruction (Section 1.1), and second is to identify the challenges prevent this target from being achieved (Section 1.3).

1.1 Ultrasound Imaging Working Principle

US imaging is performed in three main steps: acquisition, reconstruction, and visualization. Acquisition happens via a process called *insonification* depicted by Figure 1.2, whereby a *Radio Frequency (RF)* (2-20 MHz) sound wave is emitted (in red) by an array of piezoelectric elements (*probe*) into the *Region of Interest (ROI)*. The ROI should ideally consist mostly of soft tissues. The incident wave is scattered by body tissue inhomogeneities, that act as secondary point sources (*scatterers*). The reflected echoes (in green), still in the RF range, are received by the same probe and the signals are then sent over a cable to a back-end imaging system to be processed and reconstructed. By using a probe comprising a *One-Dimensional (1D)* array of elements D , a 2D body slice can be insonified; with a two-dimensional (matrix) probe, a quasi-pyramidal 3D volume can be scanned (Figure 1.3).

The echoes returned by tissue discontinuities are processed with an algorithm called *Beamforming (BF)*. BF reconstructs an image by defining the reflectivity of the tissue (scatterers) at numerous locations, called *Focal Point (FP)*s. This is accomplished by summing the returned echoes according to a delay profile that represents the time taken by a US wave to travel from an origin O to a FP $S \in V$ and be backscattered to a transducer element $D \in 1, \dots, N$. The reflectivity correlates to the amplitude of the summed echoes and is ultimately rendered as a darker or brighter pixel in a greyscale image. A key part of BF is thus the calculation of one delay profile per FP, as will be clarified in Sections 1.3.3 and 1.3.4.

Finally, a visualization processing step is performed to produce a displayable and readable image. In particular, the image must undergo *Scan-Conversion (SC)*, i.e. a polar-to-Cartesian transform, and *log-compression*, i.e. its brightness range must be mapped to a logarithmic

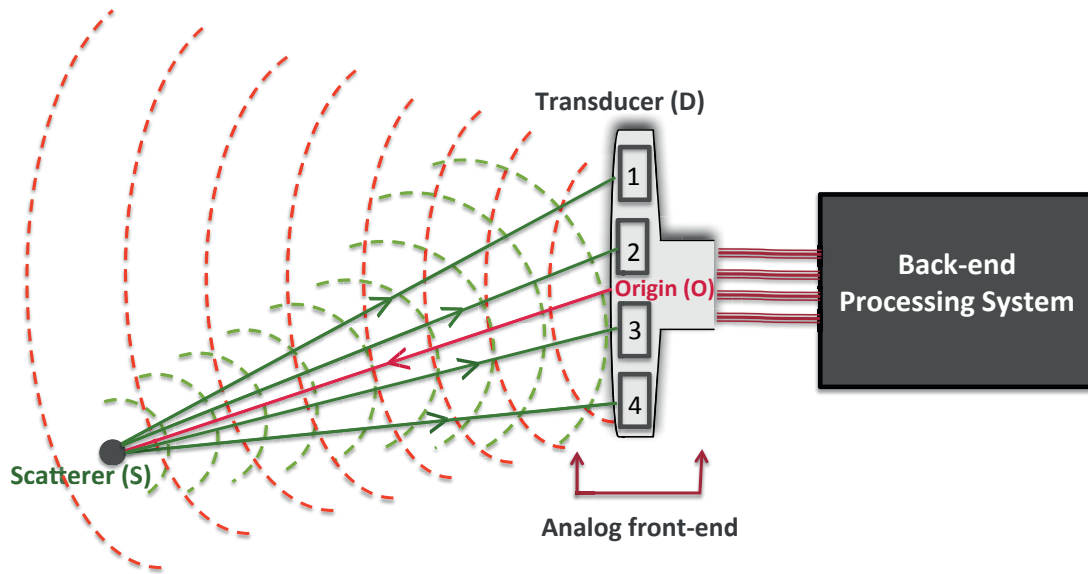


Figure 1.2: The US insonification process. The two-way time-of-flight of US is the time taken by the wave to be transmitted from an origin O to a scatterer S and reflected back to each transducer element D . The transmitted beam is in red, and the backscattered beam is in green.

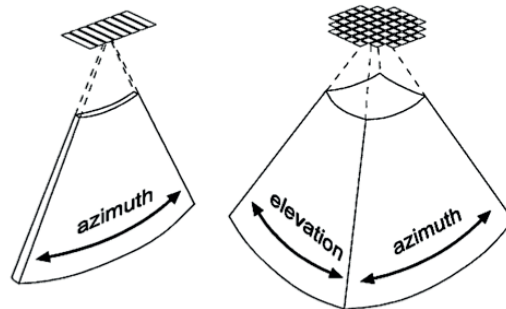


Figure 1.3: 2D versus 3D imaging. Left: array probe insonifying and acquiring a cross-section of the human body. Right: matrix probe insonifying and acquiring a quasi-pyramidal volume of the human body. Picture from [4].

scale adapted to human vision.

1.2 Ultrasound System Specifications

In order to put everything into its perspective, we will report numbers and evaluate quality based on the settings specified in Table 1.1. Both the challenges presented in Section 1.3, and later the evaluation of the proposed imager in Sections 6.4 and 7.7 are reported based on these settings. This is without loss of generality and scalability of the proposed algorithmic and architectural contributions. We present two versions of US imagers: a 2D US imager that supports 64 receive channels and reconstructs with a resolution of 64×500 FPs per image, and a 3D US imager that supports 32×32 receive channels and reconstructs $64 \times 64 \times 500$ FPs per volume. The choice of the sampling frequency f_s value, which is $5 \times f_c$, and the meaning of the *element directivity* are clarified in Section 2.2.

Table 1.1: System Specifications

Parameter	Symbol	Value
Speed of sound in tissue	c	1540 m/s
Transducer center frequency	f_0	4 MHz
Transducer bandwidth	B	4 MHz
Wavelength	λ	0.385 mm
Transducer pitch		$\lambda/2$
Sampling frequency	f_s	20 MHz
2D specification		
Transducer array size (2D)	N	64 elements
Focal points (2D)	F_{2D}	$64 \times 500 = 32k$
Imaging cross-section ($\theta \times r$, 2D)		$73^\circ \times 260\lambda$
Element directivity in the 1D Array probe (acceptance angle)		0.707 rad
3D specification		
Transducer matrix size (3D)	$N_x \times N_y$	32×32 elements
Focal points (3D)	F_{3D}	$64 \times 64 \times 500 = 2M$
Imaging volume ($\theta \times \phi \times r$, 3D)		$73^\circ \times 73^\circ \times 260\lambda$
Element directivity in the 2D Matrix probe (acceptance angle)		0.707 rad

1.3 Telesonography Challenges

Enabling telesonography is conditioned by realizing a US medical system that fulfills the following features; (i) is able to perform full 3D imaging, (ii) is portable, (iii) is low-power (ideally battery operated), (iv) is low-cost, (v) is operator-friendly, and (vi) is able to provide high quality reconstructions, since in medical applications reliability and accuracy are not negotiable. This creates several challenges; (i) technology challenges represented by the matrix probe manufacturing and the interfacing of the high number of channels between the sensing part (i.e. the probe) and the processing part (i.e. the reconstruction unit) (Challenge 1), (ii) the challenges emerged from the need to perform massive amounts of computations - for 3D

reconstruction - in a tight resource budget (Challenges 2, 3, 4, and 5), and (iii) the challenges resulted from the decoupling of US acquisition from the diagnosis that have always been performed together at the same time by the same expert US specialist (Challenges 6 and 7). In this research, we focus more on the last two groups; (ii) and (iii) of challenges, while addressing the interfacing side of the group (i) of challenges. Matrix probe manufacturing to support high number of channels input while meeting the thermal regulations and the battery power budget, has not been tackled in that study.

1.3.1 Challenge 1: Transducer-Processing System Interfacing, and Input Bandwidth and Memory Requirements for the Samples

In this thesis, we are concerned more with the back-end digital side (Figure 1.2) and its challenges. However, the interfacing between the analog front-end and the back-end digital processing system is a must-to-be-addressed problem to eventually achieve a realistic complete system. The interfacing between a US matrix probe and the processing back-end system is one of the most challenging obstacles in 3D US imaging in general. The problem has been raised from different perspectives; (i) the matrix probe availability for research purposes, (ii) the required bandwidth to feed the data in realtime from all of these channels, and (iii) the required storage size for the input data.

In 2D imaging, and by referring to Table 1.1, the input data rate of the 64-channel probe - given the 20 MHz sampling frequency - is 1.28 G samples/sec. The typical *Analog-to-Digital Converter (ADC)* precisions for US applications are 12-16 bits; assuming a digitization resolution of 12 bits per sample, around 15.3 Gbps will be required to provide the input stream in realtime. The problem is much more challenging in 3D, where the required bandwidth will be 16 times higher due to the increase in the number of channels. This means that the interface bandwidth will be a question of around 245 Gbps. This is far beyond the capabilities of the typical used technologies.

In addition, each of the supported 32×32 input channels - given the 10 cm target penetration depth (to be traversed forward and backward), c , and f_s as specified in Table 1.1 - produces 2597 data samples per insonification. Given the common US ADC precisions, and by assuming 2 bytes per sample, over 5 MB of samples are produced per insonification. This dataset is beyond what can be practically stored on-chip in most architectures, forcing a streaming design that reconstructs slices of the image from small subsets of the input data.

Further, matrix probes are quite expensive and they are - mostly and until recently - not enabled for open RF data access for research purposes. Therefore, non-realtime and simulated inputs should be exploited to be able to perform research and development in the back-end digital side, and proceed in exploring, proposing, and testing new techniques.

1.3.2 Challenge 2: Beamforming Resolution

The BF process relies on fine-grained time differences to locate the position of body features. Any imprecision may result in poor focus, image artifacts, aliasing, etc. The imprecisions can be introduced by inaccuracies in the delays calculation, or/and insufficient reconstruction resolution. The delay calculation accuracy is the most critical factor since it is controlled by the used algorithm, methodology, and implementation for the calculation. The reconstruction resolution is defined by the number of scanlines -in azimuth and elevation directions - and radial lines resolving the ROI for BF. In another words, it is the number of FPs representing the ROI. The reconstruction resolution is typically configurable. However, the trade-off between the increase in the number of FPs and the corresponding increase in the computation load and resources should be always considered (refer to Challenge 3, 4, and 5).

1.3.3 Challenge 3: Realtime Beamforming Computation Load

One of the main bottlenecks in the processing pipelines is the delay calculation in the BF process. It requires the calculation of the two-way time-of-flight of the US wave to travel from an origin O to each scatterer S - named transmit delay Tx (the red straight line in Figure 1.2) - and back scattered from S to each transducer element D , named receive delay Rx (the green straight lines in Figure 1.2). In Figure 1.2, both the Tx time spent to follow the red straight line and the four Rx times spent to follow the green straight lines need to be calculated to reconstruct only this single scatterer S in the figure. In reality, a body region is imaged as a collection of numerous number of this scatterer (or FPs), depending on the reconstruction resolution (Section 1.3.2), while the transducer can easily comprise tens of elements in 2D case, and hundreds or even thousands of elements in 3D case.

According to the settings specified in Table 1.1, to reconstruct a frame in 2D imaging based on a single emission origin O , $F_{2D} + N \times F_{2D} \approx 2$ M delays/image will need to be calculated. On the other hand, for 3D imaging, this number will be significantly increased to $F_{3D} + N_x \times N_y \times F_{3D} \approx 2.1$ billion delays/image. At a desired frame rate of e.g. 30 *Volumes Per Second (VPS)*, around 63 billion delays will need to be calculated per second. Each delay value is the calculation of the Euclidean distance divided by the speed of sound c in the medium, which is typically assumed constant. This means that in 3D imaging, 63 billion square-roots calculation per second will need to be dealt with. In other words, from 2D to 3D imaging, as both the number of image points and the number of probe elements increase by 64 and 16, respectively, the total number of calculations increases by a factor of around 1024. Evaluating this complex function in realtime is obviously extremely challenging within a portable, inexpensive, and battery operated platform. Further, image enhancement techniques are widely used in medical practice and should be supported, at an additional complexity cost. This includes for example compound imaging [31] (refer to Section 2.3.4), whereby the final image is obtained by combining multiple ROI reconstructions. For the same overall frame rate, this technique has a linear computation overhead, i.e. if the compounding count is 5, then 5 times as many

delay calculations will be required. Other techniques, such as zone imaging (Section 2.3.3), improve resolution, but also entail additional complexity.

All of that are only for the delay calculation unit in the BF process. However, BF includes another essential unit, called *apodization* (Section 2.2), which weights the transducer elements differently for each FP (scatterer) reconstruction; i.e. $V \times N = 2.1$ billion evaluations.

1.3.4 Challenge 4: Memory Requirements and Access Bandwidth to The Beamforming Coefficients

An intuitive solution to Challenge 3 is to pre-calculate the delay and apodization functions for all possible geometries, and then to fetch the values on the fly from tables. Based on the same reasoning above, 2.1 billion distinct delay and as many apodization values would need to be stored; assuming a 16-bit representation of the values, this equals 8.4 GB of coefficient tables, necessarily stored off-chip. All 8.4 GB of coefficients would then need to be fetched 30 times per second, for a bandwidth of 252 GB/s. This implies unrealistic hardware costs and power budgets for the memory subsystem¹.

1.3.5 Challenge 5: Post-Processing Computation Load

The second source of the computation bottleneck in the 3D US processing pipeline is in the volume visualization and rendering phase, in particular, the SC process. In 3D, the SC, which includes the transformation from polar to Cartesian coordinates of the beamformed data, is a very demanding process in terms of computation load, memory requirements, and output interfacing. According to the *Field of View (FOV)* geometry and the reconstruction resolution specified in Table 1.1, $(2 \times 500 \sin(\frac{73}{2})) \times (2 \times 500 \sin(\frac{73}{2})) \times 500 = 177$ million interpolations per volume rendering will be required. This includes another critical demand, which is the on-chip memory requirement to keep both the beamformed data and the post-SC data. Indeed, it is impractical to be fit in a compact footprint like a single FPGA, which is supposed to not only include the SC alone but along with other processes and bottlenecks mentioned before. Moreover, the visualization step includes the demodulation filtering, the log-compression function, and the need to a high bandwidth to show the output in realtime. Therefore, smart ideas and optimizations are needed.

1.3.6 Challenge 6: Probe Positioning and Scans Labeling By Untrained Operator

Since the invention of medical US, the sonographer has always had the full control over the positioning of the probe. There has been a direct hand-eye coordination allowing the specialist to move the probe until finding the sought anatomical features and reaching realtime diagnosis. Telesonography severs this connection and makes it time-consuming or problematic for a

¹Note that, in a special fully symmetric geometry setup, leveraging quadrant symmetry might reduce the memory footprint requirements by 4X, but this solution is not generic.

remote doctor to even identify the location origin of a remotely acquired and unlabeled scan. For instance, an experienced sonographer can distinguish between cardiac and kidney scans. However, the two kidneys would be essentially indistinguishable from each other if acquired in unlabeled scans. Therefore, it is imperative for the scans to be somehow position-tagged. Yet, a lightly trained operator on-site may not have the necessary expertise or precision. This includes the inevitable need to provide probe positioning guidance to the untrained operator, who might not even know the anatomy of the human body, for the most common US scans.

1.3.7 Challenge 7: Reconstructed Volumes Transmission

In telemedicine, the whole reconstructed volumes will need to be transmitted for remote diagnosis. This implies the demand for lossless compression techniques to achieve reliable yet low bandwidth transmission. A reconstructed volume has a resolution of $64 \times 64 \times 500$. After the log-compression process, the frame will be represented in 8-bit gray scale, which means that a *single* volume will have a size of 2 MB. Typically, a movie (4D) will be acquired, otherwise, it will be at least several shots. Therefore, a case for data compression will be raised since every bit counts.

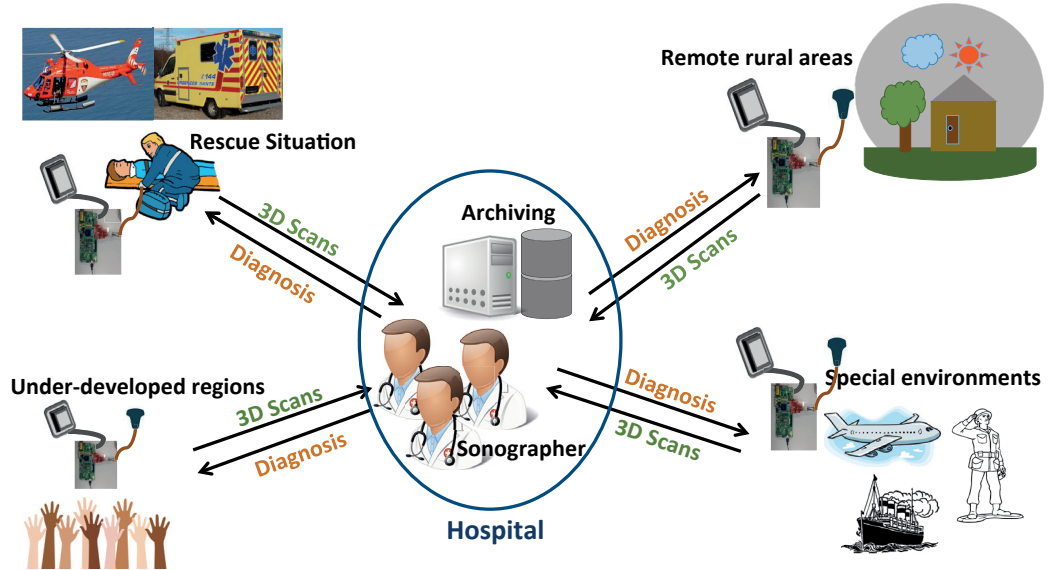


Figure 1.4: Workflows enabled by the proposed telesonographic imager.

1.4 Novel Contributions

In this research, each of the challenges of the digital processing unit (Section 1.3) has been addressed with the aim of telemedicine-capable imaging system. In response to the telemedicine requirements outlined above, our digital back-end prototype (i) supports 3D US, (ii) reconstructs good-quality images thanks to the scalable support for a high transducer channel

count, e.g. 1024 which is on par with the state of the art, (iii) is contained within a relatively inexpensive single off-the-shelf Kintex UltraScale KU040 FPGA [32], (iv) has an estimated power budget of 5W, (v) provides a complete digital signal processing pipeline from sampled echo signals to on-screen image over *High-Definition Multimedia Interface (HDMI)*, (vi) offers two basic scan-converted orthogonal cross-sections to provide realtime feedback to the operator, (vii) supports various imaging modes including zone imaging and compound imaging. The single-FPGA demonstrator has a size of 26.7cm×14cm×0.16cm size. The design is highly scalable, and can either be scaled up on a larger FPGA or scaled down if only 2D imaging is required.

This has been successfully achieved by first building, investigating, and studying the US imaging pipeline - both in 2D and 3D -, then, tackling every block by proposing and implementing efficient techniques, smart algorithms and ideas, and optimized FPGA architectures. Our telesonographic platform can be deployed, as shown in Figure 1.4, in rescue situations, remote under-served areas, developing regions, and special environments like aircrafts, ships, battlefields, etc.. In all of these cases, an operator, who can be a paramedic or a very lightly trained person, acquires 3D scans for the region of interest and uploads them to a hospital, where a sonographer can diagnose and archive the scan.

1.5 Thesis Outlines

The next chapters discuss the work behind achieving our goal and all the technical details. The thesis is organized as follows;

Chapter 2: The basic definitions, terminology, and background of US will be highlighted. This includes different types of medical US transducers, beam profiles, common processes in the reconstruction pipeline, and some prevalent imaging modes. This will be followed by a detailed literature review about the state-of-the-art systems and work, both in research and commercial domains, to solve the 3D US processing challenges.

Chapter 3: Our developed feature-rich 2D/3D US Matlab-based toolkit will be presented. This includes the discussion on the different algorithmic and parametric options supported by the pipeline. Few examples of these options are reported in the chapter.

Chapter 4: A detailed illustration, mathematically and architecturally (FPGA), of our novel delay calculation algorithm (SHEDA calculator) will be shown. The significant impact of the approach on simplifying the computation requirements will be highlighted. In addition, we have assessed, qualitatively and quantitatively, the algorithmic approximation inaccuracy.

Chapter 5: We will continue demonstrating the optimization contribution in the reconstruction and BF unit. In this chapter, we propose a novel apodization function (SCA scheme) to compensate for the inaccuracy introduced by the proposed delay calculation algo-

rithm (Chapter 4). Two additional apodization schemes are discussed. Further, we delineate the final implementation we chose for our single FPGA and the evaluation of this careful simplification. Moreover, the details of the hardware realization of the amplification function on the received echo (Time-Gain Compensation (TGC) defined in Section 2.2) is clarified. This is followed by reporting the efficient BF order used by the architecture, the input data mapping to memory, and the realization of the last step in the used BF method.

Chapter 6: We turn to the post-processing step including our simple and resource-friendly demodulation algorithm, and the proposed telemedicine-suitable idea of the on-site cross-sectional SC process that significantly saves computation load (and accordingly resources). Moreover, the different imaging modes supported by the prototype are revealed. This is followed by intensive quality assessment for the system reconstruction in these modes using various quality metrics; quantitatively - Peak-Signal-to-Noise Ratio (PSNR), and Contrast Ratio (CR) metrics - and qualitatively using Point Spread Function (PSF) and Visual assessment.

Chapter 7: In this chapter, diverse topics about the proposed tele-ultrasonography-capable design are discussed. We elucidate: (i) the two supported options for the input interfacing of our system; how we provide US raw data to the imager for both 2D and 3D imaging cases, (ii) the data representation in our FPGA design, (iii) the communication logic between the FPGA, the board microprocessor (the MicroBlaze), and the developed Graphical User Interface (GUI), and (iv) the platform self-bootability. Further, we propose two solutions for the gap arose from the decoupling of the acquisition from the diagnosis created by the tele-ultrasonography concept. Bridging that gap is essential to avoid false diagnosis, and to save time and effort on the US specialist side. Finally, we evaluate our single-FPGA 2D/3D US processor in terms of the resource utilization, system performance, and the prototype size and cost. This is with a recap for the design quality assessments distributed in the previous chapters.

Chapter 8: A conclusion for the whole research will be presented, followed by suggested future directions.

2 Background and Previous Work

Before addressing the problem and solving the tele-ultrasonography question, we explain the US imaging mechanism in this chapter. Different types of US transducers; the starting point of the imaging process, and their different possible beam profiles are presented in Section 2.1. In Section 2.2, we elucidate the common US imaging reconstruction and processing units including the basic sonography definitions and terminologies, which will be used all over the thesis. This is followed by the illustration of the most common medical US imaging modes (Section 2.3).

Finally, the literature review for the recent commercial systems and research work is presented in Section 2.4. This includes the various proposed solutions to tackle the problem and their advantages and drawbacks. All of these topics are presented in this chapter as a preparation for the next following chapters that describe our solution for a tele-ultrasonography-capable system.

2.1 Ultrasound Transducers and Beam Profiles

In order to image a body part with US techniques, the first step is the transmission of high-frequency (often called RF for Radio Frequency) acoustic waveforms through the region of interest by a process called *insonification*. This is achieved with a US transducer comprising a set of vibrating elements, often based on the piezoelectric principle. The piezoelectric principle relies on the property of some materials to convert mechanical signals, like sound waves (vibrations), into electrical signals, and vice-versa. In the transmission phase, electrical signals are applied to the piezoelectric crystals, which in-response propagate vibrations through the human body. These vibrations get reflected back by tissue inhomogeneities, and are picked up by the same crystals, which in the receive phase perform the opposite transformation from vibrations to voltage signals.

The piezoelectric elements are most commonly physically laid in a straight row, in *linear* and *phased* arrays (Figure 2.1 left and center), or in a convex arrangement (*convex array*) (Figure 2.1 right). A linear array, called also as *sequential array*, has usually narrow element

directivity, and therefore it is designed in a large probe face. Phased arrays are similar to linear arrays, but electronically steer the beam sideways thanks to the supported control system that electronically manipulates and drives the excitation of the elements, thus sweeping a circular sector and removing the directivity restriction. Other layouts are also possible for specialized applications, like annular arrays, i.e. ring-shaped transducers, for mammographies.

Recently, volumetric or 3D imaging has also become available. 3D imaging is achieved by means of a probe with a matrix of elements (Figure 2.2 left) - rather than an array -, or by mechanically sweeping a probe for 2D imaging and by collating the acquired frames (Figure 2.2 right).

Any probe can be driven so that its elements get excited - and hence vibrate - in unison, or with a certain delay profile, which controls *transmit (Tx) focusing*. The overall acoustic wave changes in wavefront and direction of propagation, as seen in Figure 2.3. In linear arrays, and since the piezoelectric elements have limited directivity, the elements get typically excited in unison, and the resulting wave propagates right in front of the probe, yielding a plane wave (Figure 2.3(a)). In phased arrays, we apply Tx delay profiles to the elements' excitation allowing for more complex wavefronts; both sweeping and shaping. In particular, it is possible to distribute the acoustic pressure evenly in the volume of interest (like with a linear array), steer the wavefront, or concentrate it in specific areas, yielding better local resolution since the resolution is a function of energy (Figure 2.3(b)). It is even possible to choose a diverging beam, where a virtual focal point is behind the transducer [33] (Figure 2.3(c)), or even on the transducer face, to insonify a wider region at once. Transmit focusing has a quality impact on the images, but no particular overhead on computation times. It complements the receive focusing that is performed in BF.

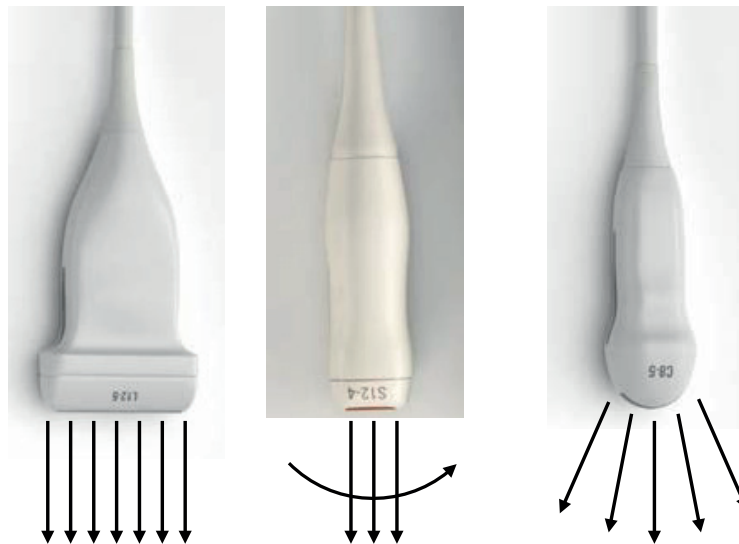


Figure 2.1: Examples of US array probes and of their acoustic emission. Left: linear array; center: phased array; right: convex array. Probe pictures from the Philips catalog [5].

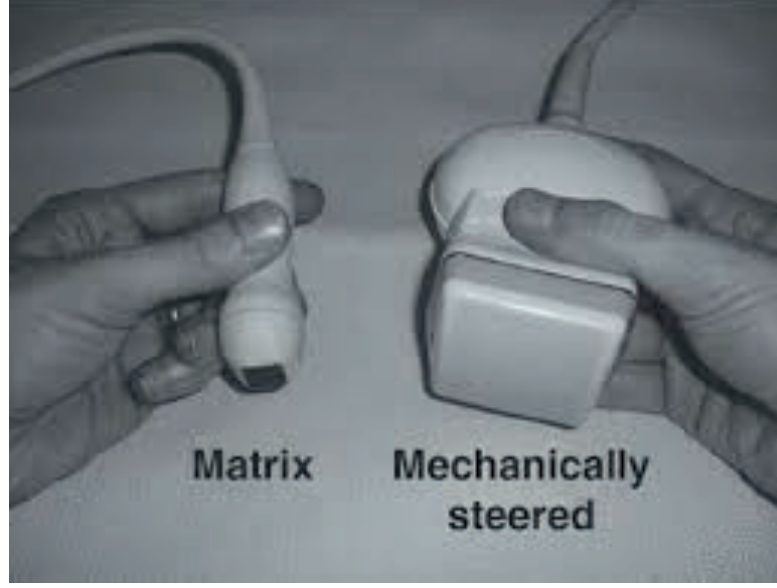


Figure 2.2: 3D US imaging probes. Left: matrix probe. Right: mechanically sweeping probe. Probe picture from [6].

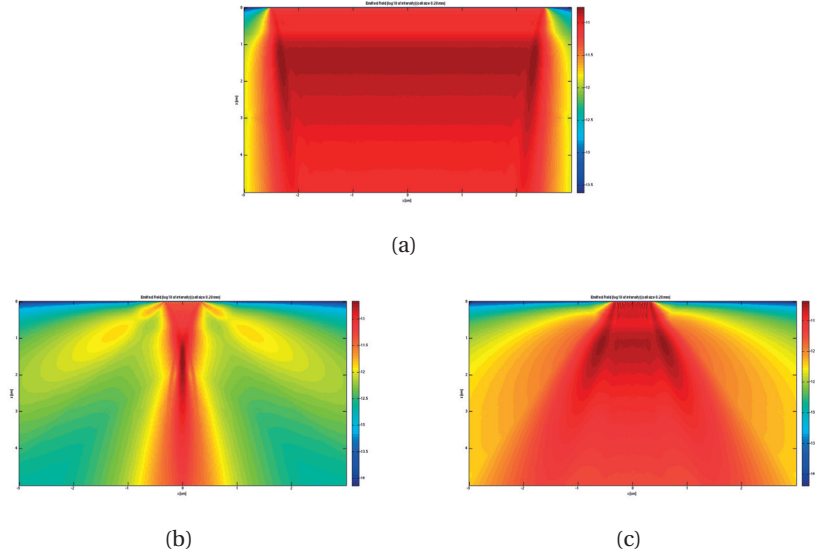


Figure 2.3: Different transmit focusing options. The transducer is at the top of the figures. (a) Plane wave, using a 192-element *linear* probe. (b) Converging wave, using a 16-element *phased* probe. (c) Diverging wave, using a 16-element *phased* probe.

2.2 Ultrasound Processing, Reconstruction, and Terminologies

A US imager requires transmit (TX) and receive (RX) blocks. The TX block (Section 2.1) is active for a few microseconds, during which an acoustic wave emission at a frequency dependent on probe design - usually in the range of 2-30 MHz - occurs. After each TX phase, the acoustic

wave propagates into the body and part of its energy is reflected towards the probe by body tissue inhomogeneities, which cause acoustic impedance mismatches. The echo signals received by each transducer element are then sent over a cable to be processed by the RX circuitry. The body can be seen as a collection of *scatterers* with different reflective properties. The imaging problem is therefore equivalently formulated as the problem of reconstructing the distribution and amplitude of scatterers in space based on the back-scattered echoes.

For convenience of illustration, Figure 2.4 shows a very generic US processing diagram. The Rx circuitry starts with analog conditioning represented by the *Analog Front-End (AFE)* block. An amplification followed by ADC is needed to digitize the analog echo signals. As a rule of thumb [34], the sampling frequency of a beamformer needs to be chosen 4 to 10 times higher than the center frequency f_c of the transducer - because of the Nyquist theorem and the typical bandwidths of the medical US transducers -, or *at least* two times its bandwidth with quadrature sampling [35–37].

After the AFE block, the digitized signals undergo processing by the digital back-end system. The US wave propagating inside the body is exposed to attenuation directly proportional to the traveling depth. This means that echoes arriving later (i.e. reflected by deeper scatterers) are more attenuated than echoes received earlier (i.e. reflected by shallower scatterers). A time-based compensation needs to be applied, called *TGC*. TGC can be performed in the analog domain, for example in the transducer head, but also in the digital domain. It is optional to apply decimation to the signal to reduce the time complexity of the reconstruction algorithms, while following the guidelines of the sampling rules mentioned before. Afterwards, the signal should be high-pass filtered to remove the low-frequency content that may occur due to saturation of amplifiers under some operating conditions.

The returned digitized, and time-gain compensated RF echoes are processed by a set of algorithms that vary from a system to another. Nonetheless, the most essential and the core of any US processing pipeline is a process called *beamforming (BF)*. BF consists of coherently summing up the echo signals received by the various channels; in this way, the reflectivity of the tissue at numerous FP sites - defined by the reconstruction resolution - can be identified. BF consists of three main operations: (i) the echo signals must be shifted in time depending on the image point under consideration, (ii) they must be weighted (apodized) to optimize antenna (i.e. probe element) directivity, and (iii) they must be summed. The first step, which is the calculation of one delay profile per FP, is the kernel and the main bottleneck of the BF process. The sampling frequency defines the resolution with which the delays need to be computed. For example, in Table 1.1, we have defined $f_s = 5f_c = 20MHz$, which indicates delay calculation at a granularity of 50 ns. The delay profile models the round-trip propagation time necessary to travel from the sound origin O to a body scatterer S and back towards each element D of the probe (Figure 1.2). A dedicated delay profile should be applied for each image point (FP), which can be seen as a “focusing” at every scatterer location. Therefore, this process is named *dynamic Rx focusing*. Unfortunately, this leads to a high computation bottleneck in the image reconstruction pipeline (Section 1.3.3 and 1.3.4).

2.2. Ultrasound Processing, Reconstruction, and Terminologies

BF includes another important step named *apodization*. Apodization [38–42] is a weighting function applied to reduce radiation contributions from the sidelobe region of the transducer aperture - during emission and reception - which degrade both contrast and lateral resolution in the final image, while maintaining the main lobe representing the useful information. The apodization function is a window of weighting coefficients that weighs differently the echo samples of the elements within the directivity limit (element directivity -or acceptance angle - in Table 1.1). Finally, the delayed and weighted echoes are summed to reconstruct FPs. Figure 2.4 depicts the BF process by the *Beamforming Unit (BFU)*, which takes as inputs the sampled backscattered echoes from N probe elements. The BFU consists of N_k parallel blocks, each of which capable of RX-focusing on one image point per cycle. The BFU requires multiple cycles to reconstruct a whole frame, depending on the desired output resolution and on the N_k parallelism.

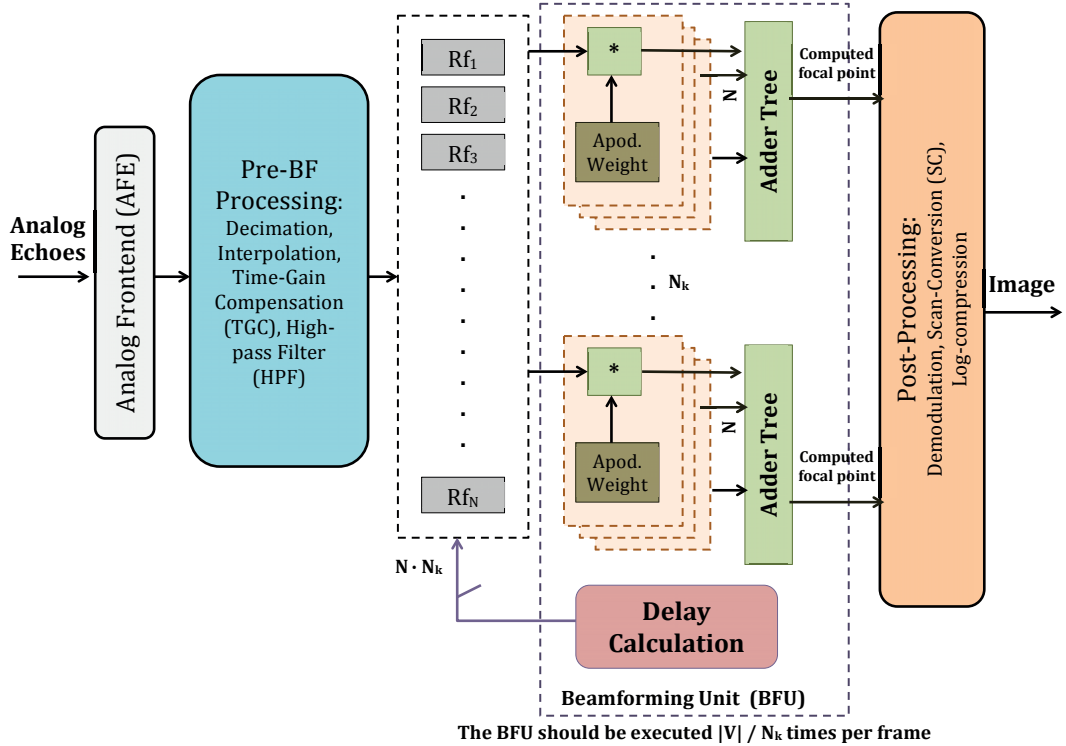


Figure 2.4: Architectural diagram of a generic ultrasound imaging system, with focus on the beamformer processing the sampled RF radio-frequency signals. N is the number of transducer matrix elements, N_k is the number of voxels per cycle the BFU can produce, and $|V|$ is the number of focal points to be computed.

The BF process to reconstruct a *single* scatterer S (FP) by computing its reflectivity s - which will ultimately be used to calculate the brightness of the corresponding image pixel - can be expressed mathematically by (2.1), where $e(D, t_p)$ is the echo received by an element D at a

time-of-flight t_p , and $w(t_p, D)$ is the weighting applied to the echoes sampled at time t_p .

$$s(S) = \sum_{D=1}^N e(D, t_p(|\vec{OS}|) + t_p(|\vec{SD}|)) w(t_p, D), \forall S \in V. \quad (2.1)$$

The high-frequency beamformed signals should then be demodulated to get the baseband information before visualization. Many techniques are available. Hilbert transform [43–46] and IQ demodulation [46–48] are among the most common demodulation techniques used for this purpose.

Finally, a visualization procedure is performed. The beamformed image undergoes a post-processing step to become displayable on a screen and interpretable by the human eye. This is achieved by two processes; *Scan Conversion (SC)* and *log-compression*. SC is a necessary process for identifying screen image pixels starting from beamformed echo signal amplitudes. In phased array or convex array imaging, SC changes the coordinate system from polar to Cartesian (Figure 2.5). Furthermore, since the reconstructed images are not necessarily represented at the same size and aspect ratio of the screen image, up-sampling or down-sampling may be involved. On the other hand, logarithmic compression is necessary to compress the extremely high dynamic range - up to 100 dB - of US echoes into a more usable and visible range of gray levels.

Figure 2.6 shows the logical processing flowchart for the basic blocks in any US reconstruction pipeline. In 3D imaging, both the BF and the SC processes represent the main bottlenecks and the most computationally and materially demanding units. Therefore, they are both colored in red in the flowchart indicating their criticality. All the flowchart blocks will be discussed, and computationally, architecturally, and/or algorithmically optimized in the next chapters of the thesis. This follows the aim of achieving the goal of a compact, low-power, and inexpensive medical US digital back-end processing system that enables telesonography for the first time.

2.2. Ultrasound Processing, Reconstruction, and Terminologies

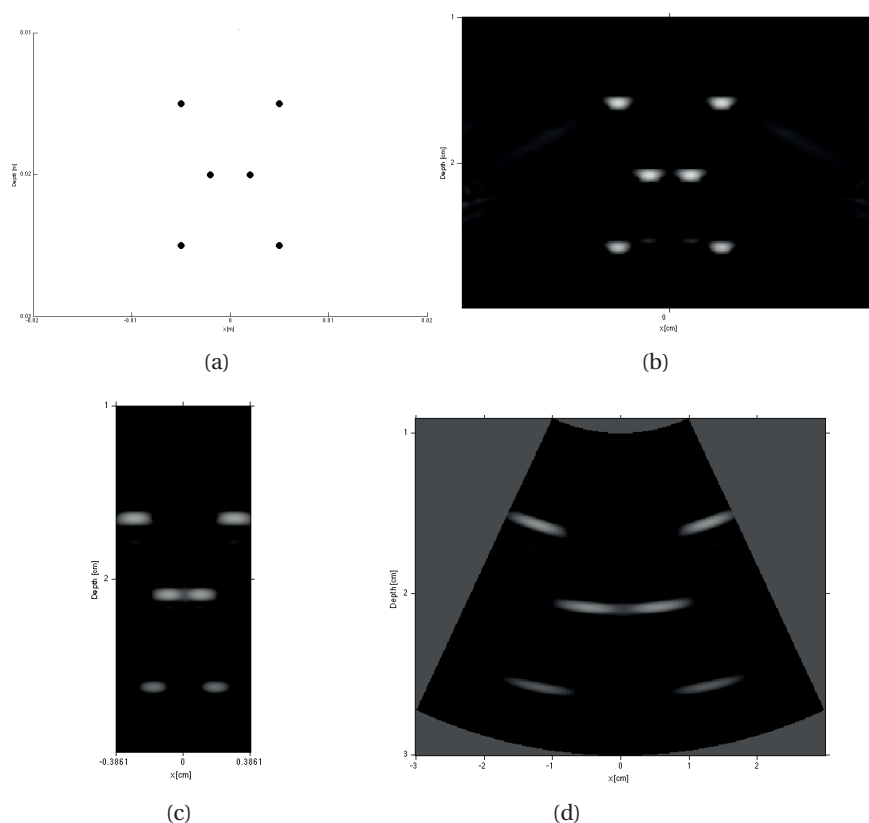


Figure 2.5: For a synthetic phantom comprising six punctiform scatterers (a), an image can be reconstructed by simulating a linear array and imaging a rectangular region (b), or a phased array and imaging a circular sector (c) and (d). (c) the beamformed sector, still in polar coordinates; (d) the same sector after scan conversion.

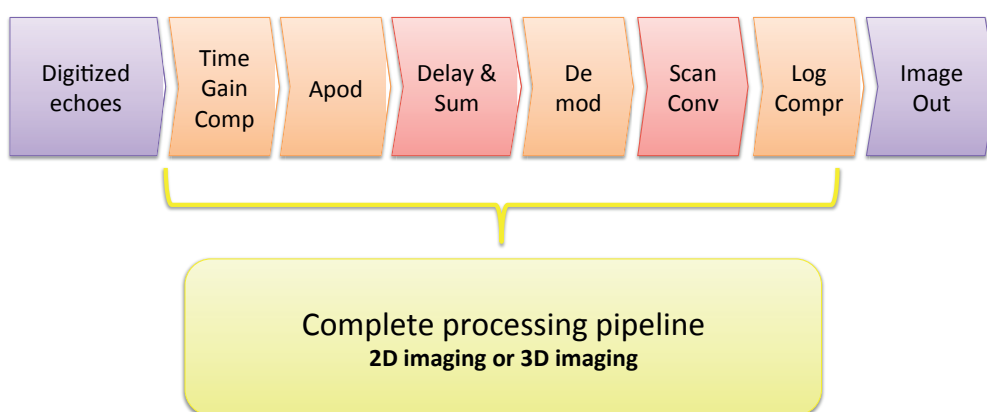


Figure 2.6: Logical processing flowchart of the US image reconstruction pipeline.

2.3 Common Ultrasound Imaging Modes

2.3.1 Conventional Imaging

In conventional US, a single scanline is reconstructed sequentially per insonification. Therefore, a number of insonifications commensurate with the number of scanlines are supposed to be performed. The focusing quality of conventional US is high due to the scanline-based Tx focus, where the US energy is concentrated on a single line at a time. However, this comes at a huge cost of acquisition time, reconstruction rate, memory requirement, and the introduction of motion artifacts due to the scanline-by-scanline acquisition mechanism. This mode is far unsuitable for 3D imaging since a volume comprises a much higher number of scanlines (e.g. 64×64 scanlines according to Table 1.1) - compared to the 2D case - and accordingly all the drawbacks will become much more severe. Most of today's 2D systems do not mainly rely on the conventional mode seeking a high frame rate throughput - suiting applications like cardiology and flow estimation imaging -, and avoiding all of its burdens.

2.3.2 Ultrafast Imaging

The opposite side of the scale and the simplest approach is to reconstruct the whole frame from a single insonification; i.e. reconstruct all the scanlines simultaneously at a time. Ultrahigh or ultrafast frame rate imaging [49, 50] relies heavily on this approach. It represents the maximum limit of parallel receive BF [51–53]. Therefore, it can be considered the most feasible imaging mode for 3D reconstruction. The insonification in this mode must utilize a broad wave profile, such as a diverging or plane wave (Figure 2.3(a) and 2.3(c)). Noting that acoustic waves in the body travel at approximately 1540 m/s, the two-way propagation delay, for a 10 cm imaging depth, is of about $130 \mu\text{s}$, meaning that with quick-enough signal processing, 7700 frames per second and up could in theory be produced. This level of speed requires definitely challenging electronic design, and is downright impractical, with current technology, for 2D even more so for 3D imaging. However, it still provides the highest possible frame rate (more than a thousand of frames per second with the current technologies), offering the most feasible imaging mechanism for modes combining multiple frames like compound imaging (Section 2.3.4). In ultrafast imaging, each processed frame is limited in resolution by the US energy density, i.e. the energy distribution over the FOV.

2.3.3 Zone Imaging

An alternative is *zone imaging*, whereby the frame is reconstructed from multiple insonifications. In zone sonography, the ROI is virtually divided into a number of non-overlapping zones - for example, in circular subsectors (Figure 2.7) -, each of which is sequentially beamformed based on a new insonification narrower than the one used in ultrafast imaging. Each new insonification may correspondingly shift the focus location, optimizing the intra-zone resolution in the direction of the ROI divisions. The zones are then stitched into a frame (Figure 2.7).

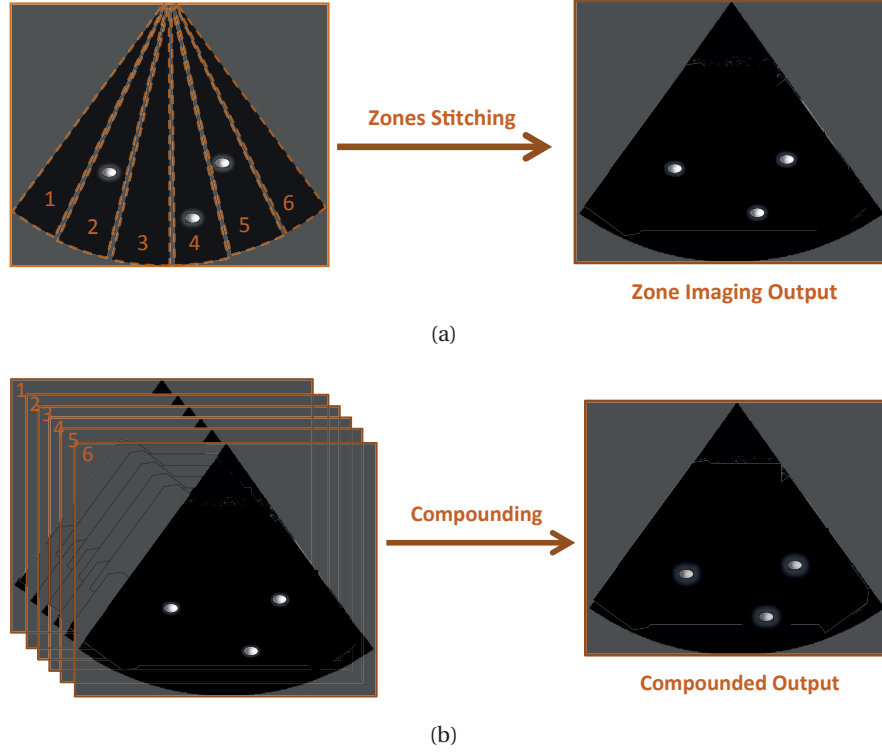


Figure 2.7: A sketch depicting the difference between zone and compound imaging in terms of the reconstruction mechanism. (a) In zone imaging, the output image is reconstructed by stitching the reconstructions of non-overlapping zones of the ROI, while (b) in compound imaging, the image is reconstructed based on compounding multiple reconstructions of the whole ROI, i.e. *full overlapping* between the contributing zones compared to zone imaging.

Zone imaging strikes a compromise between conventional high-quality US reconstruction, i.e. line-by-line with an insonification per line (which is completely impractical for 3D imaging due to the massive number of such lines), and ultrafast imaging (which has poorer resolution). This technique is used industrially by companies such as Zonare Medical Systems Inc. [54–56]. Figure 2.8 shows an example of the insonification profiles that can be used for 5-zone imaging reconstruction.

This approach reduces the maximum possible frame rate where the acquisition time becomes longer, proportionally to the number of zones and insonifications, while the processing time, processing resources, and memory requirements are supposed to be almost the same. It is better suited to systems where the reconstruction computations are slow. A downside of zone imaging is that patients are never perfectly still, resulting in potentially alignment glitches across zones. However, these glitches are much lower than in conventional imaging case.

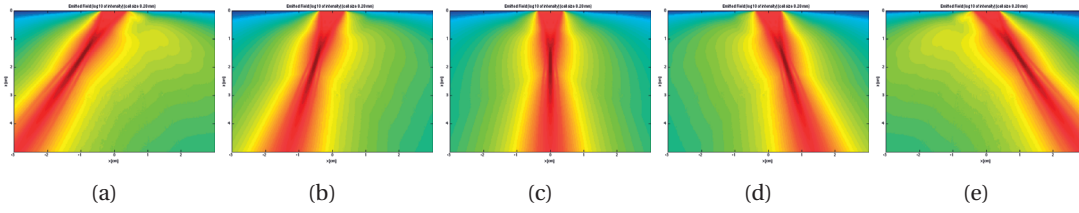


Figure 2.8: Example of possible focused beams for zone imaging, where five zones are insonified in sequence.

2.3.4 Compound Imaging

Any acquired US image frame is bound to have sub-optimal resolution and feature a certain degree of adverse phenomena including speckle, due to interference among acoustic waves and multiple reflections, and noise. This can be partially remediated by compounding techniques. In this technique, the whole ROI is imaged multiple times, and the various frames are merged (Figure 2.7) - using a blending operator, typically averaging - into a single better one leveraging their diversity. Although some diversity across subsequent reconstructions is always intrinsically present due to noise and subject movement, additional diversity is often intentionally introduced to improve the outcome. Commonly, the intentionally modified parameter is either the emission frequency, named frequency compounding - but this relies on the availability of a wideband transducer -, or the emission profile in space, named spatial compounding [31]. Further, compounding can be incoherent or coherent [57] depending if the compounding happens after or before envelope detection (i.e. demodulation), respectively. Compound imaging has the main purpose of reducing image speckle due to the coherent nature of the US waves used for imaging [58]. This comes at a corresponding penalty to frame rate, and is a good match to ultrahigh frame rate imaging, where the availability of such high throughput can be exploited to improve frame quality.

2.3.5 Tissue Harmonic Imaging

The acoustic propagation in the body is a non-linear process, giving rise to reflections that are harmonics of the insonification frequency; usually only the second harmonic has a significant amplitude. Provided that the probe has sufficient bandwidth to detect echoes at frequencies at least twice as high as the transmit frequency, the imager can then process the received echoes demodulating from the second harmonic of the nominal frequency, yielding better resolution and contrast than the fundamental image [59–61]. Tissue harmonic imaging relies on that theory and mechanism.

2.3.6 Synthetic Aperture Imaging

In *Synthetic Aperture (SA)* imaging [53, 62–64], the ROI is acquired, and accordingly reconstructed, multiple times where each time one transducer element is active in transmission while all the transducer elements (or the same single element [64]) are simultaneously active in receive. Multi-element SA imaging is another form of SA where a group of elements are active in transmit - rather than a single element - at a time, and again all the elements are active in receive. The reconstruction of the final image is based on combining all these reconstructions. SA imaging improves significantly the contrast and resolution of the reconstruction by performing dynamic transmit (can even perform FP-by-FP Tx focusing) and receive focusing thanks to its mechanism. However, a major drawback of SA processing is its massive computation, memory, and bandwidth demands to output a single final image.

2.4 Literature Review and Previous Work

3D US imaging systems, either commercial or research-oriented, should in principle support a high input channel count, because a fully-populated, high-density matrix array can easily comprise thousands of elements [2]. However, no existing system is able to process the resulting stream of data, due to a variety of limitations including cost. This leads to quality trade-offs.

Typically, the channel count is significantly reduced, e.g. to a few hundreds, already within the piezoelectric probe. This can be achieved by different techniques. Analog pre-BF or micro-BF [52, 65–70] is the most common; given a fully-populated transducer, it adds up the signals received by a group of transducer elements, according to a fixed precomputed delay profile, and connects the output to a single channel towards the imager. The pre-BF analog output, which has much lower signal counts, is then used for digital BF. This reduces the wiring and computation complexity, but sacrificing the ability to focus - since combining the data of an element group according to a fixed profile is equivalent to fixing the focus of that group -, losing information and therefore impacts resolution and image quality.

An alternative approach is to use arrays that intrinsically feature fewer channels, or that deliberately choose to limit the number of accessible elements. For example, sparse 2D-arrays [71–73] and multiplexing [74, 75] choose the count and pattern of active receive elements per scan. However, it has been concluded that there is a direct relationship between the density of the probe elements and the quality of the reconstructed images due to reduced sidelobes level and narrowed mainlobe; therefore, a high channel count is still desirable. *Row-Column Addressed (RCA)*- or *Top-Orthogonal-to-Bottom-Electrode (TOBE)*-addressed arrays access an $N \times N$ matrix with just $2N$ signals, along the edges, instead of N^2 channels. This is achieved by accessing all the row elements together and all the column elements together, with an intrinsic averaging effect. RCA arrays drastically reduce the processing computation cost and the wiring challenge, but again at the cost of a more limited FOV, restricted focusing capability with higher sidelobes, and in general a reduced overall reconstruction quality [76–80]. Recently,

Compressed Sensing (CS) or Compressive sampling has been applied to US imaging [81–89], as a sub-Nyquist sampling and processing approach, with the aim of reducing the required acquired data while maintaining the reconstruction quality. Although CS shows promising quality improvement, the mechanism complexity, resource requirements, and computation time challenge its application in 3D imaging with matrix probes, especially if the aim is a portable and battery operated platform. Moreover, there is always a desire to relax the compression rate to gain more quality enhancement.

Other works [90–94] have shown that a feasible alternative is to try to compute all delay coefficients on-the-fly on-chip, but the challenge of supporting a high-channel-count realtime 3D BF on a portable platform remains daunting. Since this computation involves the evaluation of complex functions like square roots, it is mandatory to identify accurate, fast and low-area approximation circuits: [90, 95] present a recursive and iterative method to compute the square roots efficiently. In [96], while utilizing 4 Xilinx Virtex 5 FPGAs, only every 32nd delay is truly computed and the remaining delays are interpolated. [92, 94] calculate the delays based on a piecewise linear approximation with large bit-width multipliers suiting ASIC-based designs.

Even though channel-reduction techniques are ubiquitous and effective, their reconstruction quality cost means that the support for a higher channel count is still a desirable property. Moreover, and despite using channel-reduction techniques, current 3D US systems still end up bulky and power-consuming. On the commercial side, [2, 3, 19, 97, 98] are very advanced and provide full 3D support, but they are aimed at hospitals: they come on a base with wheels, they consume hundreds of watts and need to be permanently plugged to a power outlet, and are very expensive. Many commercial US machines that *are* portable, like the GE Voluson i [99], Samsung UGEO HM70A [100, 101], Samsung MySono U6 [102], and Chison Q9 [103], are essentially 2D imagers; they nominally offer a 3D feature by supporting mechanically-swept arrays with low channel count (e.g. 128 elements). This type of probes introduces major motion artifacts, since the acquisition of the whole volume takes about 1 second per frame, and is only suitable for applications like obstetrics, where the subject (the fetus) barely moves. Applications like cardiac imaging require high frame rate and high resolution at the same time, and therefore full 3D support. For example, the Philips CX50 [104] scanner has a mode for full 3D *Trans-Esophageal Echocardiography (TEE)*, which is considered as an invasive examination that needs not only the presence of a sonographer but also a physician, leveraging a matrix probe of 2500 elements, but analog pre-BF is exploited to compress this data onto only 100 receive channels [105] at a major image quality cost. Cephasonics provides the first US system supporting up to 4096 channels, called cQuest Griffin [106, 107], by stacking 64×64 -channel cQEngine modules. A 1024-channel cQuest Griffin consists of 16 cQEngine modules, consumes 640 W power, and has a size of $30\text{cm} \times 68\text{cm} \times 48\text{cm}$. Xilinx has also released a reference solution for a US imager architecture [108]. This solution leverages a *High-Level Synthesis (HLS)* flow, whereby the FPGA logic is inferred from human-written signal processing code. While this flow is valuable, the embodiment of [108] is not particularly efficient in terms of resources, requiring *two* Kintex Ultrascale KU060 FPGAs (i.e. two chips each approximately 1.5X as large as the KU040 used in this thesis [32]) to process 256 channels (as opposed to up

to 1024 in this thesis), for a compounded resource efficiency gap estimated at about 12X. This gap makes it impractical to adopt the Xilinx reference design for portable 3D imaging.

A few 3D US research systems have been proposed. They all reduce the receive channel count, yet still ending up bulky. For example, the recently-released 256-channel ULA-OP system [109] is implemented with 9 high-end FPGAs and 17 Digital Signal Processor (DSP)s with dimensions of $34\text{cm} \times 30\text{cm} \times 26\text{cm}$, for a weight of 16 kg. The powerful, flexible, and advanced research SARUS [91] platform supports 1024 receive channels, the highest count supported by any single 3D system, but requires 320 FPGAs and needs extensive cooling. The Sonic Millip3De system [110,111], that performs ultra-fast imaging, uses 128×96 probe elements - but only 1024 channels are considered per shot - with piecewise quadrature approximation and a powerful die-stacked package. However, its main limitation is the required large external DRAM memory to store the BF delays, and the need of several GB/s memory bandwidth. There are also few single-FPGA US research systems, but they support up to only 64 receive channels [112, 113]. Moreover, there are many US systems relying on software-based BF, running on *Graphics Processing Unit (GPU)*s [114, 115], multicore CPUs [114], or DSPs [116–118], but the resulting power budget is not optimal for battery operation, specially in 3D imaging. The DiPhas system [119], which supports up to 256-channel GPU-based processing and can be scaled by connecting multiple cabinets, also needs to be plugged in and is expensive. The Ekho *Application-Specific Integrated Circuit (ASIC)* pre-silicon 28nm layout [120] provides excellent efficiency in terms of area (1.68cm^2) and power (30W) when scaled to 10000-channel 3D beamforming. To achieve these results, it must adopt optimizations to the delay calculator, which are in this case based on a piecewise approximation, as well as other techniques, such as bandpass processing. However, the market size for US applications is probably too small to justify the manufacturing costs of such an ASIC in comparatively tiny batches. Therefore, the authors also proposed a mapping of the same architecture to FPGA [9]; the comparison in that paper, however, demonstrates that the architecture proposed in this thesis (which is currently even more efficient and complete than the one presented in [9]) is drastically better optimized for the FPGA environment, while in the case of Ekho, the delay generation logic alone would fill the FPGA.

It is desirable to have a fully-digital, maybe even software [121], and high-channel-count BF to dynamically set the focus position during receive. However, the large amount of input signals to be processed individually still poses a major computation, resources, and bandwidth challenges (refer to Section 1.3).

A smart and efficient BF technique is needed to achieve a compact and easily reproducible design, yet high-quality reconstruction. This should be the basis to start solving the question of a telesonography-capable platform. Further, each processing step in the imager should be optimized to yield overall platform compactness (ideally, single-chip) while being compatible with battery operation. In this research, an efficient and optimized method for each imaging step has been used to achieve overall platform efficiency, portability, and low power consumption. We built our system around our novel proposed BF technique (Chapter 4). The result

is an unprecedented 3D medical US platform of 1024-channel processing on a single FPGA and around 5 Watt power consumption. The proposed demonstrator is a complete digital back-end system that includes pre-processing, BF (core reconstruction), and post-processing processes. Our architecture could further be used in combination with one of the techniques described above to be compatible with transducers with even higher element counts.

2.5 Summary

In this chapter, essential US definitions and background have been highlighted to serve as an infrastructure for what is coming next of novel contributions and technical details. This includes the elucidation of common US processing pipeline procedures, where each procedure is tackled and optimized in the next few chapters in order to provide the aimed platform. Different US transducers and emission patterns, along with the prevalent medical US modes have been discussed. Moreover, a detailed literature review not only for the today's state-of-the-art 3D systems, both commercial and research, but also for the common methods and approaches used to solve the numerous calculation and resources necessities of 3D sonography, has been provided.

3 Matlab-based Imaging Pipeline and Algorithms Investigation

The initial steps towards reaching our goal of the first telephonography-capable platform have been taken within Matlab framework [122, 123]. In order to design a powerful and flexible US imaging system, development and testing in an environment such as Matlab is essential. This is needed to assess the most important algorithmic alternatives and their impact on the image quality and computation cost. Only later, select algorithms can be mapped onto a hardware/software platform, for example running off an FPGA. Even then, a simulation environment is still useful for debugging, the generation of specialized inputs, the evaluation of the outputs, and the exploration of new features.

We have developed a feature-rich Matlab environment that models complete imaging pipelines. Figure 3.1(a) and 3.1(b) show the developed US processing pipelines for both linear (2D) and phased (2D and 3D) imaging, respectively. Our Matlab-based US platform can be considered as a sandbox for investigating, innovating, testing, and evaluating different algorithms, settings, and modes. It facilitates the hardware development process, and expedites the innovation and testing of new techniques before the actual hardware implementation phase.

Several options - algorithmic and parametric - are supported by our pipeline. The following are examples of the major options:

- The use of linear imaging (2D) vs. phased imaging (2D and 3D), and the full control over the transmit focus (Figure 2.3), that can be a plane wave, a focused beam, a diverging beam, or any other focus patterns.
- The control of the number and pattern of active receive elements.
- The use of a single insonification per imaging frame versus zone or compound imaging (Section 2.3, where Section 6.3 shows their hardware translation).
- The use of the traditional delay-and-sum BF method based on the exact delay calculation algorithm (i.e. square-roots calculation) or our proposed *Steering-based Hardware-Efficient Delay Approximation (SHEDA)* algorithm (Chapter 4).

Chapter 3. Matlab-based Imaging Pipeline and Algorithms Investigation

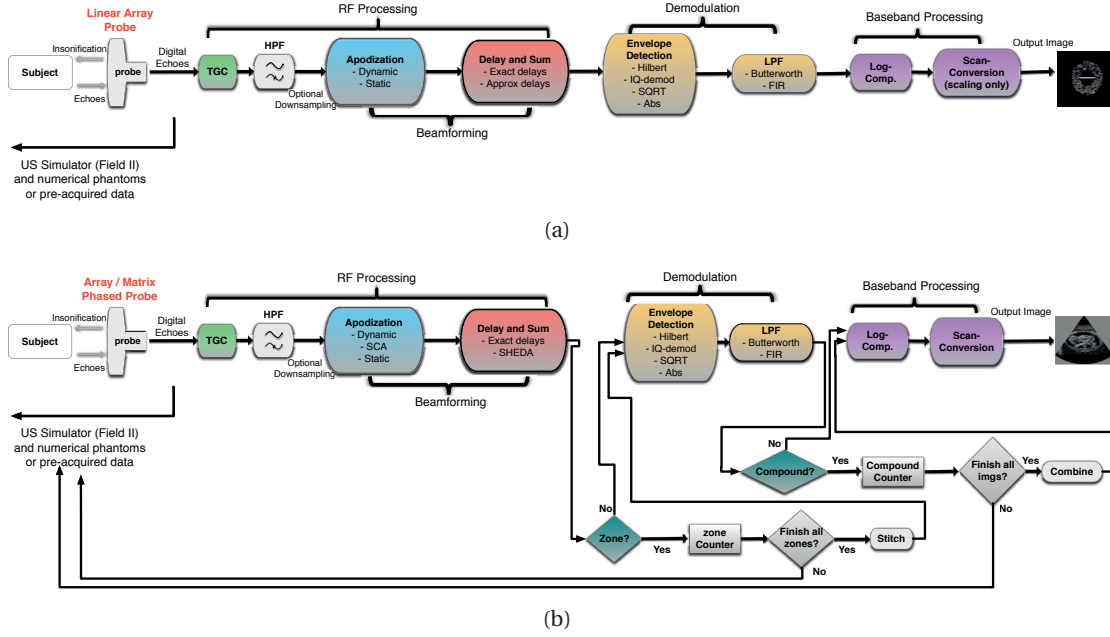


Figure 3.1: Our Matlab-based US imaging pipeline. (a) 2D linear imaging pipeline using *1D linear* array transducer. (b) 2D/3D phased imaging pipeline using *1D/2D phased* array transducer.

- The possibility to choose between various apodization models (Section 5.1); dynamic, static, or *SHEDA-Correction Apodization (SCA)* (for 3D only).
- The opportunity to choose between various combination of methods for the signal transformation - Hilbert vs. IQ-demodulation vs. square-root vs. absolute value - and the low-pass filtering - Butterworth vs. *Finite Impulse Response (FIR)* filter - blocks in the demodulation process.

On the other hand, the developed Matlab-based *phased* pipeline supports the hardware design by preparing some pre-defined tables (the correction coefficients for the SHEDA approach illustrated in Chapter 4, and the static apodization and TGC coefficients discussed in Chapter 5) and setting scripts to be used by our single-FPGA digital imager. Figure 3.2 depicts the workflow between our Matlab-based US imaging pipeline and the single-FPGA digital imager. Further, the quality assessments of our prototype for (i) the delay-calculation (Section 4.4), (ii) the apodization schemes (Section 5.1), and (iii) the whole design in different imaging modes (Section 6.4), are fully performed on the Matlab side by providing a golden reference - based on exact reconstruction (exact delay calculation and dynamic apodization) - to evaluate against, and various quality metrics to use (PSF, PSNR, CR, and visual assessment). Other reconstructions are also provided by combining the algorithmic options mentioned before such as the imaging based on exact delay calculation and static apodization, or SHEDA delay calculator with dynamic / static / SCA apodization.

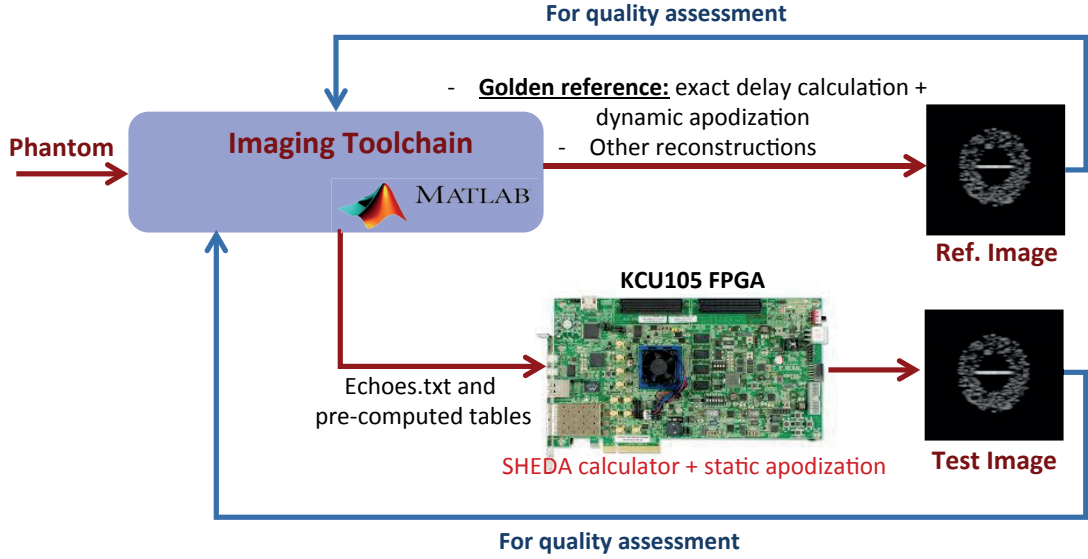


Figure 3.2: The workflow between our Matlab-based imaging pipeline and the single-FPGA design. Digital echoes in addition to other pre-defined tables are provided by our Matlab design to the single-FPGA imager. The Matlab pipeline provides a golden reference for the assessment of our single-FPGA imaging quality.

Our complete Matlab-based US processing pipelines are openly accessible on [124]. They are self-contained, include a detailed "howto", and are ready to be exploited for further algorithmic exploration, innovation, development, and evaluation.

Due to the unavailability of real input data - especially 3D data - during most of the research period, we resorted to the usage of predefined synthetic phantoms (Figure 3.2). We have generated synthetic phantoms directly within the Matlab environment. A synthetic phantom is a defined collection of scatterers in space, with configurable reflectivity. The advantage of synthetic phantoms is that they can be arbitrarily configured, allowing for objective comparisons between the known input structure and the final reconstructed image, which is not possible when using real US data. We have created a small database of 3D phantoms for development and testing purposes. The Field II software [125–127] is then used to simulate the insonification of the phantom.

Field II [125–127] is a US simulator that runs on Matlab. It emulates US fields - both emitted and received pulse-echo - and their characteristics (attenuation, lobes, etc.). Field II allows the definition of US transducers with high design flexibility to control the probe dimensions, specifications (center frequency, etc.), and number of elements. This includes the modeling of probes for 3D imaging that cannot be physically bought as they are either too expensive or unavailable for research purposes. The output of a Field II simulation is a set of pressure signals sampled in time. It should be noted that a Field II simulation, while highly accurate

and representative, does not model some of the phenomena occurring during a real insonification; for example, it does not generate harmonics of the transmitted pulse (thus, we haven't implemented tissue-harmonic imaging mode - Section 2.3.5), it does not model multiple reflections, it does not directly model variance in the speed of sound in different tissues, and it does not directly factor in any electronic or acoustic noise. For any study where these effects are of particular concern, real data must be used.

In this chapter, we present few examples of the experiments performed on our Matlab pipeline. The goal is to present an overview of how imaging parameters affect the subjective quality of the results, while at the same time estimating the computation cost via the runtime of the Matlab simulation. We do not aim to identify configurations that are “best”, because each of them is likely to be useful in some scenarios, but rather to assess the quality/computation trade-off, in view of a final miniaturized implementation able to switch modes and tuning parameters based on the available resources and on the currently displayed image.

In these experiments, we insonify with Field II a synthetic phantom consisting of a hollow sphere, of 2 cm outer diameter and 1 cm inner diameter, crossed by a wire (Figures 3.3, 3.4, 3.5, and 3.6). The computation cost is evaluated by measuring the runtime of the Matlab code that is in charge of image reconstruction (i.e., excluding the runtime of the Field II simulation, which is irrelevant for our purposes). We used Matlab R2016b [123] on a 3.1 GHz Intel Core i7 with 16 GB of DDR3 RAM at 1867 MHz, averaging five runs of each experiment. Obviously, these execution times give a very rough estimation of the actual computation costs. However, in our experience, we have generally noticed a correlation between variations of Matlab runtime and the projected amount of software calculations or hardware resources that would be needed in the corresponding imaging scenarios. Thus, we consider Matlab runtime a good proxy to estimate how various parameters influence performance, at least in relative terms.

3.1 Active-Elements Pattern in Receive

In this experiment, for a linear array of 96 elements, we investigate the effect of choosing different patterns and numbers of *active* elements in receive mode, i.e. keeping some of the 96 elements inactive. Note that, in transmit, it is not beneficial to do so (inactivate some of the transmit elements), where the wave is emitted at no particular *computation* cost, unless a specific imaging mode is aimed - like synthetic aperture imaging (Section 2.3.6). However, in receive mode, the BF cost can be reduced proportionally to the number of inactive elements, and the interface between the probe and the processing system will be much simpler and cheaper (interfacing resources, input memory requirements, etc.). In Figure 3.3, the effect of various patterns on the reconstruction quality is shown, while in the top six rows of Table 3.1, the corresponding imaging runtime (BF and SC) is reported.

Figure 3.3(a) shows the best possible image quality, when all the 96 elements are active. Figures 3.3(b) and 3.3(c) show the reconstruction with a smaller receive aperture, by using only the central 32 and 16 elements, respectively. A reduced aperture always results in a loss

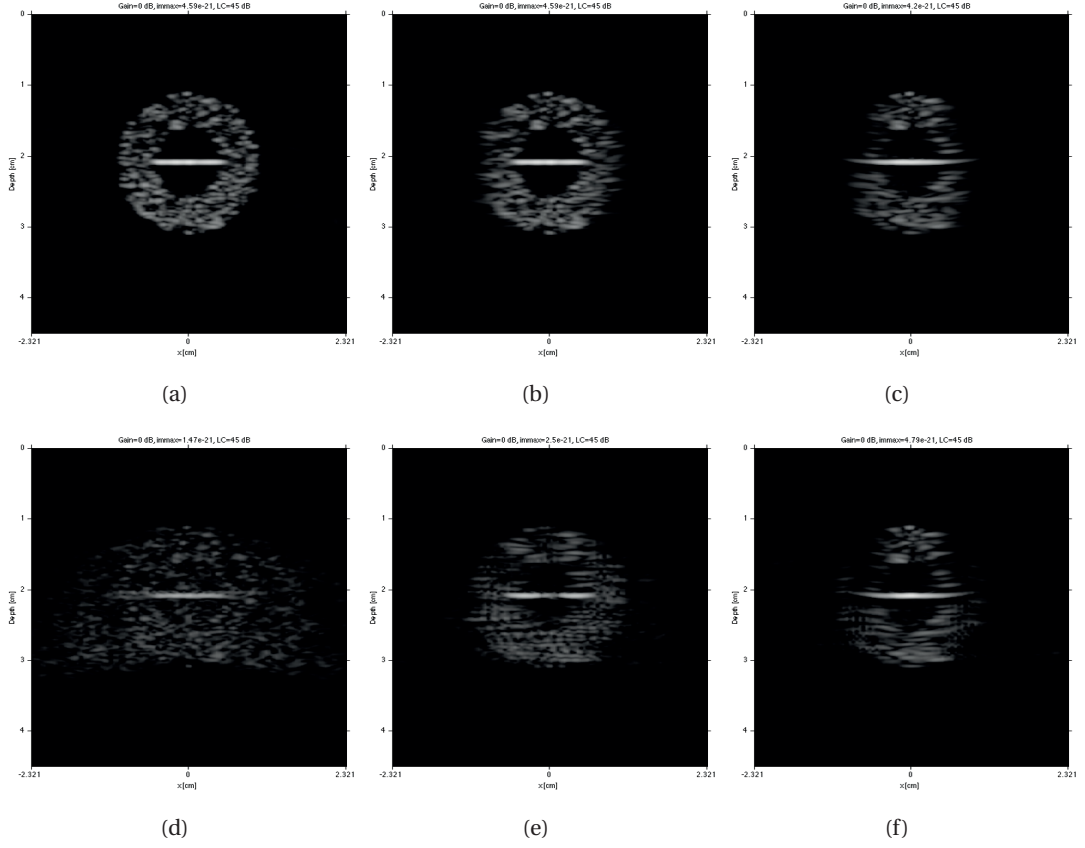


Figure 3.3: Reconstructions based on different number and pattern of *active* transducer elements in receive, and the consequent quality impact. (a) 96 out of 96. (b) central 32 out of 96. (c) central 16 out of 96. (d) 1 every 3. (e) 6 every 16. (f) 12 every 32. A 96-element linear array probe is used of $f_o = 3.5$ MHz and the echoes are sampled at $f_s = 200$ MHz. The full aperture is active in transmit.

of lateral resolution. In the extreme case of using only 16 elements, it reduces the ability to image the edges of the phantom, which are only partially acquired by the narrower receive profile. A “naive” activation pattern where only one element every three is active (Figure 3.3(d)) does “see” the whole volume, but results in unacceptable speckle due to the emergence of so-called *grating lobes*. Grating lobes are large sidelobes that have comparable size to the central main lobe. Therefore, they severely affect the directional selectivity of the probe, leading to artifacts that can be major. The grating lobes’ intensity depends on the periodicity of the active elements. Another possible arrangement is to use multiple clusters of active elements, like 6 every 16 elements (Figure 3.3(e)) or 12 every 32 (Figure 3.3(f)), in both cases with a total active element count of 36. These arrangements incur less speckle than using 1 active element every 3, while saving a comparable amount of calculations; however, their coverage of the volume and lateral resolution are more compromised (compared to Figure 3.3(a)).

Concerning the runtime, as expected and by referring to Table 3.1, the computation cost

depends only on the active element count, not on the pattern. Overall, depending on the clinical requirement on the ROI size, the interfacing capability, and the acceptable quality loss as a cost of the gaining time and saving resources, different trade-offs are available.

The idea of activating select elements in receive mode is the intrinsic concept behind the multiplexing and spare arrays approaches used to work around the high computation requirements and interfacing challenges in 3D imaging (Section 2.4).

Table 3.1: Runtime of the imaging flow (BF and SC) for different elements count in receive and array probe types.

Array	TX focus	RX active	Avg runtime
Linear	Plane	96/96	2.53 sec
Linear	Plane	32/96	1.86 sec
Linear	Plane	16/96	1.69 sec
Linear	Plane	1/3 × 32	1.86 sec
Linear	Plane	6/16 × 6	1.96 sec
Linear	Plane	12/32 × 3	1.96 sec
Phased	Focused	32	2.55 sec
Phased	Focused + brightness comp.	32	2.62 sec
Phased	Diverging	32	2.6 sec
Phased	Zone imaging	32	2.62 sec

3.2 Phased Arrays and Zone Imaging

In this experiment, we demonstrate phased insonification options and the consequent reconstruction quality, in addition to zone imaging (Section 2.3.3) trade-offs. We utilize a simulated 32-element phased array, with $f_0 = 3.5$ MHz and $f_s = 200$ MHz. The main advantage of the phased array probes is the wider directivity of their composing elements (Section 2.1) which allows the imaging of large FOVs using small probe footprint. This is in addition to their strong focusing and steering capabilities.

Figure 3.4(a) shows the reconstructed phantom when using a focused beam (i.e. converging profile) in transmit. A focused beam yields maximum resolution in the focused area, since the acoustic pressure is highest, but since less energy is used to insonify the rest of the volume, the unfocused regions exhibit lower resolution and brightness. The brightness only can be compensated very cheaply by applying a brightness adjustment profile (Figure 3.4(b)). Alternatively, if a diverging beam is used in transmit (Figure 3.4(c)), the volume can be insonified more evenly, resulting in a more consistent frame quality. The choice depends mainly on the clinical interest of identifying small features in a precise area, or rather of studying a broad volume.

In addition, the output of the zone imaging technique (Section 2.3.3) is investigated, whereby a

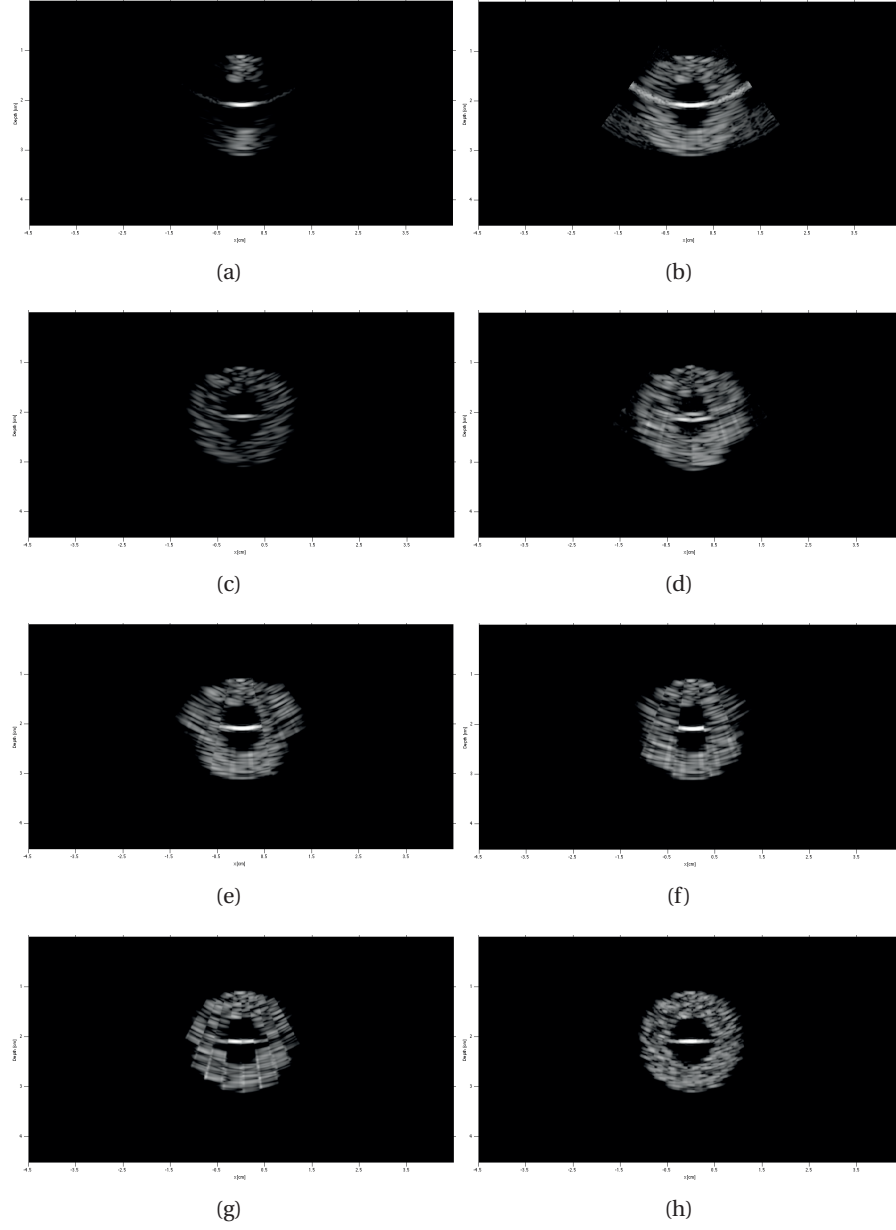


Figure 3.4: Phased reconstruction with focused and diverging insonification profiles, for single-zone and multi-zone imaging; (a)-(c): single insonification per frame; (d)-(h): zone imaging of 2-50 zones, each is a circular sector. (a) Focused Tx. (b) Focused Tx, with intensity compensation. (c) Diverging Tx. (d)-(h) Zone imaging of 2, 3, 5, 10, and 50 zones, respectively, while employing focused insonification profiles.

single frame is reconstructed by stitching multiple sub-frames, each computed from a separate insonification with optimized focus. In Figures 3.4(d)-3.4(h), the resulting frame is a composite of 2-50 zones, each being a thin circular sector. Since we use focused insonifications - like those of Figure 2.8 - and we do not apply any blending across the zones, which should normally

be done, it is easily possible to detect abrupt transitions and artifacts at the edges of the zones, until the number of zones becomes very high (Figure 3.4(h)). Increasing the number of zones also helps resolution since a larger percentage of the frame is in focus.

From the computation standpoint (the four bottom rows of Table 3.1), it can be seen that the runtime does not vary much; indeed, the total number of beamformed pixels per frame remains the same regardless of the transmission-profile focus or zone imaging choices. Brightness compensation and zone stitching are both very cheap operations and they do not skew the results substantially. On the other hand, it is important to remember that in the case of zone imaging, the number of insonifications to reconstruct one frame is equal to the number of zones. Therefore, even if the BF workload per frame remains constant, the maximum achievable frame rate will definitely be impacted. It can be noted that the runtime of the 32-element *phased* processing is different than that of *linear* processing. Indeed, it is due to the differences in the SC process in both cases, in addition to some differences in the BF reconstruction itself.

3.3 3D Reconstruction Resolution and Element Count

Imaging runtime is definitely highly dependent on the BF resolution; i.e. the number of FPs to be reconstructed. The computation cost can be drastically reduced if the reconstruction resolution is lowered. We confirm this prediction by simulating a 16x16 matrix phased probe for 3D imaging, while varying the axial resolution of the beamformed images. The resulting images are shown in Figure 3.5, and the BF runtime is recorded in Table 3.2. Lower resolutions degrade the image quality, although not as much as could be expected, even at extremely low values. It is impossible to devise an ideal resolution value in a general way. The guiding principle should be to match the physically achievable spatial resolution, which depends on the probe's element count, element arrangement, center frequency, imaging modes and settings, etc. Note that the runtime does not depend linearly on the axial resolution of the beamformed image, as could be expected. The reason is that our innovative SHEDA method (Chapter 4) - which is the main building block in the BF process - dramatically saves computation complexity and load, but incurs a fixed calculation overhead which is not resolution-dependent.

Table 3.2: 3D BF runtime as a function of the desired axial resolution. 11688 is the maximum possible resolution, by reconstructing a pixel for every time sample of the input echoes, considering the f_s and imaging depth of this experiment (45 mm).

Axial Resolution	11688 pixels	500 pixels	100 pixels	50 pixels
Runtime	17.26 min	1.15 min	24.42 sec	19 sec

Further, volumetric imaging depends heavily on the number of probe elements, especially if no pre-BF get applied (Section 2.4); i.e. all the data input get processed independently. Figure 3.6 shows the reconstruction quality of 3D images acquired using 16x16 and 32x32 probes, where

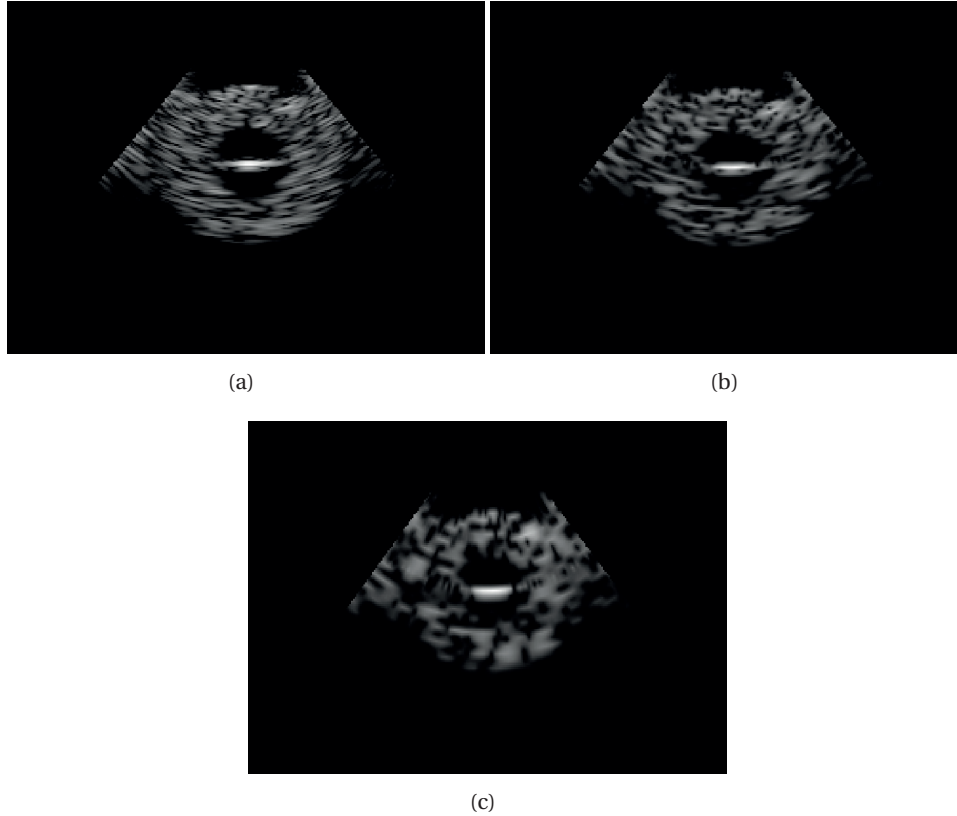


Figure 3.5: 3D imaging with a 16x16 matrix phased array, and a variable number of beam-formed points in the axial direction; (a) 500 points, (b) 100 points, and (c) 50 points. The images show the middle transverse plane (azimuth-radial plane) of the reconstructed 3D volume.

the BF runtimes on Matlab are 1.1 mins and 3.87 mins, respectively. The runtime of the core BF routine is found to be linearly proportional to the number of active elements in the probe, as expected in theory with a little overhead in the BF algorithm itself (0.18 min).

3.4 Summary

In this chapter, our developed Matlab-based US imaging platform has been introduced. Three pipelines have been implemented on Matlab environment; 2D linear, 2D phased, and 3D phased imaging pipelines. Various algorithms have been developed and assessed *efficiently* - in terms of the development time and effort - before the hardware realization. The trade-offs of processing options, parameters, and settings have been studied. The detailed quality assessments of the teleosonography-capable platform have been exclusively performed on Matlab. This is in addition to the preparation of pre-defined tables for the FPGA imager.

This chapter have illustrated a few of the possible modes of operations of our Matlab toolkit.

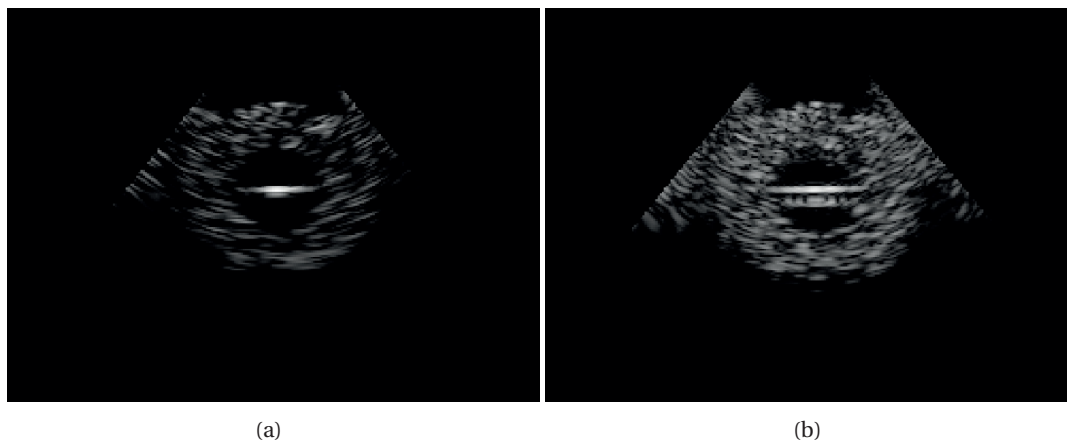


Figure 3.6: 3D imaging with (a) 16x16 and (b) 32x32 matrix phased probes. The images show the middle transverse plane (azimuth-radial plane) of the reconstructed volume.

The experiments presented here are; (i) the variation of the number and pattern of active elements in receive in linear imaging, (ii) the phased imaging of diverseinsonification focus, (iii) the zone imaging while varying the number of zones, (iv) the 3D reconstruction while tuning the BF resolution, and finally, (v) the change of the number of elements in matrix probes. The experiments allowed to evaluate quality/complexity trade-offs before hardware implementation.

4 SHEDA - Steering-based Hardware-Efficient Delay Approximation Calculator

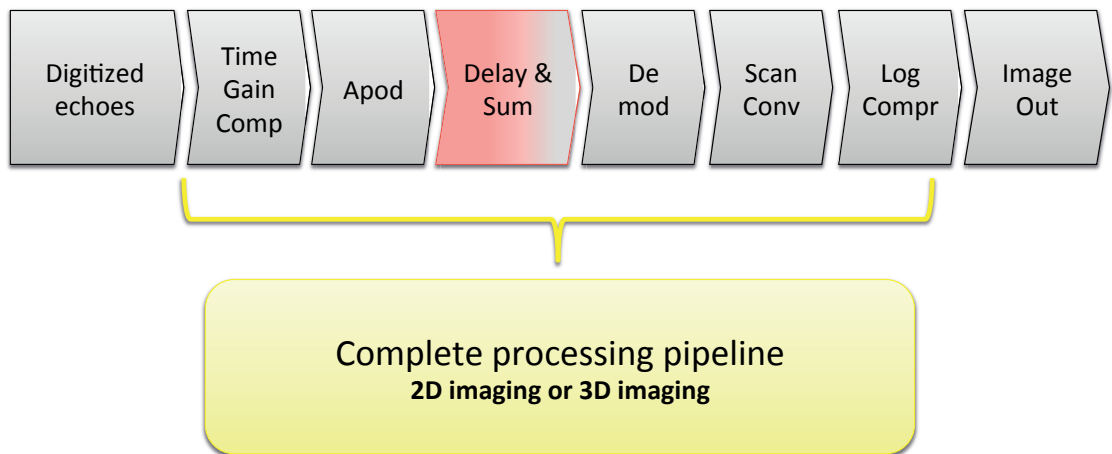


Figure 4.1: Logical processing flowchart of the US image reconstruction pipeline.

In volumetric US, both the BF and the SC (Section 6.2) procedures are main reasons for the high power, cost, and area requirements. The BF process includes three main stages; apodization, delay calculation, and summation. The delay calculation is the most demanding among the three, followed by the apodization (Section 5.1). As an example, in 3D imaging, a straightforward implementation of the delays t_p in Eq. (2.1) - for a reasonable imager configuration and frame rate - involves the need to calculate about 63 billion delays/sec (Section 1.3.3). Each delay is the time taken to travel from the origin O to a scatterer S plus from the scatterer S to any of the transducer element D . This requires calculating Euclidean distances (i.e. square-roots) divided by the speed of the traveling sound in the medium. Since the sound wave is typically assumed traveling in a constant speed c , the delay calculator can

be considered as a generator for 63 billion *square-roots per sec*. Indeed, it is quite challenging to fit such a generator - with also other demanding blocks - on a single self-contained board without innovative ideas and techniques.

In this chapter, a novel delay calculation algorithm has been proposed. The algorithm relies on simplifying the square-root calculation, into far fewer square-roots and additions between tables of pre-computed values (Section 4.1), by means of utilizing Taylor approximation. An efficient FPGA architecture has been accordingly designed (Section 4.3). An extensive evaluation for the algorithm and architecture inaccuracies has been performed, both qualitatively and quantitatively (Section 4.2 and 4.4).

4.1 Working Principle

Delay calculation is the calculation of both the transmit Tx delay $t_p(|\vec{OS}|)$ and receive Rx delay $t_p(|\vec{SD}|)$. These delays are used as indices for the raw data to be accordingly summed (Eq. (2.1)) to determine both the scatterers' location and reflectivity.

4.1.1 Receive Delay

The RX delay $t_p(|\vec{SD}|)$ is much more critical, since it must be evaluated for a varying scatterer location S and transducer element $D = (x_D, y_D, 0)$, i.e. about 2 billion times per volume.

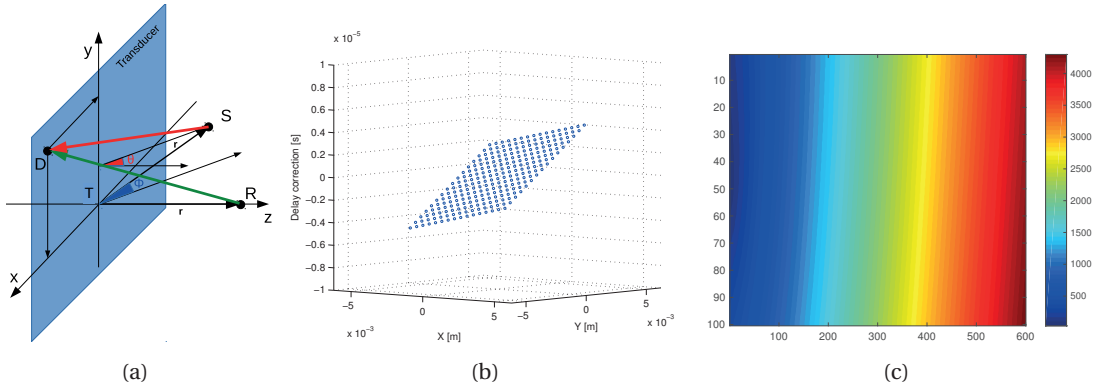


Figure 4.2: (a) Propagation delays must be calculated between each S and each element D of the transducer. The reference delays are the delay values for points R on the Z axis. For a point on another line of sight, the delay can be computed from the reference delay table plus an angle-dependent offset. (b) When considering both θ and ϕ steering, the required compensation is a plane, whose inclination around the origin is a function of θ, ϕ . (c) A section of the compensated delay table for a steering angle, where the x-axis indicates the depth in time samples and the y-axis represents the probe elements in the azimuth direction. The color-map represents the two-way delay values.

Let us assume that the three coordinates originate at point $T = (0, 0, 0)$, at the center of

the transducer surface. In order to tackle the bottleneck of the Rx-delay calculations, we have proposed - by means of approximation - an efficient delay calculation algorithm, called *Steering-based Hardware-Efficient Delay Approximation (SHEDA)* algorithm. Our SHEDA approach is based on calculating a set of *reference delays* that represent the receive delays for the set of points $R = (0, 0, r)$ along the central scanline that coincides with the Z axis. For the receive delays for the points along any other scanline, a correction should be added (Figure 4.2(b)). This correction could be seen as "steering" for the reference delay table, which is the reason behind the naming of the method. The steering approach is known from literature on 2D ultrasound imaging [128], and we first proposed to exploit it for 3D imaging.

The problem to be solved now is to find the correction factor to be able to beamform a point S that is on a steered line of sight at azimuth and elevation angles; θ and ϕ , respectively. This can be solved by referring to Figure 4.2(a) and considering a point R along the reference line of sight at the same distance from the transducer's center T ($r := |\vec{RT}| = |\vec{ST}|$), where¹:

$$T = (0, 0, 0); R = (0, 0, r); D = (x_D, y_D, 0); S = (r \sin \theta, r \sin \phi \cos \theta, r \cos \phi \cos \theta). \quad (4.1)$$

Note that the reference delays are the Rx delay value for R. The delay for the point S can thus be expressed as the reference delay table of point R with the addition of a correction factor, as follows:

$$t_p(S, D) = t_p(R, D) + \frac{|\vec{SD}| - |\vec{RD}|}{c}, \quad (4.2)$$

where

$$|\vec{SD}| = \sqrt{(x_S - x_D)^2 + (y_S - y_D)^2 + (z_S - 0)^2} = r \sqrt{1 + \frac{x_D^2 + y_D^2}{r^2} - \frac{2x_D \sin \theta + 2y_D \sin \phi \cos \theta}{r}}, \quad (4.3)$$

and

$$|\vec{RD}| = \sqrt{(0 - x_D)^2 + (0 - y_D)^2 + (z_R - 0)^2} = r \sqrt{1 + \frac{x_D^2 + y_D^2}{r^2}}. \quad (4.4)$$

The correction value we seek is thus:

¹The coordinate expressions depend on how the volume is swept, e.g. azimuth-first or elevation-first. We assume here azimuth-first sweeping.

$$\begin{aligned}
 t_p(S, D) - t_p(R, D) &= \frac{|\vec{SD}| - |\vec{RD}|}{c} = \\
 &= \frac{r}{c} \sqrt{1 + \frac{x_D^2 + y_D^2}{r^2} - \frac{2x_D \sin \theta + 2y_D \sin \phi \cos \theta}{r}} - \frac{r}{c} \sqrt{1 + \frac{x_D^2 + y_D^2}{r^2}}. \quad (4.5)
 \end{aligned}$$

This cannot be further simplified, but a Taylor expansion [129–131] can be used:

$$\sqrt{1+x} \approx 1 + \frac{1}{2}x - \frac{1}{8}x^2 + \frac{1}{16}x^3 + \dots, |x| < 1 \quad (4.6)$$

where the condition on x means that, if increasingly high-order polynomials are used, the expansion converges towards the root function only in the interval $-1 < x < 1$. This is a required condition for convergence of the expansion with an infinite number of terms, but is inconsequential here since we only propose to use a first order polynomial. However, the choice of a first-order approximation *does* incur an inaccuracy, which is discussed in Section 4.2. By using the first-order expansion:

$$\begin{aligned}
 t_p(S, D) - t_p(R, D) &\approx \frac{r}{c} \left(1 + \frac{x_D^2 + y_D^2}{2r^2} - \frac{2x_D \sin \theta + 2y_D \sin \phi \cos \theta}{2r} - 1 - \frac{x_D^2 + y_D^2}{2r^2} \right) = \\
 &= \frac{r}{c} \left(-\frac{x_D \sin \theta + y_D \sin \phi \cos \theta}{r} \right) = -\frac{x_D \sin \theta}{c} - \frac{y_D \sin \phi \cos \theta}{c}. \quad (4.7)
 \end{aligned}$$

This derived formula is very efficient because it reduces complex square root calculations to just a lookup in a small table (reference delay) plus two additions of correction coefficients. For 2D imaging, the reference delay table is a 2D matrix with dimensions $e_x \times d_p$; for 3D imaging, a 3D matrix with dimensions $e_x \times e_y \times d_p$, i.e. $32 \times 32 \times 500 = 510 \times 10^3$ elements. Therefore, the reference delays can be pre-calculated and stored in a reasonable table size, or calculated on the fly as we realized in our final implementation (Section 4.3). Since the possible values of ϕ, θ, x_D, y_D are discrete and few, the correction terms can be fully pre-calculated and also stored in small tables as our realization - Section 4.3 - (or even calculated on the fly).

4.1.2 Transmit Delay

For a specific emission origin O and to reconstruct a single volume V , Tx calculation is less demanding than Rx calculation by a factor of the number of transducer elements D . Tx calculation depends only on $S = (r, \theta, \phi)$, while O is fixed. In 3D imaging and according to Table 1.1, for a single transmission origin O , 2 million Tx delays need to be calculated versus

2 billion Rx delays *per volume*. Therefore, we calculate TX delay $t_p(|\vec{OS}|)$ in full exact form on-the-fly, i.e. with square root calculations, since the computational cost is manageable.

4.2 Accuracy Bound

Using a first-order Taylor approximation for the delay calculation introduces inaccuracy. To control this issue, it is natural to attempt to formally bound the degree of inaccuracy. A common way to do so is by using the Lagrange bound on the Taylor remainder. Unfortunately, although a formulation of this bound can be derived, the bound diverges to infinity (Appendix A - Section A.1) when $r \rightarrow 0$. Therefore, a different bounding approach is required.

Note that the original function $f(x) = \sqrt{1+x}$ and its first-order expansion $f_1(x) = 1 + \frac{1}{2}x$ are always positive. This can be seen because the expression $(1+x)$ is the square of a distance, see (4.3) and (4.4). It can also be immediately seen that the largest approximation error occurs for $x \rightarrow \infty$, with both functions diverging to infinity, $f_1(x)$ much more quickly than $f(x)$. Therefore, the approximation can be bounded to

$$|E_{f_1}(x)| = f_1(x) - f(x) \xrightarrow{x \rightarrow \infty} f_1(x). \quad (4.8)$$

As mentioned previously, we have approximated two functions, $h(x)$ in (4.3) and $g(x)$ in (4.4). The error bounds for each of those approximations are:

$$|E_{h_1}(x)| \leq 1 + \frac{1}{2}x_h, \quad |E_{g_1}(x)| \leq 1 + \frac{1}{2}x_g. \quad (4.9)$$

The total error is the difference of the errors on $h(x)$ and $g(x)$, because these two functions have the same sign and the error must be calculated in the same location x . Thus,

$$\begin{aligned} |E(x)| &\leq |(1 + \frac{1}{2}x_h) - (1 + \frac{1}{2}x_g)| = \frac{1}{2}|(x_h - x_g)| = \\ &= \frac{1}{2} \left| \left(\frac{x_D^2 + y_D^2}{r^2} - \frac{2x_D \sin \theta + 2y_D \sin \phi \cos \theta}{r} - \frac{x_D^2 + y_D^2}{r^2} \right) \right| = \left| \frac{x_D \sin \theta + y_D \sin \phi \cos \theta}{r} \right|. \end{aligned} \quad (4.10)$$

Looking back at (4.5), we can express the error in time units by multiplying by r over c :

$$|E(x)| \leq \left| \frac{x_D \sin \theta + y_D \sin \phi \cos \theta}{c} \right|, \quad (4.11)$$

which does yield a finite bound on the Taylor expansion inaccuracy, as will be quantified in Section 4.4.1. Section A.2 of Appendix A shows more graphical and mathematical details about the derivation of our bounding approach.

4.3 FPGA Architecture

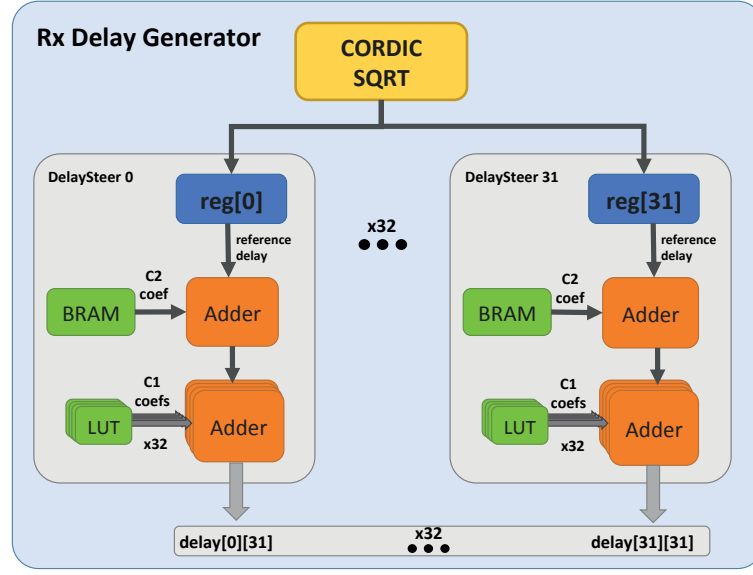
The SHEDA method for calculating the delays is computationally and materially efficient because it simplifies the numerous complex square roots to just a calculation of a small reference set of delays plus two additions. Since the possible values of θ , ϕ , x_D , and y_D are discrete and few, the correction terms can be fully pre-calculated and stored in small tables.

The delay calculation logic must first of all compute the reference Rx delay value $t_p(R, D)$. This delay is itself the output of a square root computation, but is much more slowly-varying than the desired $t_p(S, D)$ as it holds constant over a nappe of 64×64 voxels. Therefore, we can afford to implement this square root on a Xilinx CORDIC core (Figure 4.3(a)), minimizing design effort. Note that this calculation on-the-fly is an improvement over our preliminary architecture in [132], where the reference delay was fetched from an off-chip table, resulting in memory bandwidth issues. We chose to use the “optimum” pipelining configuration of the CORDIC core; this saves area and latency in return for a lower operating frequency, that we still found to be in excess of 133 MHz. The delay calculation architecture shown in Figure 4.3(a) is composed mainly of 32 sub-blocks, offering high parallelization; each contains a Xilinx *Block Random Access Memory (BRAM)* in which we store pre-calculated elevation correction coefficients ($c_2 = \frac{y_D \sin \phi \cos \theta}{c}$), and *LookUp Table (LUT)*s for storing pre-calculated azimuth correction coefficients ($c_1 = \frac{x_D \sin \theta}{c}$). Since the size of the c_2 table is much larger than the c_1 table, we used BRAMs instead of LUTs to save logic. Using adders, for each elevation step, we add the stored c_2 to the reference delays and then for each azimuth step we add the stored c_1 .

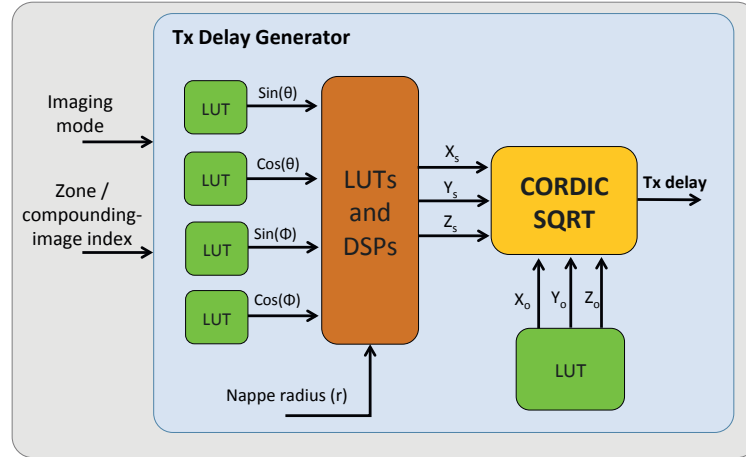
The TX delay computation $t_p(O, S)$ is not critical in terms of resources, since it needs to be performed at a much lower throughput than the RX delay computation. To minimize the design effort, the Tx delays are calculated by mapping the coordinate squaring onto the FPGA’s DSP48 slices, while using directly another Xilinx CORDIC core for square roots calculation, as seen in Figure 4.3(b). The location of each scatterer $S = (x_S, y_S, z_S)$ (as a function of the current azimuth and elevation angles θ , ϕ) and of the current emission origin $O = (x_O, y_O, z_O)$ are resolved and used as inputs. Many US imaging techniques exploit different transmit strategies, e.g. diverging insonification or steered plane waves, and sometimes rely on repositioning the origin freely at every insonification, e.g. in zone-, compound-, ultrafast-, or synthetic aperture imaging. Depending on the imaging mode (Section 6.3), the initialization of the azimuth θ and elevation ϕ pointers, as well as the emission origin, changes.

To minimize additional computations, the delay is directly computed in samples, i.e. the input coordinates of S and O are pre-multiplied by the sampling frequency and divided by the speed of sound. Finally, the RX and TX delays are summed. Note that a single TX delay, valid for a point S , is summed to many \overrightarrow{SD} RX delays. The architecture works identically for 2D imaging, setting ϕ and y_D to zero. However, to simplify the job of the synthesis tools while ensuring resource efficiency, we use an *Register-Transfer Level (RTL)* parameterization to automatically instantiate a simplified architecture for 2D imaging.

The delay values are used as an index into an echo buffer (Section 5.3) containing 2600



(a)



(b)

Figure 4.3: The SHEDA-based delay-calculation architecture. (a) Rx delays are computed by adding the two steering coefficients c_1 and c_2 to exactly-calculated reference delays. (b) Tx delay calculator, which is based on Xilinx CORDIC IP. The sum of Tx and Rx delays is used to index the input samples in the BRAMs of Figure 5.11.

samples/channel, corresponding to a 20 MHz sampling of the two-way sound propagation time ($2 \times 260\lambda$). This requires the addressing to have a bit-depth of 12 bits. For efficient sum operations, in terms of performance vs. logic, a fixed-point representation is useful. Let us assume for the moment, without loss of generality, a 18-bit design, which fits well one of Xilinx's selectable BRAM bank widths and gives also the flexibility to increase the depth of

the sample memory by increasing the sampling frequency and/or the imaging depth. The reference delays are always positive, thus they can be stored in 13.5 unsigned format and they can be sign-extended at the moment of applying the correction. The correction coefficients, which may be negative, must be stored with a signed ± 13.4 representation.

4.4 SHEDA Accuracy Evaluation

The SHEDA approach has two causes of inaccuracy; one is introduced by the first order Taylor approximation, and the other is due to the fixed-point representation of the delays (including the final rounding to integer indices). We have evaluated the algorithmic approximation by quantifying numerically the inaccuracy bound (Section 4.4.1) and assessing the PSF metric. In addition, in Section 4.4.3, different fixed-point resolutions have been evaluated. This helped on deciding the representation at which the delays (reference and correction coefficients) are defined on the eventual hardware implementation. Further, the total error for the proposed approach has been quantified and a visual assessment has been performed in Section 4.4.4.

Although the final FPGA implementation of our digital imager - including the delay-steer algorithm (SHEDA) - is based on the settings specified in Table 1.1, the performed assessments (Sections 4.4.1, 4.4.2, 4.4.3, and 4.4.4) for the proposed delay calculation approach are based on a further scaled up version of the 3D design. In this accuracy study, the probe comprises 100×100 elements with 32 MHz sampling frequency and imaging volume of $73^\circ \times 73^\circ \times 500\lambda$ beamformed for $128 \times 128 \times 1000$ FP. The rest of the specifications hold. The number of probe elements, the sampling frequency, the imaged FOV, and the BF resolution have been scaled up to allow extensive investigation of the inaccuracy at different scatterers' location, hence, achieving comprehensive testing and verification of the algorithm.

4.4.1 Accuracy Bound Evaluation

The main cause of inaccuracy in the SHEDA method is the inaccuracy due to the algorithmic approximation in using the first-order Taylor polynomial to “steer” the reference delays. In Section 4.2, we demonstrated the theoretical bound of the Taylor approximation inaccuracy and we represented it by (4.11). To get the maximum error of the approximation theoretically, D should be at one of the four corners of the probe (i.e. $\pm x_{Dmax}$ and $\pm y_{Dmax}$) and at $\pm \theta_{max}$ and $\pm \phi_{max}$, yielding an error bound as follows (refer to the Appendix for more details):

$$|E| = \frac{0.0103274}{1540} = 6.71\mu s \quad (4.12)$$

which at the target sampling frequency of 32 MHz, equals 215 signal samples. This degree of inaccuracy is unacceptable. Figure 4.4(a) shows the regions that incur inaccuracies due to the SHEDA calculation approximation. The color map of the inaccuracy distribution is based

on the fact that any contribution of any element with a sampling error beyond 2 samples² is essentially noise. Thus, if the sampling error is known upfront, the element samples are better discarded than summed in.

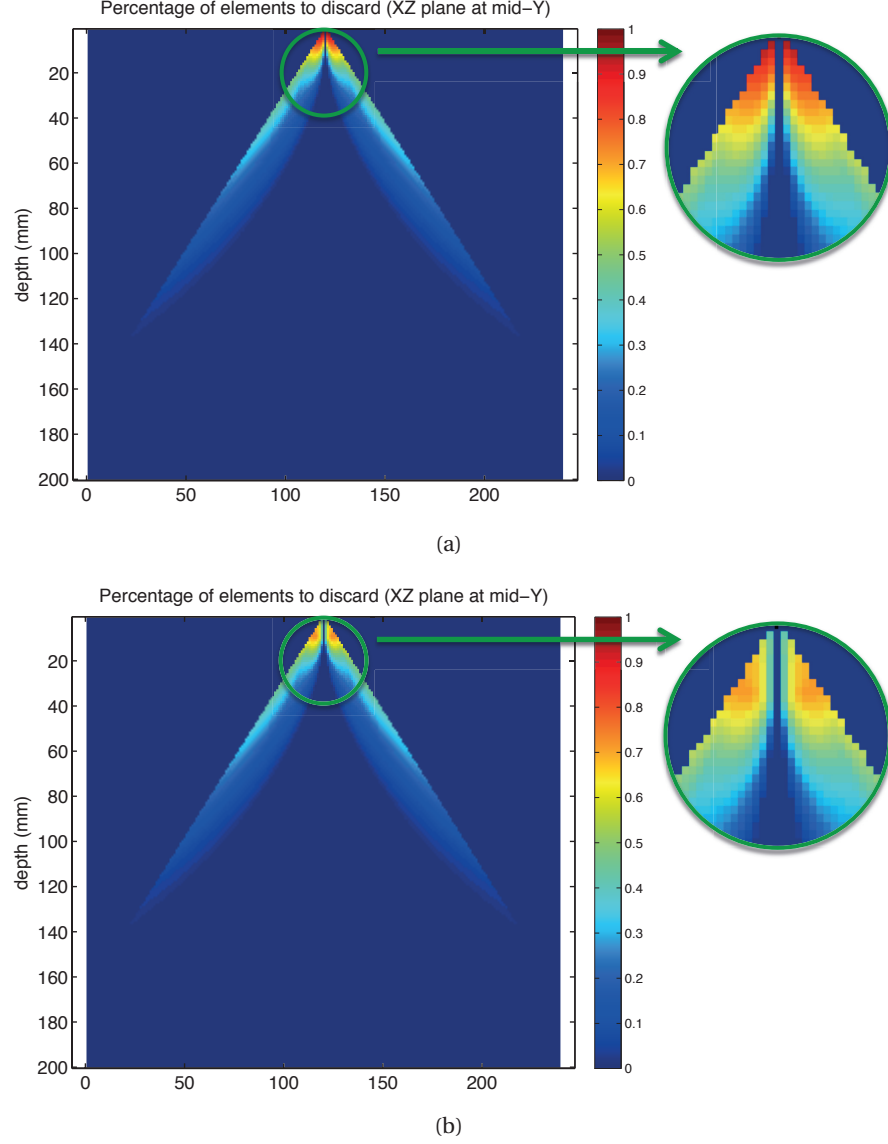


Figure 4.4: Graphical depiction of the geometric approximation in SHEDA approach. (a) Geometric inaccuracy of the approach. The inaccuracy is significant only very close to the probe and at broad angles. (b) Geometric inaccuracy after applying dynamic apodization (Section 5.1). The color map represents the percentage (0 = 0% and 1 = 100%) of elements that incur delay inaccuracy of more than the constructive interference threshold of 2 samples.

A first mitigation factor however comes in the form of apodization; since the worst inaccuracies

²Based on a phase offset threshold of 90° between constructive and destructive interference, and considering that the sampling frequency is $f_s = 8f_c$.

occur at broad angles beyond the elements' directivity, they are anyway discarded by the imaging system. Indeed, the typical expanding-aperture apodization function described in Section 5.1 weighs the probe elements whose directivity function makes them insensitive to given echoes by zero. Furthermore, the approximation's worst errors occur only at extremely short distances from the origin and at the extreme angles of the FOV (Figure 4.4(a)); both regions are usually the least critical for diagnosis. With a comprehensive numerical exploration in the volume of interest, considering the expanding apodization, we observed a reduction in both average and maximum absolute error. The average absolute error over the whole volume due to the algorithm itself becomes 44.641 ns , i.e. ≈ 1.4285 signal samples, while the maximum error equals $3.1\mu\text{s}$, i.e. 99 signal samples. Figure 4.4(b) shows the FOV inaccuracy map for a reconstruction based on SHEDA algorithm along with the typical expanding-aperture apodization function. We have further investigated and accordingly developed in Section 5.1.1 a stricter apodization scheme to trim away more of the elements yielding the remaining regions of inaccuracy of Figure 4.4(b).

4.4.2 Point Spread Function (PSF) Evaluation

We have assessed the approximation of the SHEDA delay calculation approach compared to the exact calculation by reconstructing point scatterers at different locations in the volume. We have plotted both the PSF contours, and the projections of those scatterers to evaluate the accuracy, the resolution, and the width of both the main and sidelobes of the proposed SHEDA approach. Five scatterer locations (Figure 4.5) have been chosen; a scatterer S_1 close to the probe surface and at the center of the imaging sector (Figure 4.6(a) and 4.6(f)), or very off-axis like S_2 (Figure 4.6(b) and 4.6(g)), a scatterer S_3 far from the probe surface and at the center of the FOV (Figure 4.6(c) and 4.6(h)), or at a broad azimuth angle like S_4 (Figure 4.6(d) and 4.6(i)), and finally a scatterer S_5 at an intermediate depth and at broad azimuth and elevation angles (Figure 4.6(e) and 4.6(j)). For S_1 , SHEDA exhibits even better resolution than the reference imager which uses square roots (Figure 4.6(f) and 4.6(a)). This counter-intuitive outcome can be explained by observing the unpredictability of delay inaccuracy artifacts. Along the central line-of-sight, where no steering occurs and the delay values are accurate, the reconstructed image is identical to the reference (central slice of Figures 4.6(f) and 4.6(a)). Away from this line (either side of 4.6(f) and 4.6(a)), the inaccuracy affects the reconstruction, yielding unpredictably slightly brighter or slightly darker voxels than the reference, which either slightly degrades or slightly improves the contrast and delineation of the feature in the central line. In this specific case, the latter phenomenon is occurring. Nonetheless, for most voxels in the volume, we tend to logically expect a degradation instead. For scatterers at the same depth and at broad angle (like S_2 in Figure 4.5), which is the most critical delay calculation inaccuracy region, SHEDA incurs a high calculation inaccuracy. Figure 4.6(g) shows that the PSF projection has a wide main lobe which more slowly degrades to the noise floor compared to the exact calculation. On the other hand, at far depths, either at the center azimuth angle (and/or elevation angle) or at the image edges, the proposed SHEDA method yields almost a perfect match with the exact delay calculation in both PSF contours and

projection (Figure 4.6(c), 4.6(h), 4.6(d), and 4.6(i)). For intermediate depth scatterers at broad angles, the exact delay calculation out-performed slightly the SHEDA calculation. This can be seen through Figure 4.6(e) and 4.6(j), where the contours of the SHEDA are a little bit wider, and the PSF projection degrades more slowly to the noise ground level, although the main lobe has the same width as the one of the exact calculation.

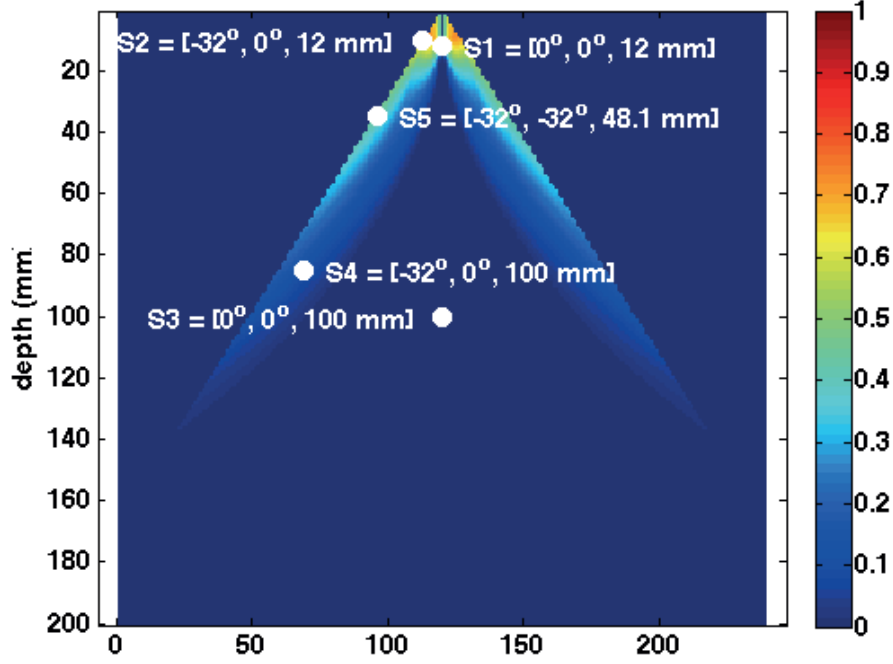


Figure 4.5: Locations of scatterers being reconstructed to test PSF contours and projections (Figure 4.6). The locations are overlaid on the inaccuracy map of Figure 4.4(b).

4.4.3 Fixed-Point Representation Inaccuracy

The second cause of inaccuracy is the fixed-point addition of the reference delay value with the two correction factors, and subsequent rounding to an integer index to access the data sample array. The inaccuracy due to using a fixed-point representation has a uniform distribution between $[-0.5, +0.5]$ *Least Significant Bit (LSB)*s. The final rounding of the summed value to an integer index of 10 bits incurs a further error of up to ± 0.5 samples.

4.4.4 Visual Assessment

A sample 2D image, reconstructed in Matlab with the SHEDA method, is shown in Figure 4.7(a). The source image data is a common example from the Field II [7] distribution. The image shown is a 2D reconstruction comprising 8 sub-images (zones), each derived from a different diverging-beam insonification. It can be seen that the subject is well-delineated. A comparison with the same image reconstructed with exact delay calculation i.e. non-optimized (Figure 4.7(b)) shows no degradation of the image quality with very negligible differences in

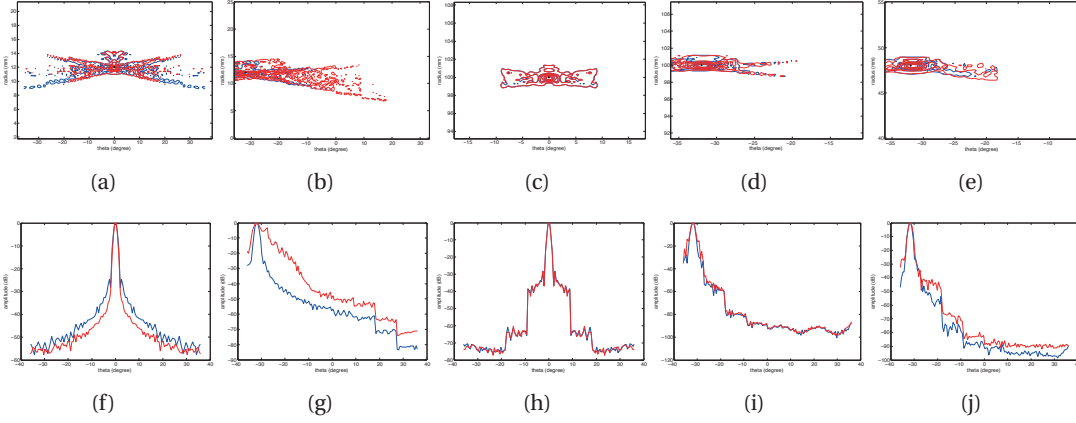


Figure 4.6: The evaluation for the SHEDA calculation approach based on simulating PSF contours and their projections for different scatterer location, where (a), (f) for a scatterer S_1 at $\theta = 0^\circ$, $\phi = 0^\circ$, $r = 12\text{mm}$, (b), and (g) for a scatterer S_2 at $\theta = -32^\circ$, $\phi = 0^\circ$, $r = 12\text{mm}$, (c) and (h) for a scatterer S_3 at $\theta = 0^\circ$, $\phi = 0^\circ$, $r = 100\text{mm}$, (d) and (i) for a scatterer S_4 at $\theta = -32^\circ$, $\phi = 0^\circ$, $r = 100\text{mm}$, (e) and (j) for a scatterer S_5 at $\theta = -32^\circ$, $\phi = -32^\circ$, $r = 48.1\text{mm}$. The blue curves represent the exact non-optimized delay calculation, while the red ones represent the SHEDA calculation.

speckle patterns close to the probe surface.

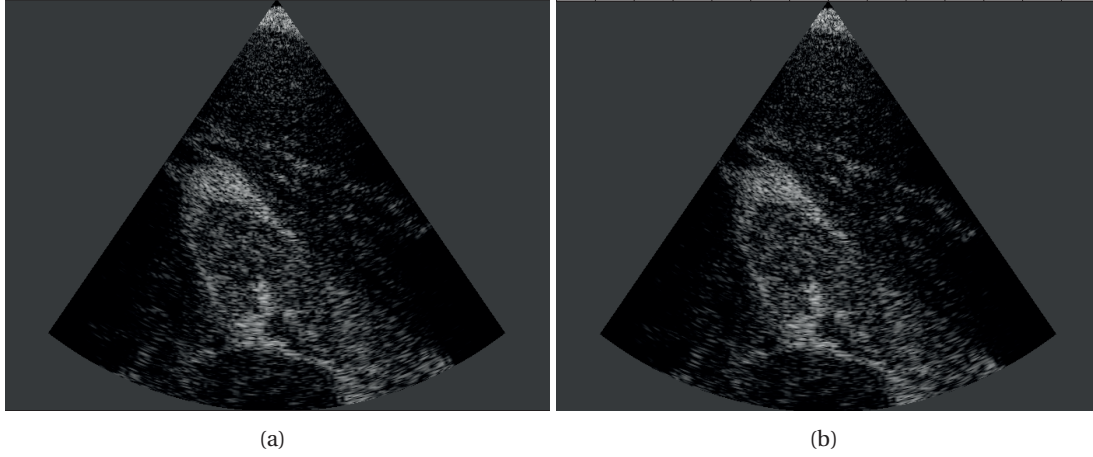


Figure 4.7: 2D imaging of a kidney phantom available online on the Field II website [7]. The reconstruction is composed of 8 zones, each insonified by different diverging-beam insonifications. The imaging depth is 10 cm and the azimuth sector is 73° wide. (a) SHEDA calculation method; (b) exact calculation method. On close inspection, the speckle pattern close to the transducer and at the edges of the imaging cone displays only minor differences.

4.5 Summary

In this chapter, one of the most demanding bottlenecks of the 3D processing pipeline has been tackled. It is the delay calculation unit. A novel efficient delay-calculation algorithm has been proposed that simplifies the massive number of intricate square-root calculations into just the calculation of a very few square-roots along the central line-of-sight while reconstructing the other lines-of-sights of the volume (or image) by adding two correction coefficients, which are pre-computed and stored in a small memory. The corresponding FPGA architecture has been presented in this chapter. We have also performed a detailed assessment of the inaccuracy of the proposed delay approximation algorithm.

5 Pre-Processing Optimization and Other Beamformer Logic

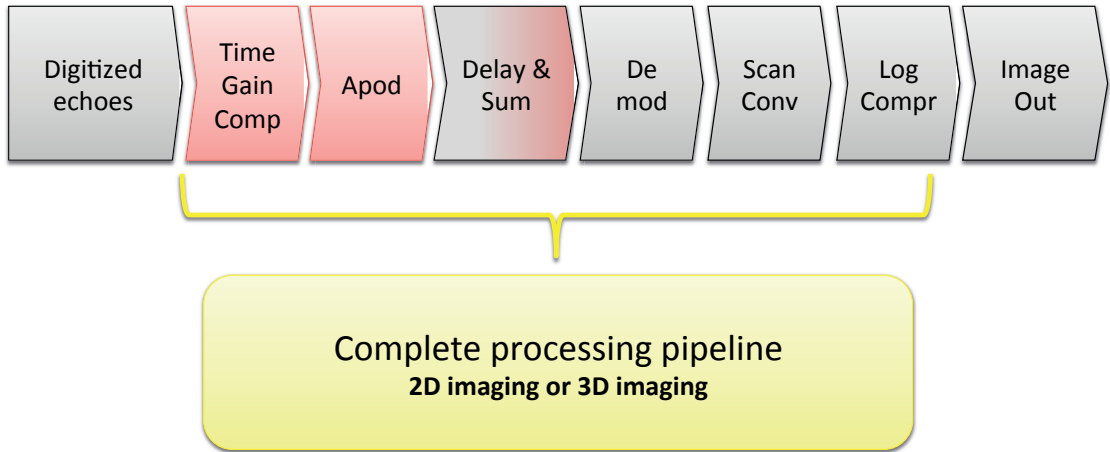


Figure 5.1: Logical processing flowchart of the US image reconstruction pipeline.

The received echoes in any US image processing system must undergo two essential scaling processes; apodization (w_{apod}) and TGC (w_{tgc}). Both apodization and TGC are weighting functions applied to the signals received by the US probe (Figure 5.1) to account for the side-lobes resulting from the antenna-like behavior of the transducer elements and the attenuation of the traveling US wave, respectively. They can be expressed through the weighting parameter $w(t, D)$ in (2.1) of the BF process, as follows:

$$w(t, D) = w_{apod}(t, D)w_{tgc}(t), \forall D \in 1, \dots, N. \quad (5.1)$$

Two proposed apodization schemes are discussed in this chapter; one is to compensate for the SHEDA delay approximation error reported in Section 5.1.1, and the other describes the final optimized apodization function implemented on our FPGA in the context of a single-board imager target (Section 5.1.2). In addition, the hardware realization of the TGC function is clarified in Section 5.2. This is followed by a dissection for the efficient processing order employed by our BF unit (TGC, apodization, and delay-and-sum) and the optimized input raw-data mapping to memory primitives, which both aim to save memory accesses and resources, especially in the 3D design (Section 5.3). Finally, the "sum" in the *delay-and-sum* algorithm including its hardware implementation, and our beamformer processing flow from the receive of the raw data until outputting a FP are explained in Section 5.4.

5.1 Apodization

The kernel of US BF includes apodization. Apodization is a well-known signal processing step used in multiple fields, for example in the design of electromagnetic antennas, where it helps shaping radio beams. Similarly, apodization in US improves the imaging quality by reducing the amplitude of the sidelobes in the receive directivity [41] - resulting from the antenna-like behavior of the element array - and thus improving the cleanliness and contrast of the image. Different techniques [133–135] and windowing functions [41] have been assessed for apodization w_{apod} with the aim of finding the balance between the suppression of the sidelobe contributions while maintaining the width and the height of the main lobe (i.e. preserving the useful information) which impact the resolution. Typically, a Hanning weighting window [42] is used and applied to the echoes received by the piezoelectric elements D of the transducer. As typical US systems focus dynamically on the voxels of the volume, calculating the corresponding delay profiles on-the-fly as discussed in Chapter 4, the apodization function must be, in principle, tuned differently for each such point. This problem is very hard to solve analytically, and more so to solve in a computationally-efficient way, although attempts have been made for 2D imaging [42, 136, 137]. Drastic simplifications have been adopted in the few papers discussing apodization for 3D US [110].

Commonly, the apodization window is implemented to have an aperture that is a function of the imaging depth (as indicated by time t), called “dynamic” or “expanding-aperture” apodization [42] (Figure 5.2). While reducing the sidelobes, the apodization plays another role in our system. It additionally reduces the regions of delay calculation inaccuracy by excluding - or reducing the considered - data received by some of the most inaccurate scatterer-element pairs, as discussed in Section 4.4.1 and Figure 4.4.

Based on that observation, we worked - in Section 5.1.1 - on proposing a new apodization scheme to minimize the delay inaccuracy in the FOV regions in which it is highest while performing the basic functionality of apodization, which is the reduction of the sidelobes. Then, in Section 5.1.2, we dissect the final scheme we proposed and chose to implement on board; *static apodization*, validated by the reasons that led to that choice.

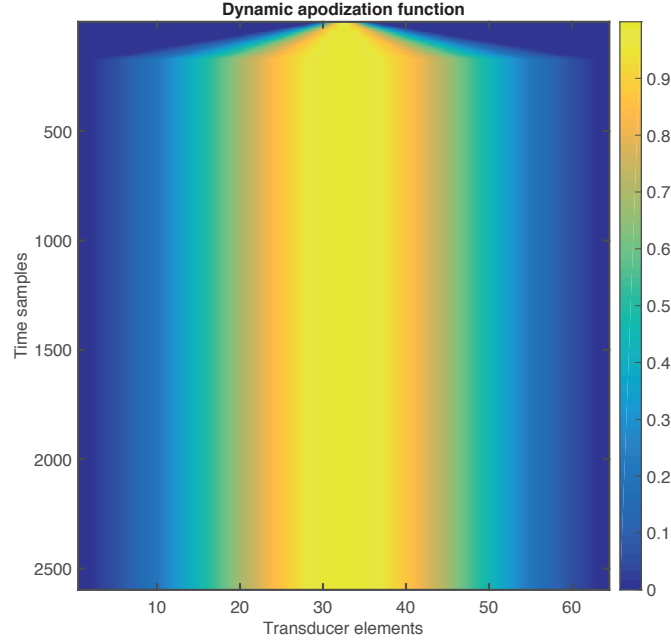


Figure 5.2: The "dynamic" apodization function plot (i.e. "expanding-aperture" apodization in radial direction). The color coding represents the apodization weighting. The transducer is at the top of the figures. For simplicity and easy visualization, we have plotted the apodization functions for the 64-element probe of the 2D imaging design. The apodization weighting is modeled as a Hanning function.

5.1.1 SCA - SHEDA-Correction Apodization Scheme

As shown in Section 4.4.1, the SHEDA approach, even when considering the effect of the typical dynamic apodization, remains still inaccurate in some regions (Figure 4.4(b)). For some locations S close to the probe surface and at broad angles, it introduces delay calculation errors of up to around $3 \mu s$. As the delay values are used to select a sample of the received echoes, this error equates to picking echo signals almost 100 samples off, and can essentially be characterized as a noise increase. A way to reduce this effect is to apply a stricter apodization window than the typical dynamic one. In other words, we propose, at those locations S , to prune the element contributions most impacted by the delay calculation inaccuracy (Figure 4.4(b)). By discarding about 18% of the received echoes on top of those discarded by dynamic apodization (Figure 4.4(b)), it is possible to reduce the delay calculation error to very low figures, typical of fixed-point designs that include rounding to an integer index for accessing the data sample array (maximum absolute error = 2.6749 delay samples, average = 0.6320). The discarding process is ruled by the observation that echoes that incur a delay calculation error of more than 2 samples¹ are the result of destructive interference rather than constructive one, and should accordingly be pruned. This result left an open question on how to discard the echoes that incur such delay inaccuracies, i.e. on how to identify a stricter

¹Based on a phase offset threshold of 90° between constructive and destructive interference, and considering that the sampling frequency is $f_s = 8f_c$.

apodization model.

We have proposed a custom apodization function, named *SHEDA-Correction Apodization* (SCA) scheme, that masks most of the inaccuracies of our approximate architecture for delay computation. To the best of our knowledge, the requirements and implementation of this function are unique and novel.

We have applied the concept of expanding apodization in such a way that it compensates for delay inaccuracy by discarding certain echoes, but at the same time keeping its implementation as simple as possible with an FPGA target in mind. This study runs following the same design settings used for the quality evaluation of the SHEDA algorithm (Section 4.4) ; i.e. 100×100 elements probe, sampling frequency of 32MHz, imaging volume of $73^\circ \times 73^\circ \times 500\lambda$, and $128 \times 128 \times 1000$ FPs BF resolution, and for the same reasons specified before. We do so by way of the following:

1. We examine the volume and derive, for each voxel, maps of (i) the usual expanding apodization window (Figure 5.3, white rectangle), and (ii) the set of elements that incur too large delay inaccuracies (Figure 5.3, region outside of the magenta contour).
2. We manually observe several of these maps, measuring the size of a new rectangular apodization window, subset of the base one, that discards as many “inaccurate” elements as possible while keeping as many of the “accurate” as possible (Figure 5.3, black rectangle).
3. We build by regression an initial set of equations that define the apodization windows (height, width, center abscissa, center ordinate) for varying locations S in the volume. This yields four equations as a function of r_S, θ_S, ϕ_S .
4. We run a script that exhaustively analyzes the volume to assess the impact of the model. This helps driving refinements of these equations, in order to trim or expand the apodization windows to achieve better results.

It is worth noting that this is an exercise in trade-offs, for several reasons. First of all, the apodization windows should ideally be unique for every S , but this is completely impractical - storing 16 million apodization windows (given a volume of $128 \times 128 \times 1000$ FPs), each defined over 100 by 100 elements, requires too much storage. It is similarly impractical to construct these windows in realtime, as they usually require computing a complex expression (e.g., a 2D Hanning) at an extremely fast rate. Therefore, a limited set of apodization windows should be precomputed and reused.

Additionally, the profile of the geometric inaccuracy (Figure 5.3) is such that to precisely discard the “inaccurate” elements and only those, a complex geometric pattern should be defined, and an even more complex smoothly degrading function on top. To simplify the implementation, we choose to only work with 2D Hanning functions defined on rectangles;

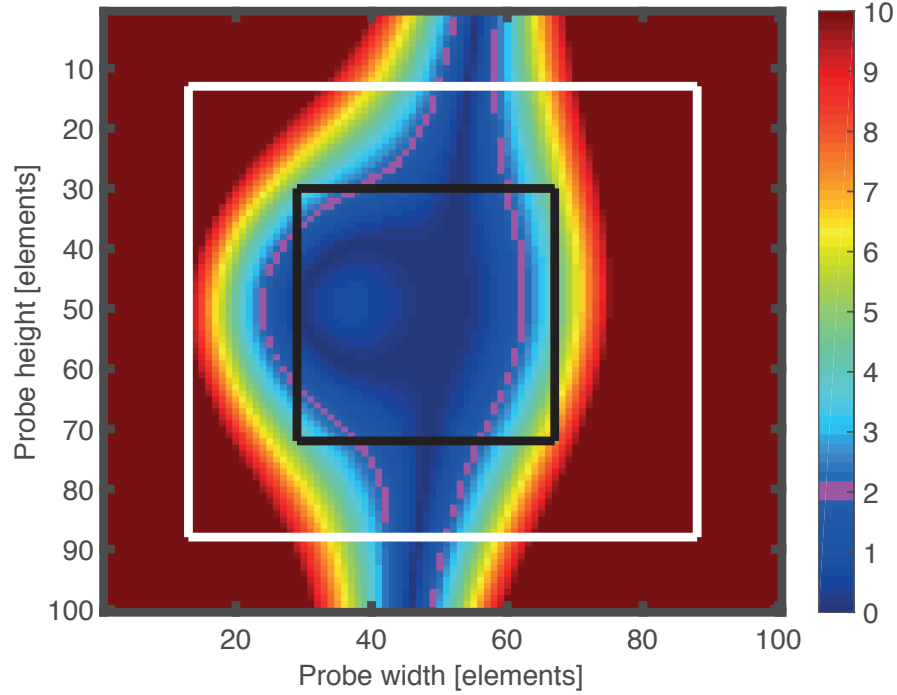


Figure 5.3: Inaccuracy of the delay calculation towards each element of the probe; the chart represents the probe face, and the color shade describes the calculation inaccuracy at that element D expressed in sampling periods, from a voxel S at $(r = 8\text{mm}, \theta = -28^\circ, \phi = -3^\circ)$. Blue = error of less than 1 delay sample, red = error of 8 samples. The contour line (magenta) defines the profile of the elements incurring an inaccuracy of ≤ 2 samples, i.e. the split between constructive and destructive contribution. White rectangle: standard expanding apodization window; black rectangle: apodization window derived in this work. Note how the latter window tracks more closely the 2-sample contour.

we must then trim profiles such as that of Figure 5.3 to a rectangle. This unavoidably either rejects a few usable elements or accepts a few “inaccurate” ones, which requires a balance.

After multiple refinements, we derived equations modeling the SCA window for the whole volume (Appendix B). Equations (5.2), (5.3), (5.4), and (5.5) are a sample of that model. They describe the width, the height, and the center - x_c and y_c - of the apodization window for a single zone of the volume. As can be seen, the width and the height are expressed as a function of r, θ, ϕ , while x_c is expressed as a function of r, θ , and y_c is expressed as a function of r, ϕ . The angle variables are expressed in degrees and the r variable is expressed in periods of the sampling frequency. Equations (5.2), (5.3), (5.4), and (5.5) hold in one region of the volume and are replicated symmetrically in θ and ϕ . As the size and the location of this window fluctuate in very complex ways, we have chosen to use different equations to model them in different sections of the volume, although the modeling cannot be perfect. These windows are a smaller version of the usual expanding apodization windows, and thus completely replace them e.g. for the purpose of omitting elements that should be excluded due to limited directivity.

Appendix B shows the complete set of the derived equations modeling the SCA apodization.

$$W(r, \phi, \theta) = \frac{13r}{140} - \frac{\theta + 37}{3.5} - \frac{\phi + 37}{3.5} + 19, \quad (140 \leq r < 1500) \wedge (-36^\circ \leq \theta \leq -19^\circ) \wedge (-18^\circ \leq \phi \leq 0^\circ) \quad (5.2)$$

$$H(r, \phi, \theta) = \frac{13r}{140} + \frac{\theta + 37}{3.5} + \frac{\phi + 37}{3.5}, \quad (140 \leq r < 1500) \wedge (-36^\circ \leq \theta \leq -19^\circ) \wedge (-18^\circ \leq \phi \leq 0^\circ) \quad (5.3)$$

$$x_c(r, \theta) = 49 - \frac{3r}{420} + \frac{\theta + 37}{10.5}, \quad (140 \leq r < 1500) \wedge (-36^\circ \leq \theta \leq -4^\circ) \quad (5.4)$$

$$y_c(r, \phi) = \begin{cases} 51, & ((140 \leq r < 1500) \wedge (-3^\circ \leq \phi \leq 0^\circ)) \\ 49 - \frac{3r}{420} + \frac{\phi + 37}{10.5}, & (140 \leq r < 1500) \wedge (-36^\circ \leq \phi \leq -4^\circ) \end{cases} \quad (5.5)$$

The SCA windows defined by these equations enable a large improvement in the rejection of elements that are subject to high inaccuracy of delay calculation, as can be concluded from Table 5.1. This can also be seen graphically in Figure 5.4 compared to both Figure 4.4(a) and 4.4(b). We could achieve a reduction from 15.4% to 3.5% (-77%) of the elements subject to large delay inaccuracy, while sacrificing only around 27% of the accurate echoes. The memory requirement is 5.8 MB while accounting for the large number of permutations in window sizes, and considering coefficients' representation at a precision of 16 bits.

Table 5.1: Count of elements that are apodized away by different apodization functions; for the remaining elements, count of the elements that experience accurate or inaccurate delay calculation (threshold = 2 sampling periods of inaccuracy). Memory buffer size required to store the corresponding apodization functions, e.g. 2D Hanning functions, considering a precision of 16-bit representation.

	Elements Apodized Away	Elements Kept (Accurate Delay)	Elements Kept (Inaccurate Delay)	Memory
Expanding Apodization	3.2%	81.4%	15.4%	327 kB
SCA	37.4%	59.1%	3.5%	5.8 MB
SCA, square	37.5%	59%	3.6%	2.06 MB

Next, we also evaluated the opportunity of defining the apodization windows as square, in order to save memory. This reduces the set of equations required to only three, one for both width and height, and two for the centering. The outcomes in terms of precision and memory requirements are also shown in Table 5.1. We discovered that in return for a negligible loss in rejection, it was possible to dramatically decrease the required amount of memory storage

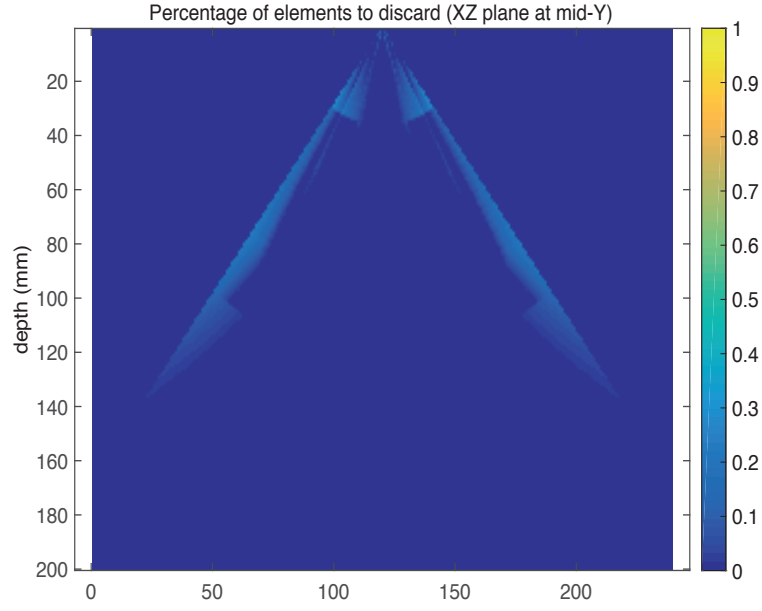


Figure 5.4: The inaccuracy in delay calculation becomes negligible by discarding all the echoes from elements that incur more than 2 samples of calculation inaccuracy. The plot shows, for each voxel S on the XZ plane of the image, the percentage (0 = 0% and 1 = 100%) of such elements when using the proposed tighter apodization. The color bar A significant inaccuracy reduction can be noticed compared to Figure 4.4(a) and 4.4(b).

(almost 3 times less).

The impact of the SCA scheme on the reconstruction quality has been evaluated using the PSF metric. The PSF allows the evaluation of the apodization scheme in terms of the reconstruction localization accuracy, the resolution, and the width of both the main and sidelobes. Figure 5.5 and 5.6 show the PSF contours and their projections for two scatterers located at the most critical regions; one is at $\theta = -17$, $\phi = -3$, $r = 12\text{mm}$ and the other is at $\theta = -20$, $\phi = 0$, $r = 15\text{mm}$, respectively. For each scatterer, we compare the PSF contours and projections that are based on SCA scheme and SHEDA algorithm (Figure 5.5(c), 5.5(f), 5.6(c), and 5.6(f)) with the PSF contours and projections of the typical dynamic apodization while using either exact delay calculation (Figure 5.5(a), 5.5(d), 5.6(a), and 5.6(d)) - the golden reference - or SHEDA algorithm (Figure 5.5(b), 5.5(e), 5.6(b), and 5.6(e)). Figure 5.5 shows that the usage of the SCA on top of the delay approximation algorithm (i.e. SHEDA) over-performs the dynamic apodization in combination with the same SHEDA approach. In particular, the peaks in Figures 5.5(f) and 5.6(f) show that the SCA achieves more accurate localization for the scatterer than when using the typical dynamic one (Figure 5.5(e) and 5.6(e)). In addition, Figure 5.5 shows that the SHEDA delay algorithm - while using either expanding apodization or SCA - yields much lower sidelobes compared to the exact delay calculation. However, this is an observation related to the delay calculation algorithm rather than the apodization scheme (Section 4.4.2). The main lobe of Figures 5.5(f) and 5.6(f) is a bit narrower than in Figure 5.5(e) and 5.6(e). The sidelobes on the other hand are a bit higher.

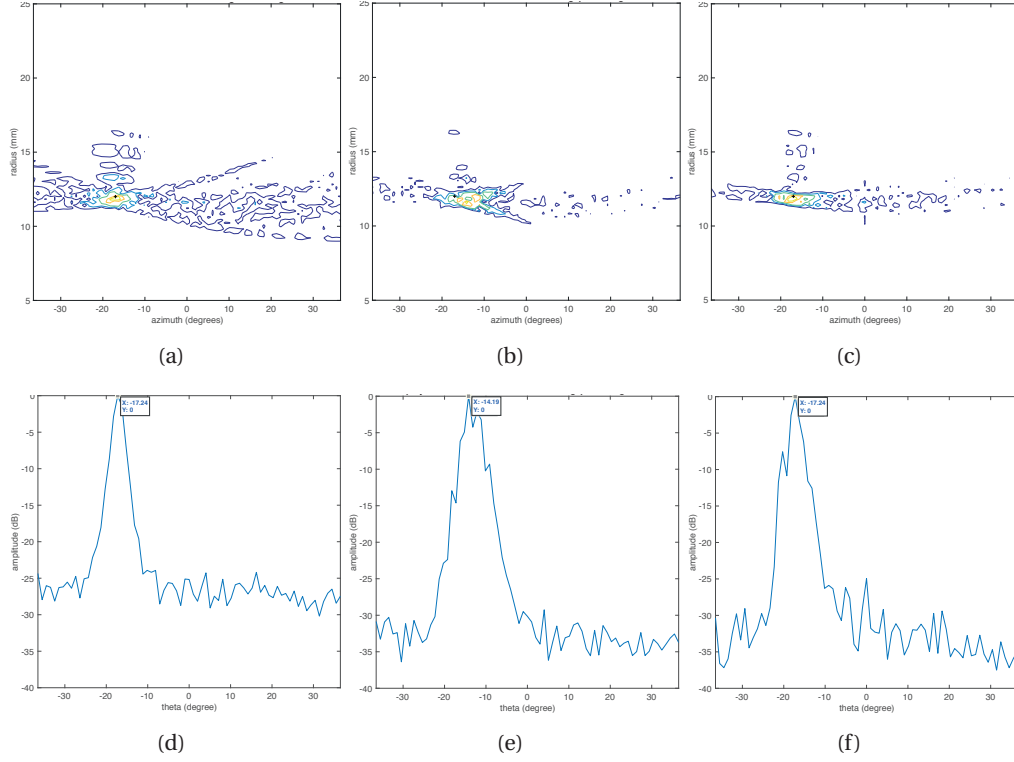


Figure 5.5: Evaluation of our SCA scheme versus dynamic apodization in terms of PSF contours and projections for a scatterer at $\theta = -17^\circ$, $\phi = -3^\circ$, $r = 12$ mm. This is achieved by testing the reconstruction that is based on : (a) and (d) exact delay calculation while using expanding apodization (golden reference), (b) and (e) SHEDA delay calculation while using also expanding apodization, and (c) and (f) SHEDA delay calculation while using the SCA model. The PSF contour colors represent the level in dB, in a range of -5 dB, -10 dB, -20 dB, -30 dB, -40 dB from inside to outside.

Moreover, we have performed visual assessment for the scheme by reconstructing a phantom and evaluating visually the final output (Figure 5.7). Although the numerical and the PSF evaluation of the SCA scheme show fair filtering for the inaccuracies, the final image reconstruction and its visual assessment do not indicate significant improvement in the quality. We do not yet have a qualitative explanation for this result, but we advance the following hypotheses:

1. The elements that incur inaccuracies higher than the threshold (2 samples) could be *in aggregate* contributing constructively by useful information.
2. The unavoidable removal of some accurate elements may be a strong factor of quality loss offsetting the quality gain - by the omission of the inaccurate elements - in the final image.
3. The inaccuracy introduced by the SHEDA approximation approach could be minor enough to not change the image features (such as suppressing a tumor or false positive

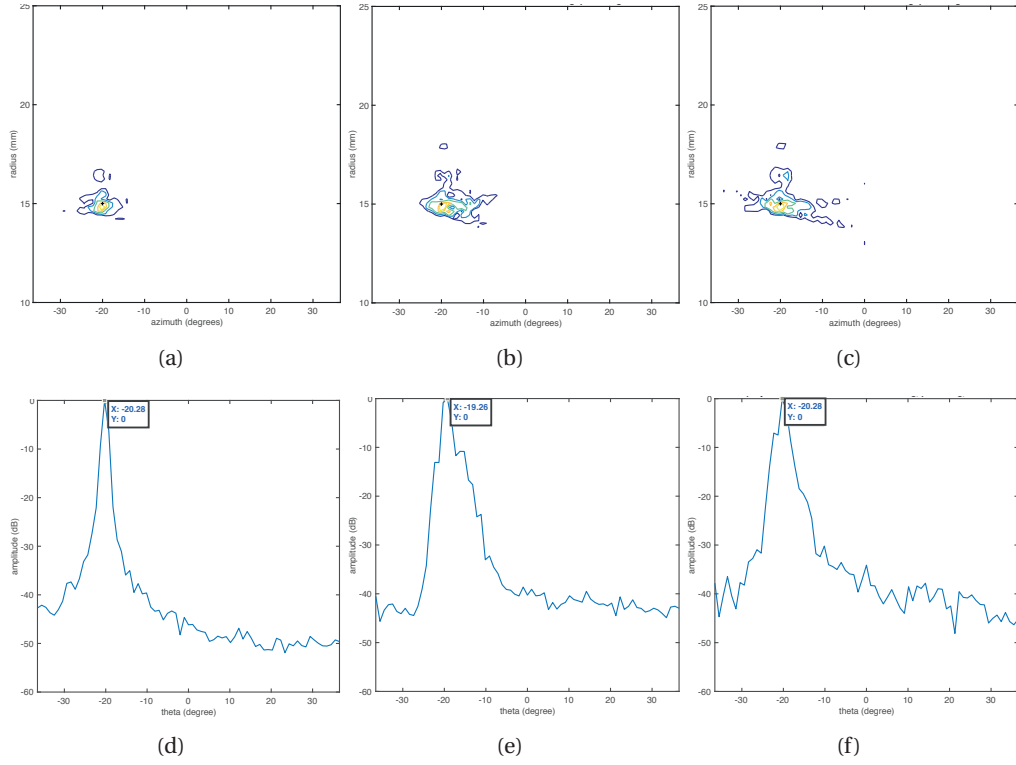


Figure 5.6: Evaluation of our SCA scheme versus dynamic apodization in terms of PSF contours and projections for a scatterer at $\theta = -20^\circ$, $\phi = 0^\circ$, $r = 15$ mm. This is achieved by testing the reconstruction that is based on : (a) and (d) exact delay calculation while using expanding apodization (golden reference), (b) and (e) SHEDA delay calculation while using also expanding apodization, and (c) and (f) SHEDA delay calculation while using the SCA model. The PSF contour colors represent the level in dB, in a range of -5 dB, -10 dB, -20 dB, -30 dB, -40 dB from inside to outside.

indication of a lesion), but only introduces little difference in the speckle distribution - in the inaccurate regions - compared to a perfectly reconstructed image. This minor difference can even be perceived as a result of performing the reconstruction based on different imaging algorithm rather than inaccuracy introduction by approximation method.

These interpretations will need to be tested against different probe settings, imaging specifications, geometries, and phantoms in order to confirm or contradict any of the mentioned points. In addition, the apodization modeling process needs to be more automated, allowing easy iteration and convergence for any given imaging settings. Keeping our main aim - of the first telesonography-capable complete 3D US system - in mind and the available time to achieve that target, we have frozen the research in that direction. This decision has been supported by the positive results of the SHEDA algorithm quality evaluation in Section 4.4.2, and based on the fact that the inaccuracies introduced by the approach are anyway in uncritical regions for

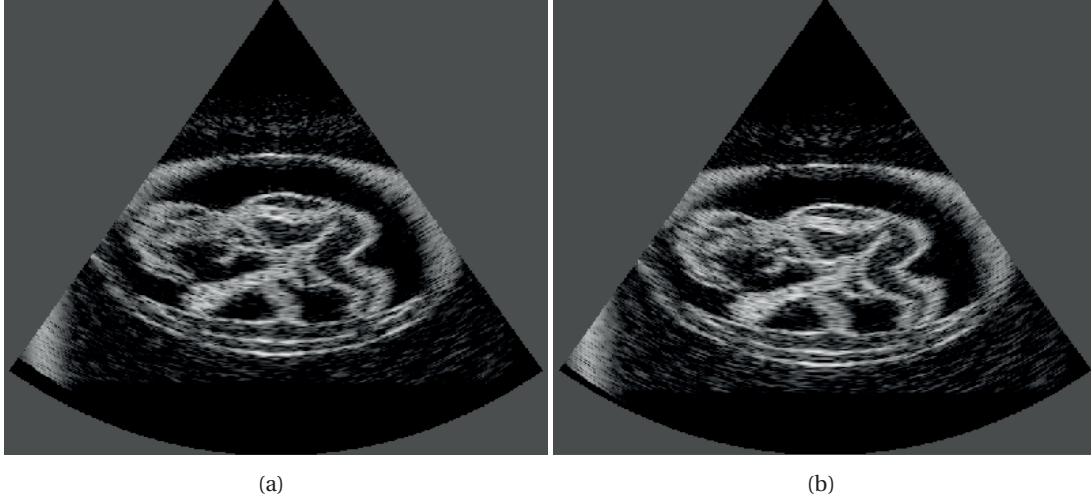


Figure 5.7: 3D imaging of a fetus phantom provided online while [8] using (a) expanding apodization, or (b) SCA *square* model.

diagnosis. However, we think that SCA is also a topic ready for further investigation.

5.1.2 Static Apodization Scheme

Considering our objective of fitting a 3D digital US imager in a single board, we returned back to study the typical expanding apodization $w_{apod}(t, D)$ [42] and its implementation. We found that at a shallow depth - which is 0.7 cm and 0.32 cm according to our 2D and 3D designs' settings (Table 1.1), respectively - the optimal window width already reaches the whole transducer's width as depicted in Figure 5.2. Thereafter, it converges to a static function of only D , $w_{apod}(D)$. In order to reduce the resources utilized by our imager, and since the difference between static and dynamic apodization is only in the very shallow area that overlaps with the region already affected by delay inaccuracy and which usually has low diagnostic relevance, we chose to fall back on a simpler scheme and finally implement a fully *static Hanning apodization* (Figure 5.8) in our imager. The static apodization coefficients, one per transducer element (i.e. 64 in 2D and 1024 in 3D), can be pre-calculated and stored in a small table with 16-bit representation. The table total size is 128 B in 2D and 2 kB in 3D. Even for the same probe settings specified in Section 5.1.1 (i.e. 10,000-element probe), the required memory size would be 19.5 KB, which is much less than the utilization of any scheme mentioned in Table 5.1. In addition, static apodization avoids the addressing logic needed to apply any of the schemes mentioned in Table 5.1. Static apodization coefficients fit in a single Xilinx BRAM, the size of which is 1024 rows of 18-bits. In order to apply the apodization coefficients to the RF data on the fly, a number of DSP multipliers matching the input sample rate must be deployed. When the Ethernet input (Section 7.2) is used, this means 2 samples/clock cycle, while with Aurora (Section 7.1) it is possible to receive up to 6 samples/clock cycle. Therefore, a small number of DSP multipliers is sufficient. This reduces

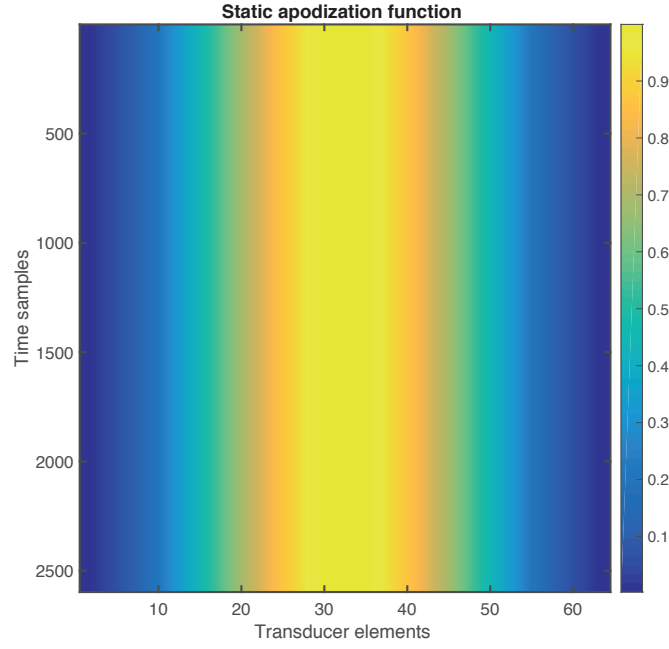


Figure 5.8: The static apodization function plot (the one implemented on our single FPGA) versus the radial-dynamic one depicted in Figure 5.2. The color coding represents the apodization weighting. The transducer is at the top of the figures. For simplicity and easy visualization, we have plotted the apodization functions for the 64-element probe of the 2D imaging design. The apodization weighting is modeled as a Hanning function.

implementation cost greatly (Challenge 3 - Section 1.3.3 and Challenge 4 - Section 1.3.4) while affecting the image quality slightly and only in the very shallowest region of the image.

5.2 Time-Gain Compensation

Another weighting function must be applied to the US echoes. The acoustic wave incurs propagation attenuation that increases as the wave propagates further. Therefore, the received echo amplitude should be compensated against that attenuation by applying a gain function in the traveling time (i.e. traveling depth), called *Time-Gain Compensation (TGC)*. As mentioned in Section 2.2, TGC can be performed in the analog front-end (i.e. the transducer head), but also in the digital back-end processing unit, as we implemented ($w_{tgc}(t)$). Equation 5.6 clarifies the calculation of our TGC coefficients.

$$w_{tgc}(t) = 0.5 \times 10^{\left(\frac{atten_dB_cm}{20} \times 2 \times d_t \times 100\right)}. \quad (5.6)$$

$atten_dB_cm$ is the attenuation coefficient which is assumed 1 dB/cm, and $2 \times d_t$ represents the traveling depth of the echoes sampled at time t . The division by 2 in the w_{tgc}

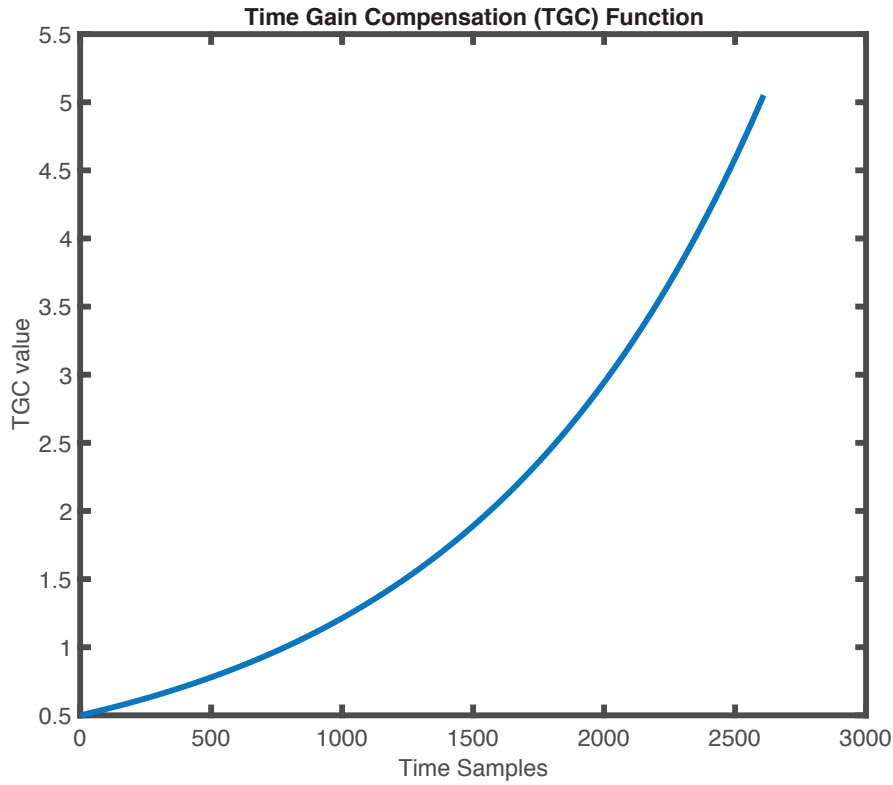


Figure 5.9: TGC function plot (linear scale) for different time samples (i.e. imaging depth). It is an exponential growth representing the relation between the compensation of the signal versus the traveling time (or depth).

calculation is just to have an extra bit of dynamic range on the FPGA so that we don't risk over-saturating some echoes (e.g. when they already approach the ADC's saturation limit and then the TGC amplifies them). That division does not affect the overall reconstruction quality since it is considered as a fixed scaling for the whole image brightness. Figure 5.9 plots the exponential growth function defining the TGC. In our design, the TGC coefficients are also pre-calculated and stored in a small table; a small number of DSP multipliers (same number as for apodization) has been used to apply these coefficients to the apodized RF data.

5.3 Beamformer Processing Order and Input-Memory Mapping

Both the apodization and TGC weightings (Section 5.1 and 5.2), and the delay-and-sum unit (Chapter 4 and Section 5.4) constitute our beamformer. Figure 5.11 draws an abstracted architecture diagram of our single-board design. All the blocks interact via the *Advanced Extensible Interface (AXI)* interconnect except the green blocks that represent the real-probe listening units (Section 7.1), which feed directly the received echoes to the beamformer. The orange blocks represent the beamformer. Figure 5.12 depicts the logical flowchart of the US processing pipeline shown in Figure 2.6; i.e. the functional flow of the main blocks in the

processing pipeline, but colored based on the color-map of Figure 5.11.

Typical US echoes are sampled with 12- to 16-bit ADCs. The weighted data - by both TGC and static apodization - can thus be stored onto 18-bit BRAMs in the FPGA (Figure 5.11), one sample per line. To minimize memory pressure (Challenge 1), in streaming fashion, only a sliding window of the echo samples is on-FPGA at any time; earlier samples are discarded as soon as possible to make space for later ones. To enable this, we resort to a *nappe-by-nappe* beamformer [92] (Figure 5.10). While traditional architectures reconstruct images one radial line at a time, this reconstruction sequence resembles successive onion layers. The key advantage is that each nappe is reconstructed from temporally thin contiguous inputs or *blankets*, which can be stored on-chip. Blanket thickness depends on geometric variables and varies with depth. Conveniently, geometric calculations reveal that the minimum required thickness of the sliding window is only a few hundred samples, which is easily affordable. We store the input samples onto Xilinx BRAM memory blocks, which can hold 1024 rows of 18 bits. In 3D, where BRAM count is a bottleneck, and since Xilinx Ultrascale BRAMs have dual-ported architecture (i.e. support a maximum of two concurrent reads), we can therefore pack samples from two receive channels into a single BRAM (i.e. 512 samples per channel simultaneously on-chip), needing a total of 512 BRAMs for 1024 channels. In 2D, we simplify the design and improve performance by dedicating one full BRAM (1024 samples) per receive channel, for a total of 64 BRAMs.

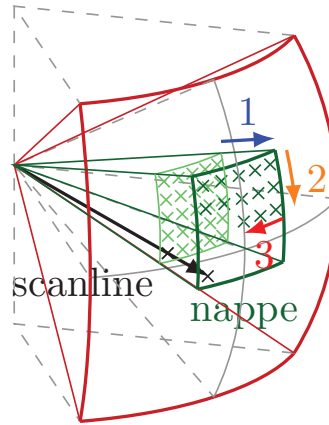


Figure 5.10: Focal point calculation order in a nappe-oriented beamformer: all points at a given depth are calculated; then the depth is incremented. A scanline is also shown for comparison; a scanline-oriented beamformer will reconstruct points along the whole scanline, then move to the next. The 1, 2, and 3 directions represent the radial (i.e. depth), elevation, and azimuth directions, respectively. Figure copied from [9]

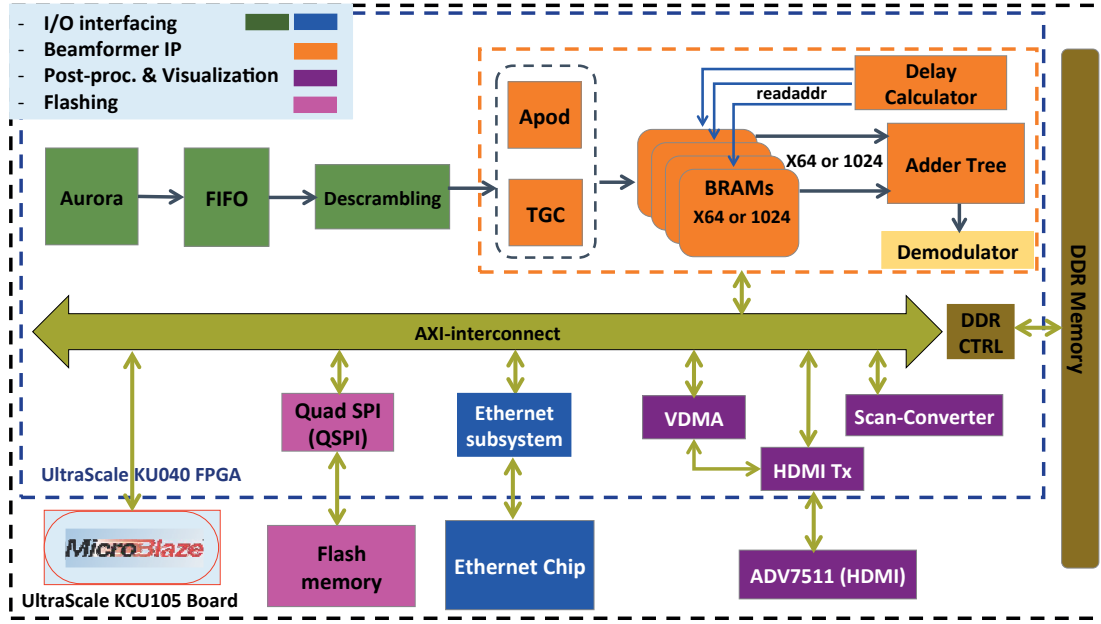


Figure 5.11: An abstracted architecture diagram of the proposed US Imager. The orange blocks represent the beamformer which comprises the TGC, the apodization, the BRAMs containing the input weighted samples, the delay calculator, and the adder tree units. The beamformer blocks are covered in both Chapter 4 and 5.

5.4 The Beamformer Summation

Figure 5.11 shows that the weighted (by TGC and apodization) samples are stored in BRAMs (Section 5.3), then fetched using indices representing the calculated delays (Chapter 4), then summed to output beamformed FPs. We have implemented this sum process as an adder tree of depth 6 for the 64-channel 2D system and 10 for the 1024-channel 3D system, utilizing 63 adders and 1023 adders, respectively. This implementation guarantees the full exploitation of the high parallelization of the delay calculator architecture, which accordingly maximizes the throughput of the beamformer. Our beamformer throughput is 1 FP per clock cycle (Section 7.7.2).

The beamformed FPs go then through the demodulation process (Section 6.1), and finally stored in an off-chip *Double Data Rate* (DDR) memory for further conditioning by the post-processing and visualization unit (Chapter 6).

5.5 Summary

In this chapter, the pre-processing stage of our single-FPGA digital 3D US imager has been exclusively handled. Both the apodization function, which is commonly considered as another core unit of the BF process - in addition to the delay calculation unit -, and the TGC scaling have been dissected. For the apodization, we have proposed two schemes: SCA and static

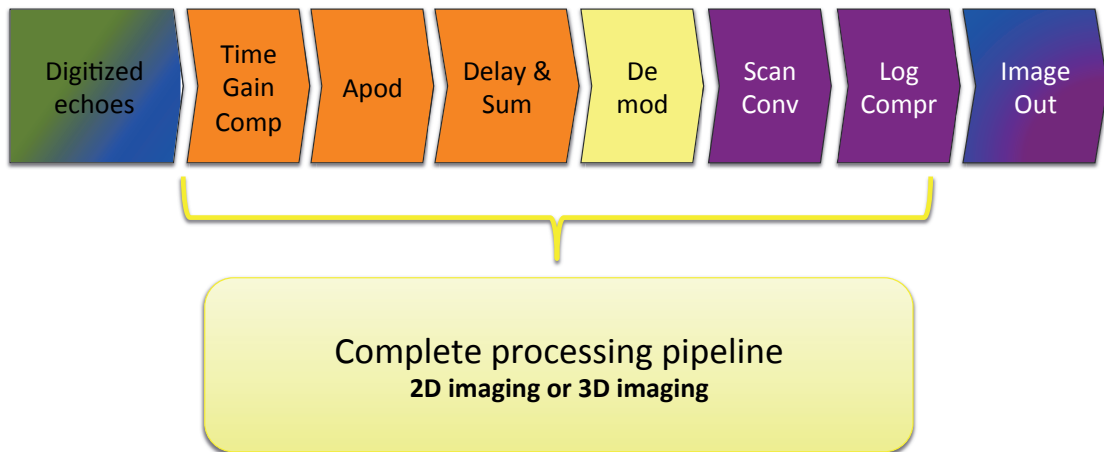


Figure 5.12: The logical processing flowchart of the US image reconstruction pipeline (like Figure 2.6) colored according to the color-map of Figure 5.11.

apodization. We have discussed their mathematical formulation, accuracy, and resource utilization. We chose the static apodization scheme to be implemented on our single-FPGA platform. We have validated and verified that choice in terms of both accuracy impact and resource utilization. The calculation of the TGC function and its hardware implementation details are also reported in this chapter. Moreover, we have explained the efficient processing order adopted by our beamformer and discussed the input data map of our design, with the aim of achieving as efficient memory consumption and accessing as possible. Finally, the realization of the sum stage in the *delay-and-sum* BF method has been clarified, and the block diagram of our beamformer including its composing processes has been depicted.

6 Post-Processing Optimization And Imaging Mode Support

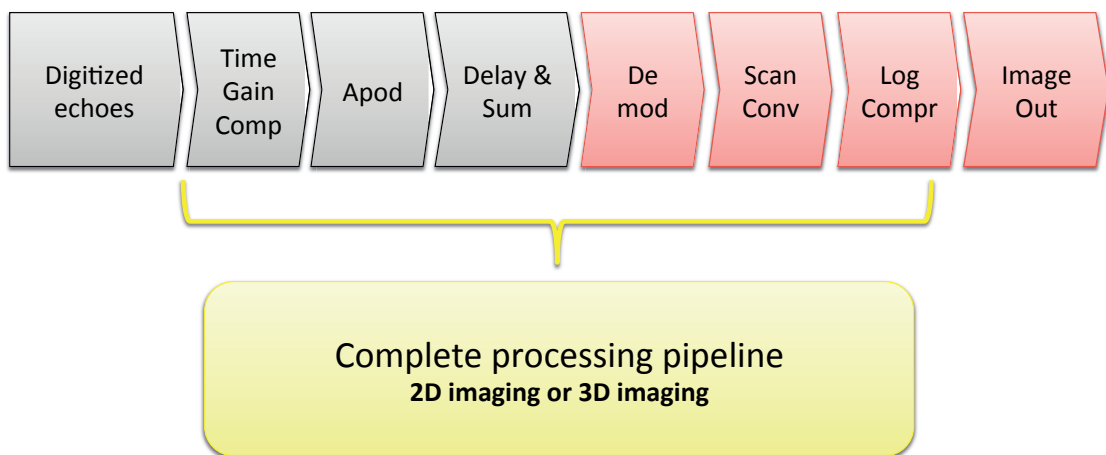


Figure 6.1: Logical processing flowchart of the US image reconstruction pipeline.

The US beamformed data (Chapter 4 and 5) have three features. They are still modulated by the US carrier signal, reconstructed in polar coordinates (cannot be directly shown on a screen), and span a huge dynamic range uninterpretable by human vision. Therefore, a US post-processing stage must include a demodulator, polar-to-Cartesian transformation, and logarithmic compression. In this chapter, all of these post-processing and visualization processes have been efficiently tackled to fit in our compact embodiment (Sections 6.1 and 6.2).

Our 1024-channel system, although compact, features three common US imaging modes: Single-Insonification Reconstruction Imaging (SIRI), zone imaging, and compound imaging, discussed in Section 6.3. The whole-system reconstruction quality for each of the supported

imaging modes has been extensively evaluated quantitatively and qualitatively using various metrics (Section 6.4).

6.1 Demodulation

After BF, the reconstructed image is still in the high-frequency domain with a frequency spectrum around the transducer's central frequency and needs demodulation, or in other words envelope detection. The demodulation provides a readable image by shifting the RF range back to the baseband frequency. Many techniques are available. In general, the signal envelope must be tracked by applying a signal transformation, followed by low-pass filtering. In our Matlab pipeline, we investigated various demodulation methods (Figure 3.1), like Hilbert and IQ-demodulation functions for signal transformation, and Butterworth and FIR low-pass filters. For our final portable hardware design, we chose a resource-friendly algorithm, performing demodulation as an absolute-value computation followed by a P -order FIR Low-Pass Filter (LPF). This minimizes not only the resource utilization but also the design complexity. The method still provides fair demodulation quality.

Figure 6.2 shows the block diagram of the chosen method implemented on the board. The figure also depicts how the envelope extraction is achieved by plotting an arbitrary signal representing the modulated input and the progression of that signal after each stage of the process. After each clock cycle, the absolute value of the beamformed FP is calculated and then stored in a circular buffer of depth $P + 1$ and width equal to a whole nappe. The FIR filter is applied along the lines-of-sight of the $P + 1$ buffered nappes. Finally, the demodulated FPs are then stored in another buffer until the completion of the whole volume (or image), to be then used by the visualization unit (Section 6.2) and later transmitted to a remote hospital for diagnosis. We assume a 4th-order filter, i.e. $P = 4$, and accordingly a buffer of 5 nappes deep, when evaluating image quality and resource utilization. In Figure 5.11, depicting our imager design architecture, the demodulation block is in yellow just after the adder tree.

6.2 Log-Compression, Cross-Sectional Scan-Conversion, and HDMI Support

The last processing step in our US imager pipeline is the visualization (Figure 6.1). This includes two main processes: *Log-Compression (LC)* and *Scan-Conversion (SC)*. The brightness of the US images just after the BF and demodulation has an extremely high dynamic range, which makes the images look to the human eye as either completely black or completely white. The LC operation, i.e. a logarithmic brightness manipulation, maps the image brightness from the original high dynamic range onto a logarithmic gray scale adapted to human vision. The resulting images feature appropriate contrast suiting visual interpretation and investigation.

Another key operation is necessary since, in most US imaging methods including 3D US,

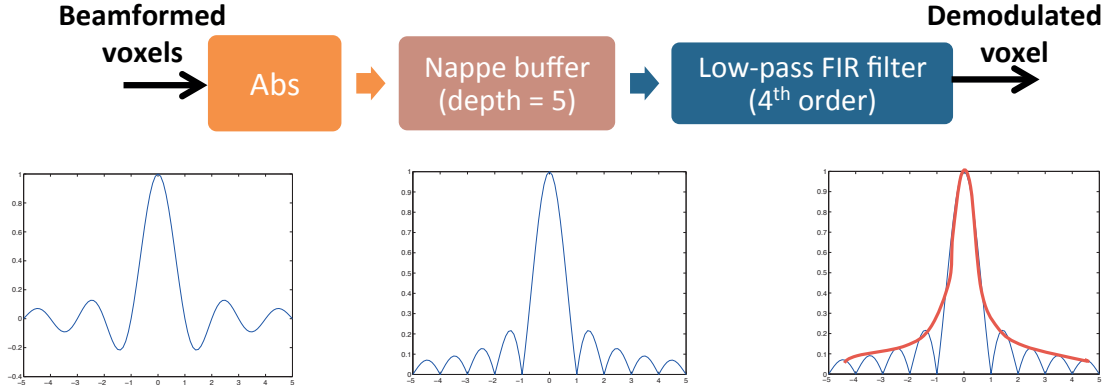


Figure 6.2: The block diagram of the simple demodulation method implemented on our single-FPGA imager. The method relies on calculating the absolute value of the beamformed voxels, then buffering them, and finally detecting the envelope by applying a LPF realized as an FIR filter.

the beamformed images are reconstructed in polar coordinates. SC transforms the image from the polar coordinate space into the Cartesian coordinate space, allowing the image to be displayable on a grid of pixels on a screen. This transformation can be performed using interpolation, which also allows image scaling.

The SC process for a whole volume (i.e. 3D reconstruction) is too computationally and materially expensive to fit in a single FPGA and run in realtime, as clarified and numerically proved in Challenge 5 - Section 1.3.5. Both the BF and the SC processes are considered major bottlenecks in the 3D US processing pipeline. However, recall that the cardinal goal of this work is to decouple image acquisition and diagnosis. This means that the full 3D SC can be performed remotely at the hospital, when needed; the local operator needs at most a 2D cross-sectional image display for guidance and on-site feedback, e.g. on a built-in device screen. Therefore, we implement a block that performs this much simpler operation. In the baseline case of 2D imaging, this block nevertheless does scan-convert the whole image.

The architecture of our SC block allows the operator to choose, using the developed *GUI* and the Ethernet communication with the board (Section 7.4), which cross-section of the volume is to be scan-converted and displayed. The default displayed cross-section by the system is the middle elevation slice (i.e. middle azimuth-depth plane) of the volume. For non-central slices, this process yields slightly distorted images. The architecture restricts the SC of oblique cuts. Other settings, like brightness and contrast control, are also configurable (Section 7.4). The IP block is equipped with a master AXI interface, which allows much faster operation than a software-driven block [138, 139] and achieves a SC rate of 14 *Frames Per Second (FPS)*.

Further, the proposed design supports HDMI output to a display. We have used the Analog Devices ADV7511 [140] part on our KCU105 board for transmitting the HDMI output. In Figure 5.11, an HDMI transmitter (HDMI TX) is used to interface the ADV7511 device with

the FPGA, while an *Video Direct Memory Access (VDMA)* IP is utilized to provide the high-bandwidth direct access memory for the frames stream. The interfacing between the VDMA on the FPGA and the ADV7511 is needed mainly to check the clock between the VDMA and the ADV7511, which varies depending on the resolution. The design also allows changing between different output resolutions from 640×480 to Full-HD 1920×1080 . Both the SC (including LC) unit, and the HDMI blocks are represented in purple in Figure 5.11. They interact with the DDR to store or retrieve data via the AXI interconnect.

6.3 Imaging Modes: SIRI, Zone Imaging, and Compound Imaging

Our single-board design supports three different US imaging modes: *SIRI* (Section 6.3.2), zone imaging (Section 6.3.2), and compound imaging (Section 6.3.3). They are considered among the essential modes in any US imaging system.

6.3.1 Single-Insonification Reconstruction Imaging (SIRI)

SIRI is the most basic imaging mode. In SIRI, the reconstruction of the whole ROI is performed based on a single insonification. This insonification must use a broad beam profile, such as a diverging or plane wave. In this thesis, we assume the use of a phased array transducer (i.e. small probe footprint), therefore the natural choice is a diverging beam. To achieve this, the emission origin O is *virtually* placed behind the transducer face [9]. SIRI offers the highest possible reconstruction rate - both in terms of echo acquisition and processing - and has very low memory requirements. This comes at the cost of a degraded image quality due, in particular, to the lack of focusing in transmit; i.e. the emitted acoustic energy is spread too broadly. This reconstruction technique is at the basis of ultrafast imaging (Section 2.3.2).

6.3.2 Zone Imaging

Zone sonography (Section 2.3.3) has been additionally implemented on our single-FPGA system. The zones are imaged in sequence, based on dedicated insonifications, each of which consisting of a more focused beam than the one required for SIRI. The virtual non-overlapping divisions of the ROI can be done in any of the imaging dimensions. Figure 6.3 shows two different examples of dividing the ROI; one is at the azimuth direction (Figure 6.3(a)), and the other is at the radial direction (Figure 6.3(b)). In this work, we slice the ROI in the azimuth direction for the 2D case, and in the azimuth and elevation directions ("sub-pyramids") for the 3D imaging case. Each zone's emission profile originates from a *virtual source* O that moves on an imaginary arc behind the transducer face.

Our imager currently supports 2, 4, 8 (2D) or 2×2 , 4×4 , 8×8 zones (3D). An increased zone count improves lateral resolution, but comes with a proportional cost in terms of acquisition time. However, the processing time, processing resources, and memory requirements are

almost the same. Compared to SIRI, there are two main differences in the processing pipeline: the first is the usage of different sub-Tx delay tables for each zone according to the different emission origins O (Section 4.3 and Figure 4.3(b)), while the second is an extra “stitching” step, performed by the beamformer while storing the beamformed data in the DDR to join the zones.

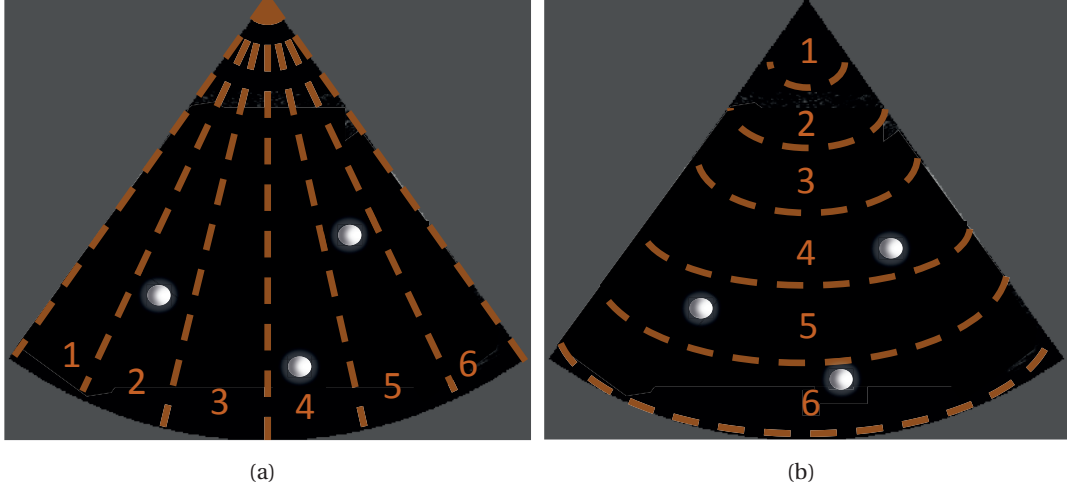


Figure 6.3: A sketch depicting two different ways of dividing *virtually* the ROI in zone imaging; (a) the 6 zones are in the azimuth direction, and (b) the 6 zones are in the radial direction. This yields lateral or radial resolution improvements, respectively.

6.3.3 Compound Imaging

Our platform also supports incoherent spatial compound imaging (Section 2.3.4). Incoherent spatial compounding has been considered [141–143] as a promising technique for reducing the speckle and clutter effects [58, 144] of the US images, with the ability to improve the organ delineations and boundaries, while coherent compounding is useful for enhancing the image resolution.

To support spatial compounding, we provide the possibility to steer the emission origin by e.g. 0° , $\pm 10^\circ$, $\pm 20^\circ$ in both azimuth and elevation (or in azimuth only for 2D case). The beamformer, if so programmed, will automatically rotate between a configurable number of origin permutations, yielding slightly different images each time. Spatial compound imaging can be considered as a special case of zone imaging where all the contributing zones are fully overlapped and insonified by wider US profiles covering the whole ROI. The compounding operation itself is lightweight, and we have chosen to implement it in software on the platform’s MicroBlaze, although hardware acceleration would be possible too. Different operators can be used for compounding in order to formulate one final image out of the contributing reconstructions [143, 145]. Our design currently supports the typical *averaging* operator as well as the *averaging-excluding-the-brightest-voxel*, *minimum brightness voxel*, and *maximum*

brightness voxel compounding, and can be easily extended further. Compound imaging increases the acquisition time similarly to zone imaging, but also incurs extra processing time and brings extra memory requirements. This is because of the need for multiple insonifications, multiple full BF passes, and the storage of multiple full images (although this can be off-FPGA) before the compounding step can be performed.

6.4 System Quality Evaluation In Different Modes

In this section, we assess the image reconstruction quality when using the different supported imaging modes: SIRI, zone-, and compound imaging. Different quality metrics have been used for the purpose. The *Point Spread Function (PSF)* has been used to evaluate the lateral resolution benefits of zone imaging over SIRI. *Peak Signal-to-Noise Ratio (PSNR)* has been used to evaluate the speckle noise suppression of compound imaging over SIRI. The *Contrast Ratio (CR)* has been used to evaluate the output image contrast in each of the three modes. Further, a visual assessment is proposed in Section 6.4.4.

6.4.1 Point-Spread Function (PSF)

We have evaluated our zone imaging implementation and its impact on the reconstruction quality by insonifying a single point scatterer while varying the zone count. The result is measured in terms of the PSF contours, and the projections thereof, to evaluate the lateral resolution and the height of the sidelobes. Two representative scatterers; one is at $\theta = 0^\circ$, $\phi = 0^\circ$, $r = 60$ mm and the other is at $\theta = -15^\circ$, $\phi = 0^\circ$, $r = 60$ mm, have been chosen for this analysis for space reasons. We divided the ROI into 2×2 zones (Figures 6.4(b), 6.5(b), 6.4(f) and 6.5(f)), 4×4 zones (Figures 6.4(c), 6.5(c), 6.4(g) and 6.5(g)), and 8×8 zones (Figures 6.4(d), 6.5(d), 6.4(h) and 6.5(h)). The zones span a fraction of the azimuth and elevation angles, i.e. they cover sub-quasi-pyramids of the overall volume. A SIRI (i.e. 1-zone) reconstruction is shown in Figures 6.4(a), 6.5(a), 6.4(e) and 6.5(e). The expected scatterer location is denoted by a "+" symbol in the figures. For the SIRI case, Figure 6.4(e) and 6.5(e) show that the PSF projection has a wide main lobe and a high sidelobe level. This result is expected since in SIRI the insonification of a whole 3D ROI is based on a single US beam, leading to a major dispersion of acoustic energy, which correlates negatively to resolution. The rest of the sub-figures prove that there is a direct relationship between the number of zones and the improvement in the image quality, especially in terms of lateral resolution. This confirms the theoretical expectations, since the ROI is now divided in slices, each insonified with a more focused and therefore higher-energy-density beam. A notable reduction can be observed in the level of the sidelobes compared to the main lobe, while the main lobe width becomes narrower and the contours become more concentrated around the scatterer's actual location.

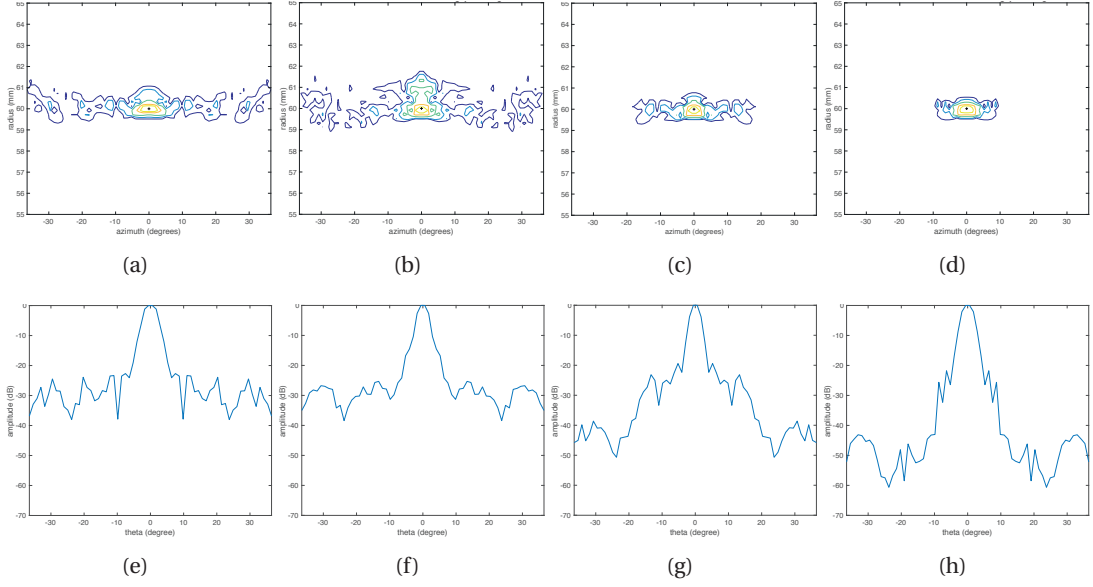


Figure 6.4: Evaluation of our zone imaging implementation versus SIRI in terms of PSF contours and projections for a scatterer at $\theta = 0^\circ$, $\phi = 0^\circ$, $r = 60$ mm. This is achieved by testing the reconstruction when dividing the ROI into, (a) and (e) SIRI, (b) and (f) 2×2 zones, (c) and (g) 4×4 zones, (d) and (h) 8×8 zones. The PSF contour colors represent the level in dB, in a range of -5 dB, -10 dB, -20 dB, -30 dB, -40 dB from inside to outside.

6.4.2 Peak-Signal-To-Noise Ratio (PSNR)

PSNR is a quality metric used to quantify how far the image under test is from a reference image. It measures the ratio between the maximum possible energy level in the image and the total energy of the noise (i.e. the error between the image under test and the reference image). PSNR indicates the precision and reliability of the reconstruction. PSNR is defined as follows:

$$PSNR = 20 \log_{10}(MAX) - 10 \log_{10}(MSE). \quad (6.1)$$

MAX represents the maximum voxel brightness in the image. Since we log-compress the reconstructions onto a grayscale range of (0 - 255), MAX is equal to 255. MSE is the Mean-Square-Error defined as:

$$MSE = \frac{1}{A \times E \times R} \sum_{a=0}^{A-1} \sum_{e=0}^{E-1} \sum_{r=0}^{R-1} [V_{ref}(a, e, r) - V_{test}(a, e, r)]^2, \quad (6.2)$$

where A , E , and R are the azimuth, elevation, and radial dimensions of the volume V . V_{ref} is the reference volumetric image, while V_{test} is the volumetric image under test. We have considered V_{ref} as the output volume of compounding 9 frames using the averaging operator

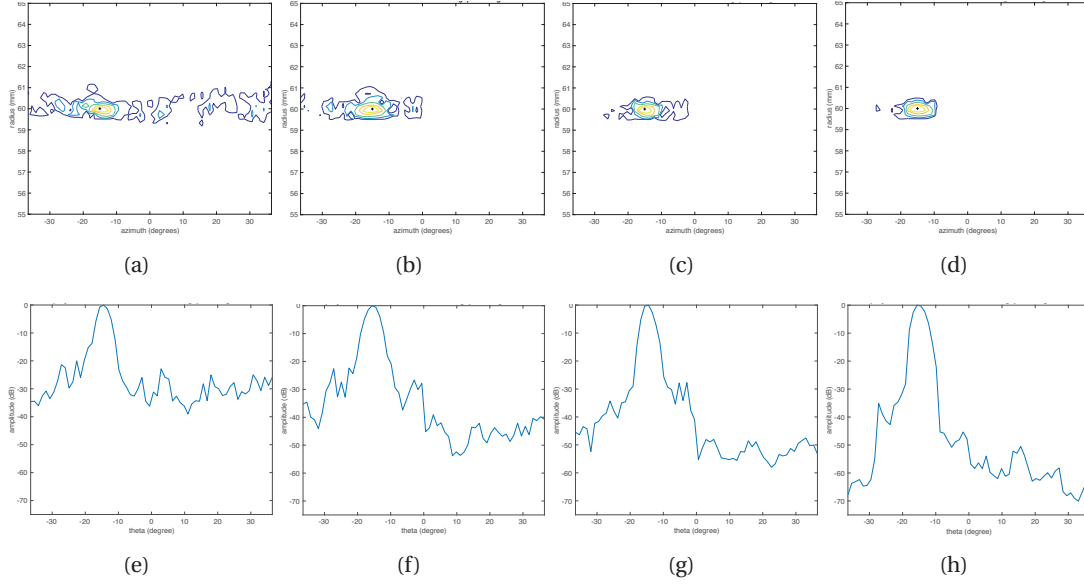


Figure 6.5: Evaluation of our zone imaging implementation versus SIRI in terms of PSF contours and projections for a scatterer at $\theta = -15^\circ$, $\phi = 0^\circ$, $r = 60$ mm. This is achieved by testing the reconstruction when dividing the ROI into, (a) and (e) SIRI, (b) and (f) 2×2 zones, (c) and (g) 4×4 zones, (d) and (h) 8×8 zones. The PSF contour colors represent the level in dB, in a range of -5 dB, -10 dB, -20 dB, -30 dB, -40 dB from inside to outside.

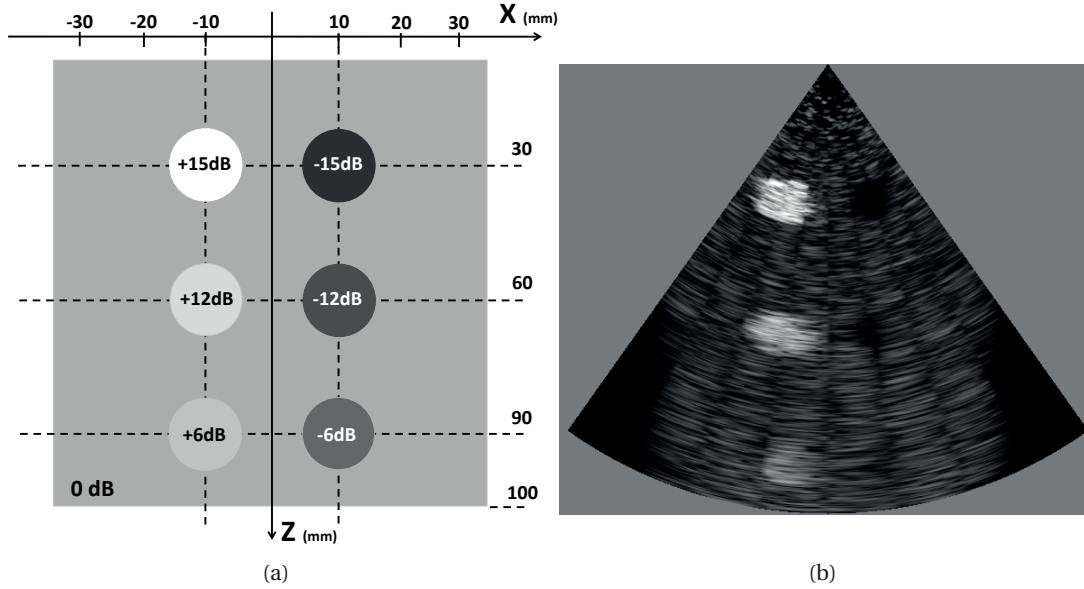


Figure 6.6: Our 6-cyst phantom. (a): sketch depicting the geometry of the phantom. (b): phantom reconstruction using phased imaging based on 8 zones diverging insonification.

and - most importantly - reconstructed based on *exact* delay calculation BF. The volumes under test V_{test} are the output of either SIRI or compounding different number of frames,

6.4. System Quality Evaluation In Different Modes

reconstructed based on our SHEDA *approximate*-delay calculation approach as implemented on the FPGA. For the analysis, we have used a 6-cyst Matlab phantom developed in house and shown in Figure 6.6. The phantom comprises 6 cysts of radius 5mm, with reflectivity of +15dB, +12dB, +6dB, -15dB, -12dB, and -6dB compared to the background tissue.

Table 6.1 shows the PSNR in dB for: (i) a single volume, (ii) the output of 3-, 5-, and 9-frame compounding with the *average* operator, and (iii) the output of 9-frame compounding with the *average-excluding-the-brightest-voxel* operator. The results show progressive removal of the speckle as we increase the number of compounded volumes. Moreover, the choice of the compounding operator plays an important role in the noise suppression.

Table 6.1: PSNR For Compound Imaging And SIRI.

* *Reference volume: 9-frame compounding using averaging operator and based on exact delay calculation BF*

Image under test	PSNR (dB)
Single volume (SIRI)*	34.1
3-compounding, average*	38.8
5-compounding, average*	41.2
9-compounding, average*	45.2
9-compounding, average-excluding-brightest*	41.2

6.4.3 Contrast Ratio (CR)

We have further appraised the image quality of our prototype outputs using the CR metric. CR is measured by selecting two regions in the image, one is for the structure of interest (i.e. a cyst), while the other is for the background. The CR is the ratio between the mean brightness of those two regions in dB, as follows:

$$CR = 20 \log_{10} \frac{Mean_{test}}{Mean_{reference}}. \quad (6.3)$$

For this measurement, we have used the same cyst phantom described earlier. Table 6.2 and Table 6.3 show the CR evolution when varying the compounding count and zone count, respectively. The following trends can be observed:

- The CR of each cyst does roughly follow the expected brightness trend, i.e. bright cysts are brighter than the background, which is brighter than the dark cysts.
- However, the CR does not match the theoretical expectations too well in Table 6.2 and the first row of Table 6.3. We attribute this to the very bad lateral resolution of the imager when the whole volume is insonified with a single emission, as discussed in Section 6.4.1.

Table 6.2: CR For Compound Imaging and SIRI.

Volume under test	+15 dB CR (dB)	+12 dB CR (dB)	+6 dB CR (dB)	-15 dB CR (dB)	-12 dB CR (dB)	-6 dB CR (dB)
Single volume (SIRI)	19.3	16.1	6.8	-3.7	-2.6	-2.3
3-compounding, average	18.4	16.7	7.1	-4.9	-2.6	-2.2
5-compounding, average	18.2	16.8	7	-5.1	-2.4	-2.3
9-compounding, average	18	16.5	7	-5.4	-2.7	-2.2
9-compounding, average-excluding-brightest	18.9	16.6	7	-5.2	-2.1	-1.9

Table 6.3: CR For Zone Imaging and SIRI.

Volume under test	+15 dB CR (dB)	+12 dB CR (dB)	+6 dB CR (dB)	-15 dB CR (dB)	-12 dB CR (dB)	-6 dB CR (dB)
Single zone volume (SIRI)	17.9	17	7.6	-4	-3.7	-2.2
8 × 8 zones volume	26.7	17.2	9.7	-11.4	-8.7	-3

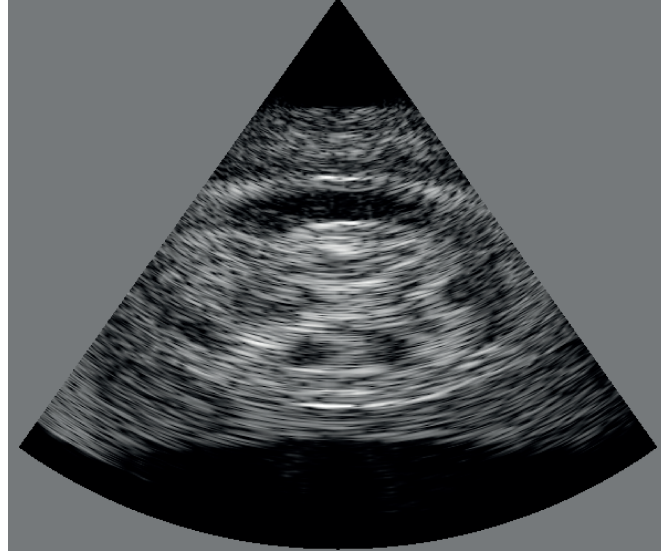
In practice, the bright cysts on the left side of the image “bleed into” the dark ones on the right, dramatically reducing the contrast. This effect is expected.

- *Incoherent* compound imaging is not expected to improve contrast rates significantly, and indeed has a negligible impact on CR figures (Table 6.2).
- On the other hand, zone imaging can dramatically improve lateral resolution and therefore cancel out the bleeding effect. This is strongly confirmed by the second line of Table 6.3. This row shows a much better match between expected and measured CR, and a much better correlation of the relative brightness of the cysts. We expect that an even higher zone count would further improve the CR numbers, of course at a frame rate cost.

6.4.4 Visual Assessment

In this section, a visual assessment based on the appearance of the reconstructions is performed. We show sample 3D reconstructions from our imager based on a fetus phantom available on the Field II simulator website [8]. Figure 6.7(b) shows an 8 × 8 multi-zone reconstruction versus a SIRI image (Figure 6.7(a)). The multi-zone reconstruction shows a clear improvement in the contrast and lateral resolution, as expected. A post-processing lateral low-pass-like filtering might be appropriate to smooth the transitions at the zone edges; however, this could be performed easily at the hospital side.

Figure 6.8 shows reconstructions achieved by compounding different numbers of frames, versus a single frame. Figure 6.8(a) shows single-frame reconstruction (SIRI). Figures 6.8(b)-6.8(d) show the compounding of 3, 5, and 9 frames, respectively, using a simple *average* operator. These clearly demonstrate the capability of the imager to filter out the speckle noise.



(a)



(b)

Figure 6.7: 3D imaging of a fetus phantom available online on the Field II website [8]. The images show the middle azimuth-depth plane (i.e. middle elevation plane) of the reconstructed volume by our imager. The imaging volume is $73^\circ \times 73^\circ \times 10cm$. (a) is a single-zone image, i.e. SIRI, based on a single diverging beam insonification, while (b) is an 8×8 zone image, where each zone is insonified independently with a more focused beam.

Different levels of noise reduction can be achieved by adjusting the compounding degree, at the expense of the reconstruction rate. The compounding operator plays also an important role in the quality of the final image. In the presented example, the *average-excluding-the-brightest-voxel* operator used in 6.8(e) shows better contrast and noise reduction than the

typical *average* operator (Figure 6.8(d)). Overall, the imager provides options to tune the level of noise reduction and contrast in the final image; the best choice would depend on the structure being imaged.

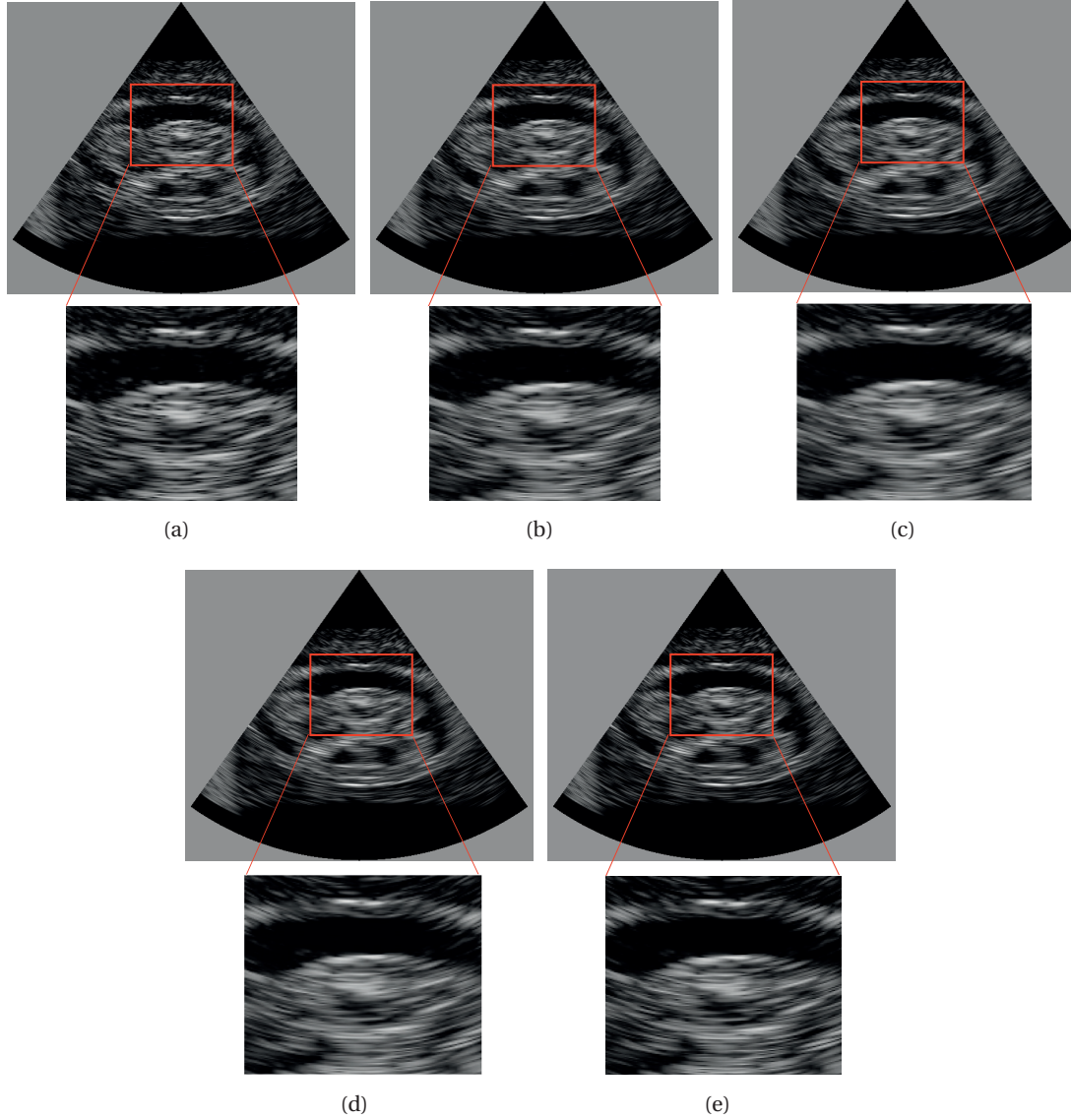


Figure 6.8: 3D imaging of a fetus phantom available online on the Field II website [8]. The images show the middle azimuth-depth plane (i.e. middle elevation plane) of the volume reconstructed by our imager. The imaging volume is $73^\circ \times 73^\circ \times 10\text{cm}$. (a): single frame, i.e. SIRI. (b) to (d): 3-frame, 5-frame, and 9-frame compounded images, using the *average* operator. (e): 9-frame compounded image using the *average-excluding-the-brightest-voxel* operator.

6.5 Summary

In this chapter, we have clarified both our optimizations for the post-processing and visualization unit, and the supported imaging modes by the proposed 3D-imaging prototype. The resource-friendly demodulation algorithm and its realization, our telemedicine-suitable idea of the cross-sectional SC, and the system ability to provide HDMI video output on a screen have been elucidated here.

In this chapter, we have discussed the three supported imaging modes by our single-board 3D system. Further, we have reported the detailed quality assessment of each of those modes based on different quality measures.

As a future work, it will be needed to develop a volumetric visualization system on the hospital side - where there is no limitation on the resources - to allow the sonographer investigating easily the received volume(s) and reaching efficiently the diagnosis. The virtual reality technologies can be a great tool to achieve that aim in a very interactive and fascinating way.

7 I/O Interfacing, System Communication, Probe Localization, and Platform Results

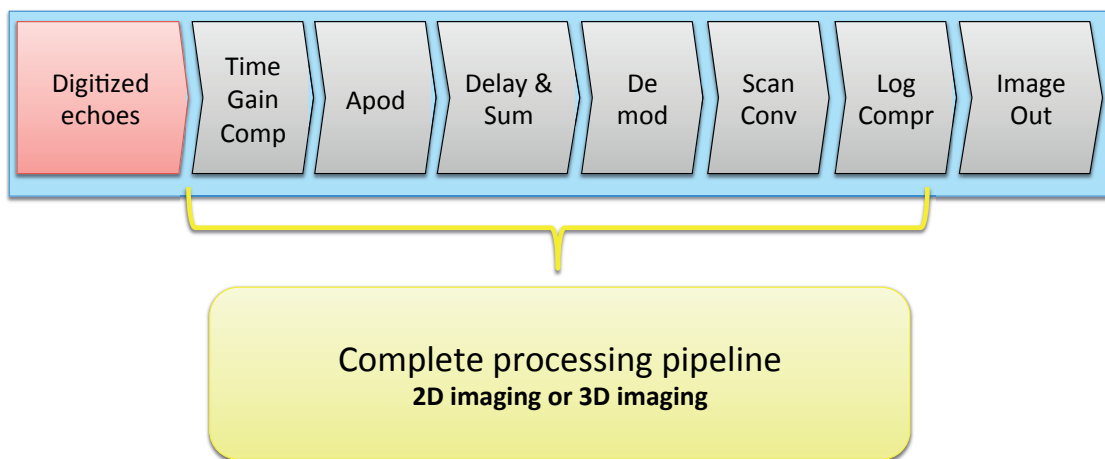


Figure 7.1: Logical processing flowchart of the US image reconstruction pipeline.

In Chapters 4, 5, and 6, we explicated the careful optimization performed in our digital US compact processor, without raising the input interfacing issue (Challenge 1). In this chapter, the two supported means of input are dissected: (i) the optical connection with a probe for realtime data input (Section 7.1), and (ii) the Ethernet connection with a laptop for simulated input (Section 7.2). This includes the reasoning behind each choice, the implementation details, the limitations, and a discussion to further extend to interface with a physical matrix probe whenever available.

In addition, miscellaneous aspects of our system architecture are discussed: the data representation (Section 7.3), the depiction of the communication logic between the FPGA, the

Chapter 7. I/O Interfacing, System Communication, Probe Localization, and Platform Results

MicroBlaze, and the GUI (Section 7.4), and the platform self-bootability (Section 7.5).

Our single-FPGA imager unlocks teleosonography usage scenarios by allowing the decoupling of acquisition from diagnosis. However, this decoupling will introduce an issue since the scans collected by a non-sonographer will not be labeled or identified according to their origin; i.e. meaningless for diagnosis. In Section 7.6, we propose two solutions to bridge that gap: an automatic approach, and a manual approach by guidance.

Finally, a detailed assessment for the whole platform, in terms of resource utilization (Section 7.7.1), system performance (Section 7.7.2), overall quality evaluation (Section 7.7.3), and prototype portability and estimated cost (Section 7.7.4), is reported. The FPGA utilization has not only been evaluated for the 2D and 3D designs specified in Table 1.1 but also for further upscaling to support higher number of channels.

7.1 Optical Connection With a Probe

In order to provide realtime data to the processing platform, an efficient communication channel with a probe should be chosen. Due to the high bandwidth requirements, especially for 3D imaging, the two preferred options to connect a probe to our KCU105 board [146] are either over the optical Small Form-Factor Pluggable (SFP) ports or the *Peripheral Component Interconnect Express (PCIe)* interface. The latter implies higher complexity, in terms of design and cabling, as well as higher power consumption, so the optical interface is favoured.

As a demonstration of this interface and since there has not been an open matrix probe available during the timeline of our research, in a collaboration with the *Swiss Federal Institute of Technology in Zurich (ETHZ)*, we have connected to our design a probe for 2D imaging. This array probe comprises 64 elements and features a 4 MHz center frequency, and is designed with optical connection support [10]. The ADCs in the probe sample the data with 12-bit resolution at 20 MHz. The sustained output bandwidth is thus of around 15.3 Gbps. To support it, the *Quad enhanced Small Form-factor Pluggable (QSFP+)* interface is used by the probe; each of its four SFP+ lanes has a nominal bandwidth of 6.25 Gbps and a net one of 5 Gbps, for a total of 20 Gbps. Each lane is driven by a Xilinx Aurora 8b10b LogiCORE IP [147] for lightweight, scalable, and high-speed serial communication.

Within our Kintex FPGA, we have also implemented a 4-lane Aurora input channel. Since the KCU105 board [146] natively only features two SFP+ ports, we have connected an intermediate QSFP+ board to the *FPGA Mezzanine Card (FMC)* interface [148] on the KCU105 (Figure 7.2).

To connect a 3D imaging probe with $32 \times 32 = 1024$ channels, assuming the same sampling frequency and resolution specified in Table 1.1, the bandwidth requirements would increase by 16 times to 245 Gbps. The theoretical maximum bandwidth allowed by the SFP+ specification is of 16 Gbps per link, i.e. 64 Gbps for a whole QSFP+ link. Considering an Aurora 8b10b module with its 20% overhead [147], the required bandwidth would reach 294 Gbps. Even with

a more compact encoding, as allowed by an Aurora 64b66b module [149] (3% overhead), the raw bandwidth would reach 253 Gbps and therefore would require a minimum of four QSFP+ connections ($253/64 \approx 4$). This is not presently implementable on the KCU105 development board due to the hard-wired connection of the FPGA transceivers to a variety of different interfaces, which poses a limit of two QSFP+ connections. Nonetheless, by developing a custom board, it is possible to use all 20 GTH transceivers of the KU040 FPGA towards the probe interface, resulting in up to five QSFP+ interfaces with an aggregate maximum bandwidth of 320 Gbps, which meets the requirements of 3D imaging. For even further scalability to higher channel counts or sampling rates, other FPGA chips of the Kintex Ultrascale family offer up to 64 GTH transceivers, thus providing at least three times more bandwidth.

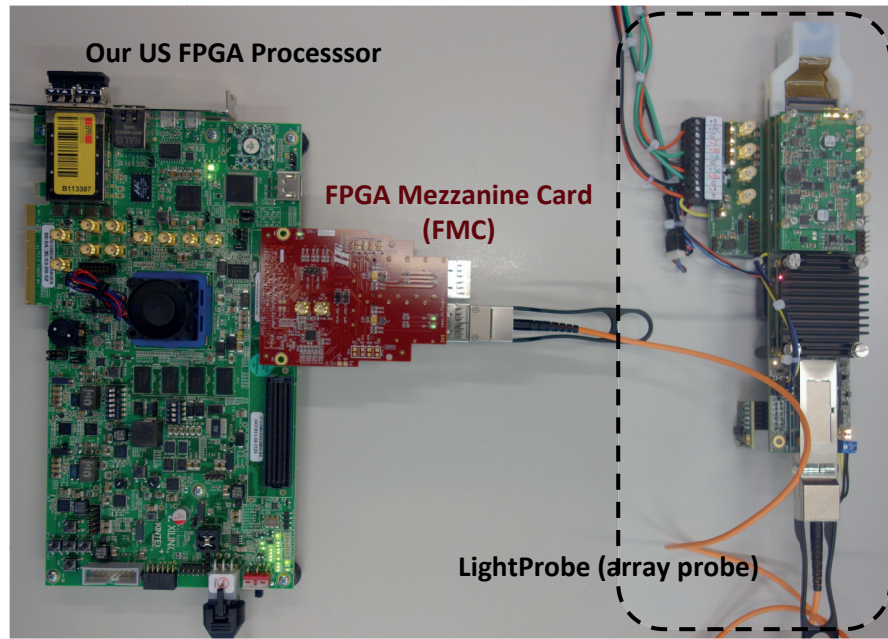


Figure 7.2: The optical connection between our US digital processor and the LightProbe probe [10], while utilizing a Mezzanine board as an interfacing between the units. The LightProbe is a 1D probe for proof-of-concept and to be replaced with a matrix probe whenever available.

7.2 Ethernet

To feed our imager with 3D data for development and debug, offline simulated RF echoes have been used. These data were obtained using the Field-II simulator [125] for Matlab fed with a description of the chosen matrix probes and 3D phantoms. For this 3D development mode, we have utilized an Ethernet port as the data transmission mean between a laptop with Matlab and the FPGA (Figure 7.3). The availability of simulated data is very beneficial as it provides a golden reference image, which helps in both debugging and quality assessment. Therefore, we optionally use the simulated data input for 2D imaging case as well as the realtime input by the probe. The Ethernet bandwidth is 1Gbps. Obviously the bandwidth of the Ethernet link

Chapter 7. I/O Interfacing, System Communication, Probe Localization, and Platform Results

proves to be a performance bottleneck, but an advantage of this setup is the extra scope for flexibility and debug (Section 7.4).

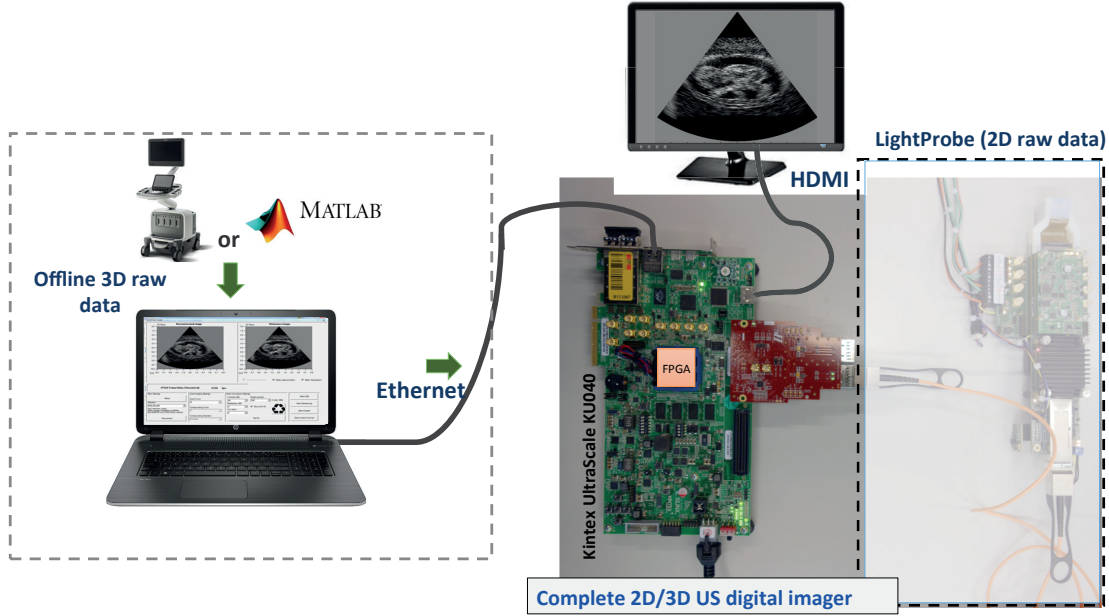


Figure 7.3: Setup of the design for 2D and 3D US imaging. The components in the dashed box to the left are for development, debugging and verification only.

7.3 Data Representation

The binary representation of data input, processing coefficients, and design parameters has been optimized for accuracy versus resource utilization.

- Input samples adopt a 16-bit signed integer representation, which is consistent with the highest-precision ADCs in use in US imaging. It also allows to load two samples per cycle via a 32-bit bus into the sample BRAMs.
- The apodization values are represented with 18-bit unsigned fixed-point (2.16) precision, since they represent multiplicative coefficients that range between 0 and 1 and which can be very small at the corners of the transducer. This width is optimized for the Xilinx BRAMs row width [32], i.e. 18 bits.
- The TGC values are represented with 18-bit unsigned fixed-point (9.9) precision, since they represent multiplicative coefficients whose values can reach that number of bits for both the integer and the fractional parts. This is according to Equation 5.6, the typical US imaging depths, and the specifications in Table 1.1.
- The delay values are calculated with 18-bit fixed-point (± 13.4) precision, since that maximizes the accuracy while still allowing to fit various steering coefficients into the

18-bit-wide Ultrascale BRAMs. After the delays have been fully computed according to Equation 4.7, they are rounded to 10-bit positive integers to index into the input sample BRAMs.

- The low-pass FIR coefficients of the demodulator are stored in 36-bit signed fixed-point (± 7.28) precision, since they can be either positive or negative, and can have very small values.

Throughout the beamformer pipeline, care is taken to preserve signal precision while minimizing resource utilization. All the coefficients that are pre-calculated are generated in Matlab and then loaded into the beamformer either at synthesis time, via include files, or at FPGA boot time, via BRAM initialization in the bitstream.

7.4 FPGA, MicroBlaze, and GUI Communication

For several reasons - such as ease of configuration, debugging, ability to provide arbitrary input data, storage of the outputs, comparison to a Matlab golden reference - we provide a facility to interface the board to a developed C#-based *GUI* running on a separate laptop. Figure 7.4 shows the developed GUI where the user can, for example, specify “*zone count*” and “*compounding count*” parameters, which determine the imaging mode (Section 6.3).

The GUI and the Microblaze control software run in lockstep, communicating over an Ethernet cable, and the user can control all settings from the laptop (Figure 7.5). These settings are sent from the laptop to a packet processing stack running on the MicroBlaze; the latter then programs the BF block accordingly. Various SC settings are similarly conveyed from the GUI via the MicroBlaze to the SC block.

The board can receive the echo inputs from a probe in realtime over the optical connection (Section 7.1), with minimal involvement of the GUI and MicroBlaze. However, artificial data can also be sent from the GUI (Section 7.2), which presides over a small database of phantoms - as shown in Figure 7.4 - which were pre-simulated in Matlab with the Field II [125] package. In either case, the BF block then starts processing, which includes the TGC, apodization, delay-and-sum, and demodulation. The resulting image data is placed, with a direct hardware copy, onto the DDR memory off-FPGA. A status flag is then set, allowing the MicroBlaze software to detect, via polling, the completion of the process. Depending on the zone/compound imaging settings, this sequence could execute multiple times. Eventually, the MicroBlaze sends a command to the SC block, including again various parameters such as resolution, brightness, and contrast. The SC is also able to autonomously fetch the beamformed data from the external DDR memory thanks to its master AXI interface, offloading the MicroBlaze from this task. The output image is sent over a fast hardware path to the HDMI controller for display on screen, as well as stored into a different DDR memory location from which the MicroBlaze can - relatively slowly - send it back over Ethernet to the GUI for additional inspection.

Chapter 7. I/O Interfacing, System Communication, Probe Localization, and Platform Results

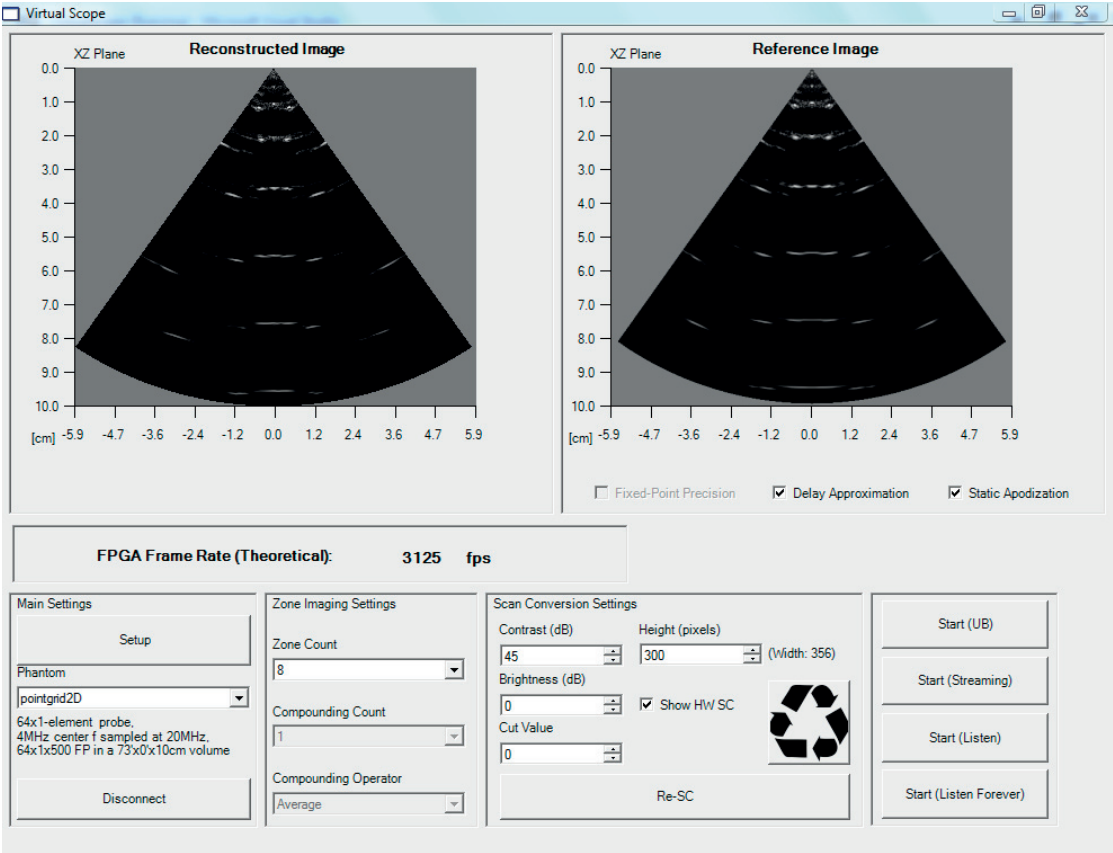


Figure 7.4: A screen-shot of our C#-based GUI. Different imaging modes' and SC settings can be specified via the GUI, which then communicates with the MicroBlaze and the FPGA.

7.5 Platform Self-Bootability

The prototype FPGA board of this work is meant to be operable standalone. In particular, the FPGA imager is self-bootable, via a *Quad Serial Peripheral Interface (QSPI)* module that loads the bootloader software from the on-board flash memory. The bootloader in turn loads the merged bitstream of both the FPGA *.bit* file and the MicroBlaze *.elf* file, stored in the on-board flash. In Figure 5.11, the flashing blocks are represented in rose color.

7.6 Probe Positioning Guidance - Bridging the Telesonography Gap

Normally, the sonographer has full control over the positioning of the probe and there is a direct hand-eye coordination allowing the specialist to seek for anatomical features. Telesonography severs this connection and makes it time-consuming or problematic for a remote doctor to even identify the location of a scan. For example, the two kidneys would be essentially indistinguishable from each other if acquired in unlabeled scans. Therefore, it is imperative for the scans to be somehow position-tagged. Yet, a lightly trained operator may not have the

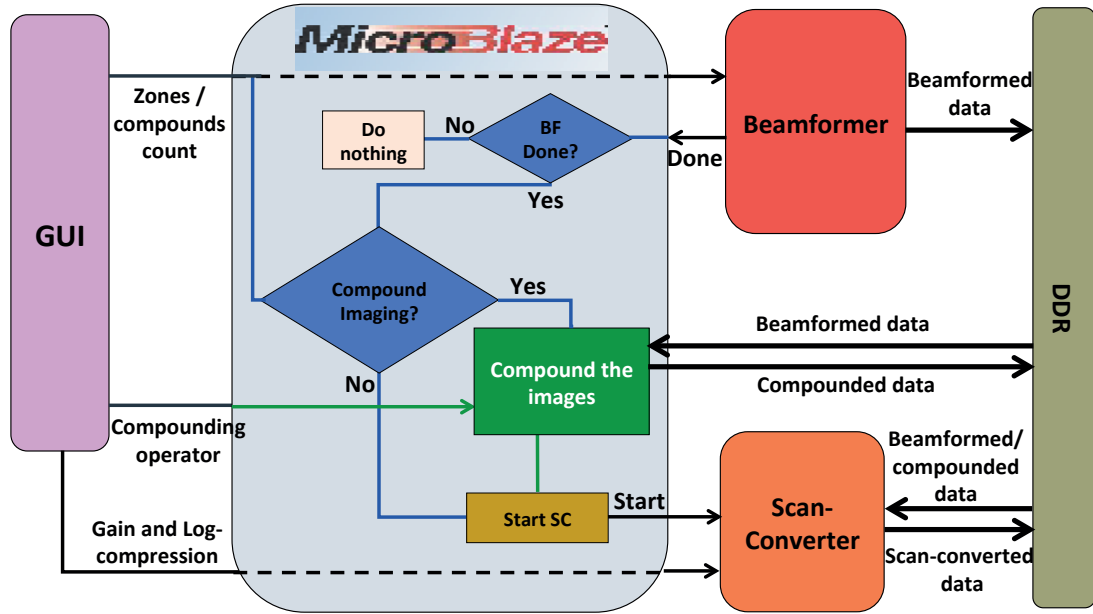


Figure 7.5: The logic of controlling different imaging modes. The communication between the FPGA, the MicroBlaze, and the GUI to handle different options and settings of the processing flow.

necessary expertise or precision.

In this section, two solutions are proposed to fill that gap: (i) an automatic probe localization unit, and (ii) an Android application for probe positioning guidance. The automatic probe localization facility (Section 7.6.1) relies on programming an *Inertial Measurement Unit (IMU)* to automatically identify the origin of the captured scans by tracking the movement of the probe. However, due to the reduced accuracy of the IMU for such medical scenarios, we have developed an android application (Section 7.6.2) that provides guidance and probe positioning charts for common US scans. This strongly helps the operator to manually label the scans. Both approaches aim to ease the remote diagnosis task of the US specialist who gets used to perform the acquisition and the diagnosis both at the same time.

7.6.1 Automatic Probe Localization - IMU

Working Mechanism

The first proposed solution to help labeling the scans is a probe localization module. The module is mechanically attached to the probe and capable of automatically detecting its own position. We choose an iNemo-M1 IMU from STMicroelectronics [150]. It is equipped with 3D gyroscope, 3D accelerometer, and 3D magnetometer in a compact package of $13 \times 13 \times 2\text{mm}$, which is tiny enough to be easily soldered into a transducer head.

Chapter 7. I/O Interfacing, System Communication, Probe Localization, and Platform Results

The evaluation board of the iNemo-M1, STEVAL-MKI121V1 [151], has also been used to easily program and evaluate iNemo-M1. The used sampling frequency of the accelerometer, gyroscope, and magnetometer is 50 Hz, 190 Hz, and 30 Hz, respectively.

We have programmed the microcontroller of the iNemo-M1 with an *Attitude and Heading Reference System (AHRS)* algorithm developed in C. Since the acquired motion signals only convey acceleration and orientation, but not position, the AHRS algorithm is used to define the probe position $P_p(t)$ [152]. Equation (7.1) shows the calculation of $P_p(t)$, where a_m is the measured acceleration, g is the gravitational acceleration ($9.81 m/s^2$), and t_0 and t are the start and end time of measuring a_m , respectively. R_S^I represents the rotation matrix of the body frame of the sensor relative to the inertial frame¹. We have computed R_S^I based on an open source AHRS algorithm [153, 154].

$$P_p(t) = \int_{t_0}^t \int_{t_0}^{t'} a_I(t') dt' = \int_{t_0}^t \int_{t_0}^{t'} \left(R_S^I a_m(t') + \begin{pmatrix} 0 \\ 0 \\ g \end{pmatrix} \right) dt' \quad (7.1)$$

Note that this method requires the definition of a spatial origin, from which to track movement. This can be done with a "reset" button to be pressed when the probe is in a known position over the patient's body, e.g. the base of the sternum. The iNemo-M1 would need to be integrated into the transducer head, which is easily possible due to its small size.

Automatic Positioning Accuracy

The reconstructed position's accuracy is a function of the acquisition time, since any measurement error is integrated over time. We also observed that the accuracy depends on the probe movement pattern; in particular, fast movement with high accelerations is more precisely detected than smooth, constant-speed gestures. Based on our initial results, for an acquisition time of about 10s, the system - calibrated at a reference starting position, e.g. the sternum - is sufficiently precise to detect basic positional coordinates, like "left" as opposed to "right" of the body, or "thorax" as opposed to "abdomen". This can reduce misinterpretation chances, however, more precise localization will need to rely on higher-accuracy systems, e.g. visual or RF tracking, which do not suit on-site usage environment.

7.6.2 Android Application For Operator Guidance

Alternatively, the scans can be manually tagged. To guide an inexperienced user in the task, a companion mobile application can, for a variety of relevant diagnostic scans (e.g., "suspected

¹The frame is the origin and the three physical reference points that define the location and orientation of the coordinate system.

7.6. Probe Positioning Guidance - Bridging the Telesonography Gap

abdominal bleeding”), visually instruct the operator on where to position the probe.

We have developed an Android application that provides the on-site operator help to properly acquire US volumes and manually label the reconstructions. The application provides charts for probe positioning guidance for a group of common US scans. Each chart represents a map on where the probe should be positioned, which accordingly helps the untrained operator to manually label the scans to eventually achieve efficient and reliable remote diagnosis. Figure 7.6 shows samples of these charts; one is for an abdominal scan, and the other is for a liver scan. The application also provides the guidelines for good US practice - like the necessity to apply gel between the probe and the skin -, and the instructions on how to operate the device. Our application is very basic, however, it is sufficient to demonstrate the idea of manual guidance and labeling. Further development can easily be performed to achieve a more attractive and functional interface.

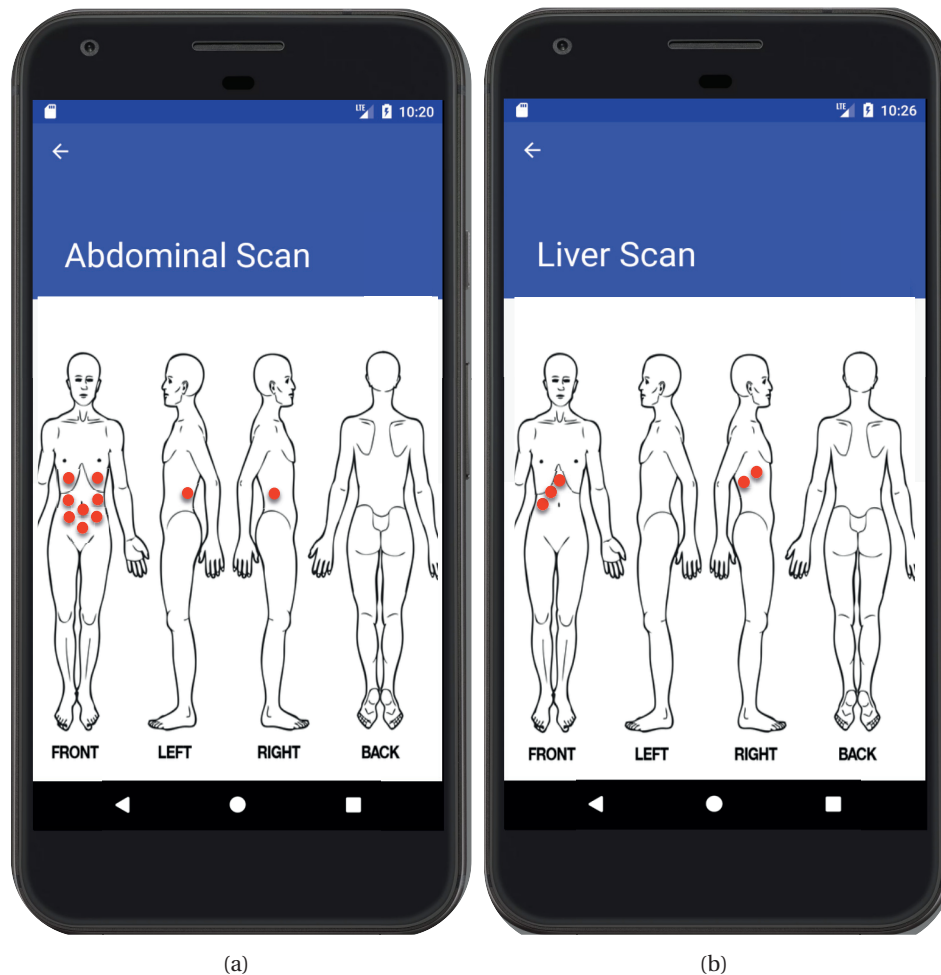


Figure 7.6: Sample shots of the probe positioning charts provided by our android application for common US scans; (a) abdomen scan, and (b) liver scan. The body-view pictures are taken from [11]

7.7 Single-FPGA Digital Imager Evaluation

7.7.1 FPGA Utilization Results

In this section, we report the FPGA resource utilization results achieved with Xilinx Vivado 2017.2.1 [155, 156]. We show results for the two versions of the proposed platform: a 64-channel 2D US imager, and a 1024-channel 3D US imager. The development board we chose, which is well-suited to our requirements, is the Xilinx KCU105 [146] with a midrange Kintex UltraScale KU040 FPGA [32]. Table 7.1 shows the utilization of the two proposed imagers. The two most critical resources are the BRAMs followed by the LUTs. For the BRAMs, 71% of the consumption is by the beamformer, with 42.7% (i.e. 512 BRAMs) just to store the received echoes, which is not further compressible for the given channel count. LUTs are also mostly utilized by the beamformer, followed by the platform's AXI interconnects. Our design contains two 32-bit AXI interconnects; one is configured with a “maximize performance” setting in Vivado, as necessary to support the high bandwidth in particular of the HDMI controller, while the other, which is configured with “minimize area” setting, handles the communication between the remaining blocks. The support for zone and compound imaging does not change substantially the resource utilization, except for the need of additional storage space in the external DDR to hold multiple full frames before compounding.

The proposed architecture can be easily scaled up, if a larger FPGA is adopted. In the third row of Table 7.1, we have also extrapolated the resource utilization of a high-end Virtex UltraScale XCVU190 FPGA when configuring the proposed imager to support 90×90 channels. Naturally, this chip would have much higher cost and power consumption.

The power consumption, as estimated by Vivado [157], of the platform is 4.6 W for the 2D configuration and 5 W for the 3D setup. This is fully aligned with the possibility of deploying the design in a battery-powered medical device. As future work, the actual power consumption of the board can be directly measured with a dedicated Maxim tool [158]. This project will also entail a careful optimization and power management of any board components and interfaces which are not needed by the US imager.

Table 7.1: Imager Resource Utilization.

* Kintex UltraScale KU040 implementation results.

** Virtex UltraScale VU190 extrapolated results.

Supported Channels	Logic	Regs	BRAM	DSP	Clock	Theoretical Reconstruction Rate
64*	37.9%	23.1%	45.6%	5.9%	133 MHz	4157 FPS
32×32*	75.6%	34.6%	97.2%	6.1%	133 MHz	65 VPS
90×90**	79.7%	31.5%	69.9%	6.5%	133 MHz	65 VPS

7.7.2 Performance

In the proposed final imaging system, the acquisition rate (i.e. the cadence of the images to be stored and uploaded to the hospital) and the display rate (i.e. the images to be displayed on a local screen, after SC, for the operator to monitor) can be decoupled. The proposed digital imager runs at 133 MHz, and the BF rate is 1 FP per clock cycle. This means that according to our system specifications (Table 1.1), the *theoretical* reconstruction rate (Table 7.1) is 4157 FPS in the 2D case, and 64.9 VPS in the 3D case, which is more than sufficient to upload high-temporal-resolution streams of images ("4D" US) to a hospital. The SC rate on the other hand is currently 14 FPS at 356×300 resolution for both 2D and 3D cases. This bottleneck only applies to the realtime visualization capability, but high frame-rate reconstructions can still be performed and uploaded. The *actual* reconstruction rate also depends on the time necessary for the insonification and especially on the echo sample acquisition from the probe, which is discussed later.

The highest possible frame rate is achieved with SIRI, yielding the best frame rate at the cost of the reconstruction quality. Table 7.2 shows the performance achievable in different modes; SIRI as a reference, zone imaging of Z zones, and compound imaging of C compounds. The peak BF rate in zone imaging is the same as in SIRI since there is no overlapping of the zones - although the insonification count of Z will impact the actual reconstruction rate. Compound imaging, on the other hand, reduces both the theoretical and actual reconstruction rate linearly by a factor of C . The SC cost remains constant in all modes, except that when in compounding mode, an additional averaging step of the raw frames is required.

Due to the impossibility to access fast a probe for 3D imaging research during our research timeline, a test setup requires feeding inputs and configuring settings over the Ethernet port. In this debug configuration, the output images are also transmitted back over the same connection for inspection. The Ethernet bandwidth of 1 Gbps and the related MicroBlaze IP software stack become a crucial bottleneck, resulting in a SIRI rate of about 0.02 FPS for 3D. Zone and compound imaging incur a further degradation (Table 7.2), due to the need to send multiple insonification data sets.

A fully-functional 2D prototype with the US probe connected to the Aurora input is currently displaying output images at 0.7 FPS, limited by a software bottleneck in the copying of the scan-converted image - which is in the DDR - to the HDMI port for drawing on the screen. We plan to optimize it away by the use of a *Direct Memory Access (DMA)*, leading to a projected frame rate close to the 14 FPS mark.

7.7.3 Quality Assessment

Our design achieves excellent resource efficiency at the cost of a slight inaccuracy in image reconstruction. The two main causes are the steering-based approximate delay calculation algorithm (i.e. SHEDA), and the use of static apodization.

Chapter 7. I/O Interfacing, System Communication, Probe Localization, and Platform Results

Table 7.2: Imager performance scaling in different imaging modes.

* *Insonification time for a single emission.*

** *BF rate for a single ROI, either volume or image, reconstruction.*

*** *SC rate for a single frame.*

Imaging Mode	Insonification Time	BF Time	SC Time
SIRI	IT*	1 / BR**	1 / SR***
Zone imaging (Z)	$Z \times IT$	1 / BR	1 / SR
Compound imaging (C)	$C \times IT$	C / BR	1 / SR + Fusion time

For the former, in Section 4.4.1, we have mathematically analyzed the image quality on reference images, and have confirmed - as theoretically expected - that the introduced inaccuracy occurs only very close to the probe surface and at the extreme lateral edges of the ROI. These regions are usually not critical for diagnosis, and in practice the disturbance is limited to a minor speckle pattern difference. Nonetheless, a detailed inaccuracy quantification using different metrics has been performed in Section 4.4. This has also included the evaluation of the error due to the fixed-point representation of the delays and the final rounding to integer indexes. A mathematical model to compensate for this introduced inaccuracy has been accordingly proposed in Section 5.1.1, followed by a quality evaluation for the delay algorithm after applying that scheme. Nonetheless, this compensation scheme (i.e. SCA scheme) has not been implemented on our FPGA (Section 5.1.1 shows the discussion).

For what concerns static apodization (Section 5.1.2), we have evaluated the impact of this optimization, finding that it only affects the shallowest 0.32cm of the ROI in our 3D setup (and 0.7cm in our 2D setup), which overlaps with the inaccuracy introduced by our SHEDA algorithm. The same considerations apply.

In Section 6.4, a detailed quantitative and qualitative assessment for the whole system in its different supported imaging modes is extensively performed. The evaluation shows the quality impact and the trade-offs between different modes.

7.7.4 Platform Portability and Estimated Cost

Our current prototype leverages a standard Xilinx KCU105 development board, which is obviously not optimized for price or size. Nonetheless, we note that we could acquire the board for about 3000\$. The QSFP+ Mezzanine Card (FPGA) interface needed to add a high-speed optical interface retails for about 500\$, while the iNemo-M1 IMU to track the probe position can be acquired for less than 100\$. Even including a screen, a battery and casing, the total bill of materials is therefore less than 4000\$, excluding the probe. We estimate that a custom, optimized, mass-produced *Printed Circuit Board (PCB)* would probably reduce the design cost in half. This compares extremely favorably to commercial 3D systems, which retail for up to 100,000\$, and potentially enables a wide adoption.

At the moment, the size of the prototype is dominated by that of the KCU105 board, i.e. $26.7\text{cm} \times 14\text{cm} \times 0.16\text{cm}$. Even without any redesign, this would be clearly compatible with a portable device. The estimated power consumption is comparable to that of a laptop CPU, suggesting that full-day operation with an inexpensive and compact battery is possible. The iNemo-M1 would need to be integrated into the transducer head, and was in fact chosen partially due to its small size ($13 \times 13 \times 2\text{mm}$), which makes the integration easily possible.

Overall, we believe that our prototype, in addition to being the first attempt at demonstrating a feasible telesonography platform and supporting an extremely high channel count, achieves an unprecedented performance/power/cost trade-off.

7.8 Summary

Through this chapter, various aspects of the design have been expounded; (i) the two means of data input supported by our platform, optical connection with a piezoelectric probe for realtime input (2D imaging) and Ethernet communication with a laptop for off-line input (for both 2D and 3D imaging), (ii) the representation precision of every processed parameter in our single-FPGA architecture, (iii) the logic of FPGA, MicroBlaze (microprocessor), and GUI communication, (iv) the design flashing and platform self-bootability, (v) the two proposed solutions for probe positioning and scans labeling, (vi) and finally, the detailed assessment for the whole design (2D and 3D) in terms of resource utilization, performance, quality, portability, and cost.

8 Conclusion and Future Directions

In this thesis, the first telesonography-capable imager has been proposed. It is a complete volumetric US digital processing system that includes pre-processing, core reconstruction, and post-processing units. Our prototype supports up to 1024-channel data reconstruction (state-of-the-art) on a single FPGA, with a material cost of less than 4000\$, and an estimated power consumption of 5 W. Two input means are featured by the design; high-bandwidth optical connection with a probe for realtime data input, and Ethernet communication with a laptop for simulated and pre-acquired input, and controls of the system. The platform is highly scalable; it can be downscaled for 2D imaging or further upscaled to support higher number of channels on a larger FPGA available on the market. Our imager is self-bootable via a QSPI, is able to output US images on an HDMI screen, and is supported with a GUI that allows the user to control various modes, options, and settings of the system at runtime. This has been successfully achieved through three main phases; (i) algorithmic innovation, development, and investigation on the Matlab framework, (ii) hardware realization of carefully selected algorithms on a Xilinx FPGA, (iii) extensive and intensive assessment for the platform in terms of the resource utilization, reconstruction quality, portability, cost, and even system flexibility and scalability, on both Matlab and Xilinx Vivado.

The main contribution can be summarized as follows:

- A novel delay calculation algorithm has been proposed based on simplifying the massive number of square-root calculations into a far-reduced number of square-root calculations plus additions of two pre-calculated correction coefficients. A detailed assessment for the proposed algorithm has been performed, which also includes the exact calculation algorithm as a golden reference. Accordingly, an efficient FPGA architecture has been designed.
- Three apodization schemes have been developed: the typical model ("expanding-aperture" apodization), a novel apodization scheme (SCA apodization), and a computationally optimized scheme (static apodization model). We have evaluated the two proposed models against the typical one in terms of resource utilization, suppression of

sidelobes, and reduction of the introduced delay-calculation inaccuracy. Accordingly, the static apodization scheme has been selected to be implemented on our single-FPGA digital US imager.

- A smart, telemedicine-suitable, and resource-friendly SC unit has been proposed and realized on our telesonography-capable prototype. It relies on displaying only cross-sections of the reconstructed volume for basic feedback during the acquisition. The block comprises also the implementation of the LC process that compresses the extremely-wide intensity scale of the reconstructed volumes (or images) to a visible range.
- Three common US imaging modes are supported by our US processor: SRI, zone imaging, and compound imaging, allowing the tuning of the imaging quality at the cost of performance and resource consumption.
- Two solutions have been implemented to help the untrained operator on-site labeling the scans before the upload to a hospital for analysis. The first is an automatic location detection facility for the probe using an IMU. The second is a mobile application for probe positioning guidance by providing charts for common US scans, along with guidelines on how to operate the device and perform good scanning practice. They bridge the gap arising from the decoupling of the acquisition from the diagnosis by assisting defining the origin of the captured volumes. This eases the task of the remote US radiologist to achieve the correct diagnosis quickly and effortlessly.
- We have assessed the whole platform from various standpoints: reconstruction quality (quantitatively using PSNR and CR, and qualitatively using PSF and visual assessment), performance, resource utilization (logic, memory, and power), size (i.e. portability), and cost. Further, the platform's scalability has been proven.

We have directed all of these novel contributions to solve the challenges mentioned in Chapter 1 - Section 1.3. The product is a state-of-the-art prototype that can be considered as a major step towards enabling US everywhere and by any personnel. This allows the rendering of the medical US service with all of its incomparable advantages (safety, low cost, non-invasiveness, and versatility) in many situations where the presence of a sonographer is problematic, like in remote rural areas, enclosed spaces (aircrafts, space stations, ships, hyperloops), rescue helicopters and ambulances, and special environments (like battlefields). Our telesonography-capable digital imager - thanks to its compact size, inexpensive cost, and battery power budget - permits the usage of volumetric US in underdeveloped and rural regions where electricity cut-off is an issue and medical equipment budget is limited. Further, this will allow family doctors and general practitioners to carry out US scans, which accordingly enable many related potential societal benefits.

We have released both the feature-rich Matlab-based US processing pipelines - for 2D (linear and phased) and 3D (phased) imaging, and the proposed 2D/3D single-FPGA digital imager design for open access on [124] via:

SSH: [git@github.com:ibrahimaya/ustogo-lsi.git](ssh://git@github.com:ibrahimaya/ustogo-lsi.git)

HTTP: <https://github.com/ibrahimaya/ustogo-lsi.git>

8.1 Future Directions

Although the system is an unprecedented prototype unlocking telemedicine usage scenarios in the US domain, further enhancements and optimizations can still be performed. This includes iterating on the current prototype, optimizing its performance, resource utilization, power consumption, and features, as follows:

- The 32×32 -channel 3D system should be connected to a real matrix probe - whenever available - for realtime data input. This requires higher-bandwidth interfacing between the board and the probe; according to the specifications stated in Table 1.1, 245 Gbps are required, i.e. 16 times the current supported bandwidth, which is calibrated for the 2D 64-channel probe. Our Kintex UltraScale KU040 FPGA supports 20 GTH transceivers, i.e., with a custom-designed board, 20 SFP+ interfaces with a maximum theoretical bandwidth of 16 Gbps, for a raw total of 320 Gbps. Considering the 20% overhead of the Aurora 8b10b protocol, this leaves a net bandwidth of 256 Gbps. Using less-robust Aurora 64b66b encoding with less overhead (3%), 310 Gbps are available. However, the currently used off-the-shelf development board KCU105 gives access to only two QSFP+, i.e. 102.4 Gbps (Aurora 8b10b) or 124.16 Gbps (Aurora 64b66b), while the rest are hardwired to other different interfaces. This will definitely cause a bottleneck on the input side. This limitation is solvable by designing a custom board (i.e. PCB board) around the KU040 FPGA itself, rather than the development board KCU105, exploiting all the QSFP+ provided by the FPGA. Developing such a board will be anyway beneficial for more resource optimization and mass production.
- The *actual* expended power (rather than the pessimistic estimation) by the current prototype should be measured with a dedicated tool like the ones from Maxim [157, 158]. This should include further power optimization for the platform by disabling the unused components.
- The actual rate of the displayed images on the operator-side can be improved by optimizing the writing of the scan-converted frames onto the HDMI port.
- The mobile application can be further developed. A lossless data compression can also be supported for the volumes transfer to a remote hospital.

Chapter 8. Conclusion and Future Directions

More broadly, further research and development can be performed in the following directions:

- Although the main concern of our work is the digital back-end of the US imager, it must be noted that the design of a matching high-channel-count matrix probe that also meets the same stringent objectives of cost, compactness and low-power – also due to thermal limits for patient and operator safety – is still an unmet objective. The LightProbe technology leveraged in this thesis is not directly scalable to high-channel-count 3D, since it is limited by the power dissipation of the AFE – including the ADCs, which are integrated in the probe head. Assuming linear power and size scaling, a matching 1024-channel LightProbe would be unwieldy. Nonetheless, there is reason to pursue this avenue further because (i) the scaling of the front-end should be sub-linear (e.g. the transmit power is constrained by regulations, not channel count; the probe control logic also scales efficiently), (ii) it is known [10] that lower-power components already exist for the realization of LightProbe functions and that technology scaling has a track record of continuous power and integration improvements [159], and finally (iii) if necessary, advanced cooling solutions can also be deployed, such as external housings or liquid cooling in the probe [160–163]. Another partially orthogonal possibility is to combine parts of the algorithms and architectures described in this thesis in combination with other techniques that relax the channel-count/image-quality trade-off (refer to the following bullet).
- Every proposed algorithm in our imaging pipeline can be exploited as it is or in combination with others to reach more efficient computation and enhanced processing. For example, the SHEDA delay-approximation algorithm can be utilized along with other channel-reduction techniques like analog pre-BF [52, 65–70], multiplexing [74, 75], compressive sensing [81–83, 86, 88, 89], RCA [76–80], etc. to achieve more efficient resource utilization while allowing the support of even higher transducer element counts.
- The SCA scheme needs to be further investigated and improved. This includes (i) the automation of the modeling process, (ii) the parameterization of the scheme to make it generic and more adaptable for any probe and reconstruction settings, and (iii) the extensive assessment of the model for various probes, specifications, geometries, and phantoms. Eventually, the scheme can be implemented on hardware.
- Advanced post-processing and image analysis techniques can also be featured on the US radiologist side to allow better diagnosis and measures.
- US volumetric visualization will be extremely advantageous if supported on the hospital side, where there is no limitation on the resources. It should permit user-friendly exploration, navigation and manipulation of volumes allowing the specialist to quickly examine the 3D US scans. This can be achieved with the exploitation of virtual reality devices, like Microsoft kinect 3D scanner [164] that has been used for CT and MRI 3D gesture-control visualization [165, 166]. It will be the first attempt to utilize virtual reality technologies in the medical US field.

Appendices

A SHEDA Error Bound

In this appendix, we discuss the error bound of the first-order Taylor approximation of the calculation of the delay square-roots. Since this approximation is the base of our SHEDA approach, it directly defines the inaccuracy limit of our delay calculation algorithm. Two error bounds have been presented; the typical Lagrange error bound, and our deduced finite error bound. Since, unfortunately, the typical Lagrange bound diverges to infinity when $r \rightarrow 0$ (r is the radial distance of the volume) (Section A.1), we have proposed another approach to bound the first-order-Taylor error. We called this new approach the finite error bound. The detailed mathematical and graphical derivation of the finite error bound is reported in Section A.2.

A.1 Lagrange Error Bound

The error of a Taylor expansion of a function $f(x)$ can be bounded with the Lagrange bound [167, 168]:

$$|E_{f_n}(x)| \leq \frac{M}{(n+1)!} |x-a|^{n+1} \quad (\text{A.1})$$

where E is the error bound, n is the polynomial order, a is the value at which the Taylor polynomial is centered, and M is an upper bound on the absolute value of the $(n+1)$ -th derivative of the original function, in the interval around a in which x varies. We perform the Taylor expansion of two functions, both square roots (Equations (4.3) and (4.4)):

$$h(x) = \sqrt{1+x} = \frac{|\vec{SD}|}{r}, \quad x := \frac{x_D^2 + y_D^2}{r^2} - \frac{2x_D \sin\theta + 2y_D \sin\phi \cos\theta}{r} \quad (\text{A.2})$$

$$h'(x) = \frac{1}{2\sqrt{1+x}} \quad (\text{A.3})$$

Appendix A. SHEDA Error Bound

$$h''(x) = -\frac{1}{4\sqrt{(1+x)^3}} = -\frac{1}{4h^3(x)} = -\frac{r^3}{4|\vec{SD}|^3} \quad (\text{A.4})$$

And

$$g(x) = \sqrt{1+x} = \frac{|\vec{RD}|}{r}, x := \frac{x_D^2 + y_D^2}{r^2} \quad (\text{A.5})$$

$$g'(x) = \frac{1}{2\sqrt{1+x}} \quad (\text{A.6})$$

$$g''(x) = -\frac{1}{4\sqrt{(1+x)^3}} = -\frac{1}{4g^3(x)} = -\frac{r^3}{4|\vec{RD}|^3} \quad (\text{A.7})$$

In our case, $n = 1$ and $a = 0$. We need a bound on M . For M_g , since $|\vec{RD}| \geq r$, immediately:

$$M_g = \max(|g''(x)|) = \frac{1}{4} = 0.25 \quad (\text{A.8})$$

Now for M_h , note that the ratio $\frac{|\vec{SD}|}{r}$ will be smallest for all points at $\pm\theta_{max}, \pm\phi_{max}$, for any r that leaves S just atop D (i.e. $x_D = x_S, y_D = y_S$). For those points and by referring to (4.3) and (4.1) of Chapter 4, the value of $|\vec{SD}|$ equals $z_S = r|\cos\phi_{max}\cos\theta_{max}|$. Therefore, since our image sector is 73° , M_h will be maximum at $|\theta| = |\phi| = 36.5^\circ$ as follows:

$$M_h = \max(|h''|) = \frac{1}{4(|\cos\phi_{max}\cos\theta_{max}|)^3} = 0.9265 \quad (\text{A.9})$$

From (A.1), we can thus now fill in:

$$|E_{g_1}(x)| \leq \frac{M_g}{2}|x|^2 = 0.125 \frac{(x_D^2 + y_D^2)^2}{r^4} \quad (\text{A.10})$$

$$|E_{h_1}(x)| \leq \frac{M_h}{2}|x|^2 = 0.4633 \left(\frac{x_D^2 + y_D^2}{r^2} - \frac{2x_D \sin\theta + 2y_D \sin\phi \cos\theta}{r} \right)^2 \quad (\text{A.11})$$

The total error in path difference (normalized by $\frac{r}{c}$) is thus

$$|E(x)| = |E_1(x)(\vec{SD})| - |E_1(x)(\vec{RD})| \leq$$

$$0.4633 \left(\frac{x_D^2 + y_D^2}{r^2} - \frac{2x_D \sin \theta + 2y_D \sin \phi \cos \theta}{r} \right)^2 - 0.125 \frac{(x_D^2 + y_D^2)^2}{r^4}$$

(A.12)

It should be noted that the total error in (A.12) is the difference of the errors on $h(x)$ and $g(x)$, because $h(x)$, $g(x)$, and their errors are all positive (refer to Figure A.1 that shows that the error is always positive) and their errors must be calculated in the same location x .

The error in time is given by multiplying by r and dividing by c , yielding:

$$|E(x)| \leq \frac{r}{c} \left(0.4633 \left(\frac{x_D^2 + y_D^2}{r^2} - \frac{2x_D \sin \theta + 2y_D \sin \phi \cos \theta}{r} \right)^2 - 0.125 \frac{(x_D^2 + y_D^2)^2}{r^4} \right) =$$

$$\left(0.3383 \frac{(x_D^2 + y_D^2)^2}{cr^3} + 1.8532 \frac{(x_D \sin \theta + y_D \sin \phi \cos \theta)^2}{cr} \right.$$

$$\left. - 1.8532 \frac{(x_D^2 + y_D^2)(x_D \sin \theta + y_D \sin \phi \cos \theta)}{cr^2} \right)$$

(A.13)

Now, we must find the values of x_D , y_D , ϕ , θ , and r that maximize the total error. Obviously, from (A.13) we note that to maximize the total error we should use the minimum possible value of r which is zero. Therefore, the total maximum error using Lagrange bound is infinity. Hence, a different bounding approach is required.

A.2 Finite Error Bound

The relation between the exact function (i.e. $\sqrt{1+x}$) versus its first-order Taylor approximation (i.e. $1 + \frac{1}{2}x$) for $x \geq -1$ is shown in Figure A.1. It is worth noting that as x increases, the difference between the exact function and its approximation increases. Furthermore, the first-order Taylor approximation is always larger than or equal (when $x = 0$) to the exact function. Therefore, we can represent the error bound by only the approximation function.

As mentioned previously, we have approximated two functions where x is

$$x_h = \frac{x_D^2 + y_D^2}{r^2} - \frac{2x_D \sin \theta + 2y_D \sin \phi \cos \theta}{r},$$

(A.14)

Appendix A. SHEDA Error Bound

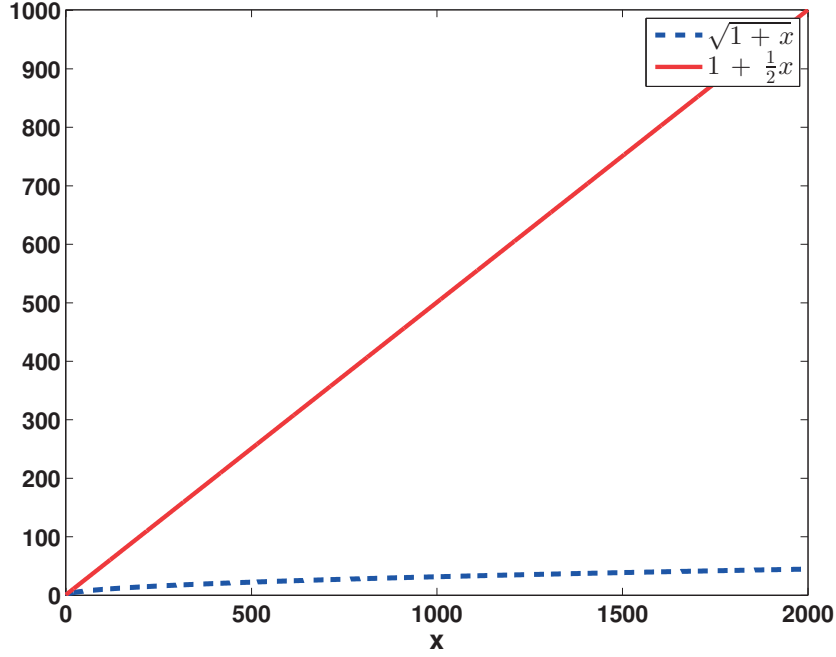


Figure A.1: The plot of the exact function $\sqrt{1+x}$ (dashed blue) and its first-order Taylor approximation $1 + \frac{1}{2}x$ (solid red) for $x \geq -1$.

$$x_g = \frac{x_D^2 + y_D^2}{r^2} \quad (\text{A.15})$$

Hence, the errors for each of those approximations are

$$|E_{h1}(x)| \leq 1 + \frac{1}{2}x_h, \quad |E_{g1}(x)| \leq 1 + \frac{1}{2}x_g. \quad (\text{A.16})$$

Again, the total error should be the absolute value of the difference of those two errors, yielding:

$$|E(x)| \leq ||E_{h1}(x)| - |E_{g1}(x)|| = |(1 + \frac{1}{2}x_h) - (1 + \frac{1}{2}x_g)| = \frac{1}{2}|(x_h - x_g)| \quad (\text{A.17})$$

By substituting by x_h and x_g ,

$$|E(x)| \leq \left| \frac{x_D \sin \theta + y_D \sin \phi \cos \theta}{r} \right|. \quad (\text{A.18})$$

The error in path difference expressed in time is given by multiplying by r over c :

$$|E(x)| \leq \left| \frac{x_D \sin\theta + y_D \sin\phi \cos\theta}{c} \right| \quad (\text{A.19})$$

To get the maximum error, we use the maximum values of x_D and y_D (i.e. x_{Dmax} and y_{Dmax}), since the relation between the error and x_D and y_D is linear. Therefore and according to our assumption that the probe is square (i.e. the transducer width = transducer height = $19.06mm$), the error will be maximum at $x_D = y_D = 9.53mm$. In addition, the ϕ and θ values that maximize the error could be obtained by plotting $\sin\theta + \sin\phi \cos\theta$ versus θ and ϕ (see Figure A.2) where the maximum values are obtained at $|\phi| = |\theta| = \theta_{max} = \phi_{max} = 36.5^\circ$. It should be noted that we can get the same maximum value for the total error by choosing the two numerator terms to be negative. An example of that choice is to use $x_D = -x_{Dmax}$, $y_D = y_{Dmax}$, $\phi = -36.5^\circ$, and $\theta = 36.5^\circ$. Hence, the two terms in the numerator of (A.19) will be added with negative signs, but the absolute operator will yield the same outcome.

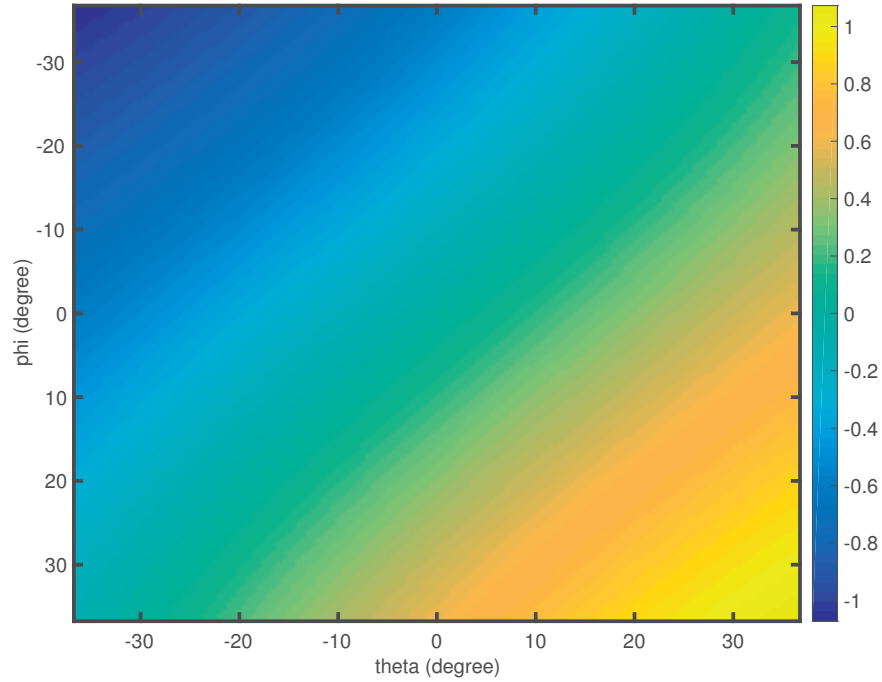


Figure A.2: The plot of the $\sin\theta + \sin\phi \cos\theta$ function versus θ and ϕ .

The final outcome is:

$$|E| = \frac{0.0102254}{1540} = 6.64\mu sec, \quad (\text{A.20})$$

Appendix A. SHEDA Error Bound

which at the target sampling frequency of 32 MHz, equals 213 signal samples. Obviously this bound is decidedly unacceptable; however, this occurs in areas very close to the transducer or at broad angles, which are least critical for image quality and anyway mitigated by apodization pruning (Section 5.1). A Matlab numerical exploration is performed in the volume of interest, and the maximum absolute error we observed after considering the typical dynamic apodization was 99 signal samples (Section 5.1).

B SCA Mathematical Model

In this appendix, the mathematical model of the SCA scheme (Section 5.1.1) is documented. We have modeled the SCA to account for the inaccuracies introduced by our SHEDA algorithm (Chapter 4). This has been performed while maintaining the typical purpose of any apodization function of minimizing the side-lobes resulting from the antenna-like characteristic of the US piezoelectric elements.

The SCA scheme is described by the window width W , height H , and center (x_c and y_c) for different volume locations (r , θ , and ϕ). The mathematical model is defined in terms of the radial distance r , the azimuth angle θ , and the elevation angle ϕ of the volume.

Equations (B.1) and (B.2) express the width W and the height H , respectively, as a function of r, θ, ϕ , as follows:

$$W(r, \phi, \theta) = \begin{cases} \frac{3r}{28} + 4, & (1 \leq r < 140) \\ 0.4 \times \left(\frac{13r}{140} - \frac{\theta' + 37}{3.5} + \frac{\phi' + 37}{3.5} + 13 \right), & (140 \leq r < 1500) \wedge (-36^\circ \leq \theta \leq -19^\circ) \wedge (-36^\circ \leq \phi \leq -19^\circ) \\ a \times \left(\frac{13r}{140} + \frac{\theta' + 37}{3.5} + \frac{\phi' + 37}{3.5} \right), & (140 \leq r < 1500) \wedge (-18^\circ \leq \theta \leq 0^\circ) \wedge (-36^\circ \leq \phi \leq -19^\circ) \\ \frac{13r}{140} - \frac{\theta' + 37}{3.5} - \frac{\phi' + 37}{3.5} + 19, & (140 \leq r < 1500) \wedge (-36^\circ \leq \theta \leq -19^\circ) \wedge (-18^\circ \leq \phi \leq 0^\circ) \\ b \times 0.6 \times \left(\frac{13r}{140} + \frac{\theta' + 37}{3.5} - \frac{\phi' + 37}{3.5} + 33 \right), & (140 \leq r < 1500) \wedge (-18^\circ \leq \theta \leq 0^\circ) \wedge (-18^\circ \leq \phi \leq 0^\circ), \\ & \text{Except } \phi = \theta = 0^\circ \\ 100 - \frac{\theta' + 37}{3.5} + \frac{\phi' + 37}{3.5} + 13, & (1500 \leq r < 5000) \wedge (-36^\circ \leq \theta \leq -19^\circ) \wedge (-36^\circ \leq \phi \leq -19^\circ) \\ 100 + \frac{\theta' + 37}{3.5} + \frac{\phi' + 37}{3.5}, & (1500 \leq r < 5000) \wedge (-18^\circ \leq \theta \leq 0^\circ) \wedge (-36^\circ \leq \phi \leq -32^\circ) \\ 100 - \frac{\theta' + 37}{3.5} - \frac{\phi' + 37}{3.5} + 19, & (1500 \leq r < 5000) \wedge (-36^\circ \leq \theta \leq -32^\circ) \wedge (-18^\circ \leq \phi \leq 0^\circ) \\ \text{Expanding aperture}, & (\theta = \phi = 0^\circ) \vee ((1500 \leq r < 5000) \wedge (-31^\circ \leq \theta \leq 0^\circ) \wedge (-31^\circ \leq \phi \leq 0^\circ)) \\ 100, & r \geq 5000 \end{cases} \quad (\text{B.1})$$

Appendix B. SCA Mathematical Model

$$H(r, \phi, \theta) = \begin{cases} \frac{3r}{28} + 4, & (1 \leq r < 140) \\ 0.4 \times (\frac{13r}{140} + \frac{\theta' + 37}{3.5} - \frac{\phi' + 37}{3.5} + 13), & (140 \leq r < 1500) \wedge (-36^\circ \leq \theta \leq -19^\circ) \wedge (-36^\circ \leq \phi \leq -19^\circ) \\ a \times (\frac{13r}{140} - \frac{\theta' + 37}{3.5} - \frac{\phi' + 37}{3.5} + 19), & (140 \leq r < 1500) \wedge (-18^\circ \leq \theta \leq 0^\circ) \wedge (-36^\circ \leq \phi \leq -19^\circ) \\ \frac{13r}{140} + \frac{\theta' + 37}{3.5} + \frac{\phi' + 37}{3.5}, & (140 \leq r < 1500) \wedge (-36^\circ \leq \theta \leq -19^\circ) \wedge (-18^\circ \leq \phi \leq 0^\circ) \\ b \times 0.6 \times (\frac{13r}{140} - \frac{\theta' + 37}{3.5} + \frac{\phi' + 37}{3.5} + 33), & (140 \leq r < 1500) \wedge (-18^\circ \leq \theta \leq 0^\circ) \wedge (-18^\circ \leq \phi \leq 0^\circ), \text{Except } \phi = \theta = 0^\circ \\ 100 + \frac{\theta' + 37}{3.5} - \frac{\phi' + 37}{3.5} + 13, & (1500 \leq r < 5000) \wedge (-36^\circ \leq \theta \leq -19^\circ) \wedge (-36^\circ \leq \phi \leq -19^\circ) \\ 100 - \frac{\theta' + 37}{3.5} - \frac{\phi' + 37}{3.5} + 19, & (1500 \leq r < 5000) \wedge (-18^\circ \leq \theta \leq 0^\circ) \wedge (-36^\circ \leq \phi \leq -32^\circ) \\ 100 + \frac{\theta' + 37}{3.5} + \frac{\phi' + 37}{3.5}, & (1500 \leq r < 5000) \wedge (-36^\circ \leq \theta \leq -32^\circ) \wedge (-18^\circ \leq \phi \leq 0^\circ) \\ \text{Expanding aperture}, & (\theta = \phi = 0^\circ) \vee ((1500 \leq r < 5000) \wedge (-31^\circ \leq \theta \leq 0^\circ) \wedge (-31^\circ \leq \phi \leq 0^\circ)) \\ 100, & r \geq 5000 \end{cases} \quad (\text{B.2})$$

where a and b are evaluated by the following definitions:

$$a = \begin{cases} 0.7, & ((r < 415) \wedge (-18^\circ \leq \theta \leq 0^\circ) \wedge (-36^\circ \leq \phi \leq -29^\circ)) \vee ((140 \leq r < 1500) \wedge (-18^\circ \leq \theta \leq 0^\circ) \wedge (-28^\circ \leq \phi \leq -19^\circ)) \\ 0.5, & (415 \leq r < 1500) \wedge (-18^\circ \leq \theta \leq 0^\circ) \wedge (-36^\circ \leq \phi \leq -29^\circ) \end{cases} \quad (\text{B.3})$$

$$b = \begin{cases} 0.7, & ((r < 415) \wedge (-36^\circ \leq \theta \leq -29^\circ) \wedge (-18^\circ \leq \phi \leq 0^\circ)) \vee ((140 \leq r < 1500) \wedge (-28^\circ \leq \theta \leq -19^\circ) \wedge (-18^\circ \leq \phi \leq 0^\circ)) \\ 0.5, & (415 \leq r < 1500) \wedge (-36^\circ \leq \theta \leq -29^\circ) \wedge (-18^\circ \leq \phi \leq 0^\circ) \end{cases} \quad (\text{B.4})$$

On the other hand, x_c is described in Equation (B.5) as a function of r and θ , and y_c is represented by Equation (B.6) as a function of r and ϕ .

$$x_c(r, \theta) = \begin{cases} 51, & (1 \leq r < 140) \vee ((140 \leq r < 1500) \wedge (-3^\circ \leq \theta \leq 0^\circ)) \vee \\ & ((1500 \leq r < 5000) \wedge (-31^\circ \leq \theta \leq 0^\circ) \wedge (-31^\circ \leq \phi \leq 0^\circ)) \vee (r \geq 5000) \\ 49 - \frac{3r}{420} + \frac{\theta' + 37}{10.5}, & (140 \leq r < 1500) \wedge (-36^\circ \leq \theta \leq -4^\circ) \vee ((1500 \leq r < 5000) \wedge (-36^\circ \leq \theta \leq -32^\circ)) \end{cases} \quad (\text{B.5})$$

$$y_c(r, \phi) = \begin{cases} 51, & (1 \leq r < 140) \vee ((140 \leq r < 1500) \wedge (-3^\circ \leq \phi \leq 0^\circ)) \vee \\ & ((1500 \leq r < 5000) \wedge (-31^\circ \leq \theta \leq 0^\circ) \wedge (-31^\circ \leq \phi \leq 0^\circ)) \vee (r \geq 5000) \\ 49 - \frac{3r}{420} + \frac{\phi' + 37}{10.5}, & (140 \leq r < 1500) \wedge (-36^\circ \leq \phi \leq -4^\circ) \vee ((1500 \leq r < 5000) \wedge (-36^\circ \leq \phi \leq -32^\circ)) \end{cases} \quad (\text{B.6})$$

The angle variables θ and ϕ are in degrees and the r variable is in periods of sampling fre-

quency. The W and H equations hold in one quarter of the volume, while the center x_c and y_c equations hold in one half of the volume. They are replicated symmetrically in θ and ϕ , while considering that $\theta' = \theta$ and $\phi' = \phi$ if $\theta \leq 0^\circ$ and $\phi \leq 0^\circ$, respectively, and $\theta' = -\theta$ and $\phi' = -\phi$ if $\theta > 0^\circ$ and $\phi > 0^\circ$, respectively.

Our methodology of designing the SCA model, and its detailed quality and resource utilization evaluation, are discussed in Section 5.1.1.

Bibliography

- [1] Business Wire, Inc., “Samsung’s ws80a with elite ultrasound system and ceretom®-equipped mobile stroke unit featured at premier, inc. annual breakthroughs conference and exhibition,” 2018, [Online]. Available: <https://www.businesswire.com/news/home/20160622006398/en/Samsung%E2%80%9999s-WS80A-Elite-Ultrasound-System-CereTom%C2%AE-Equipped-Mobile>.
- [2] “EPIQ 7 ultrasound system,” Philips Healthcare, 2018, [Online]. Available: <http://www.medical.philips.com/main/products/ultrasound/systems/epiq7/>.
- [3] GE Healthcare, “Voluson E10,” 2017, [Online]. Available: www.gehealthcare.com.
- [4] “Real time 3D (RT3D) ultrasound,” George Stetten, [Online]. Available: <http://www.stetten.com/george/rt3d/>.
- [5] Koninklijke Philips N.V., “Ultrasound transducers,” 2018, [Online]. Available: http://www.healthcare.philips.com/main/products/ultrasound/transducers/open_article_index.wpd.
- [6] J. L. H. French, N. J. Raine-Fenning, J. G. Hardman, and N. M. Bedford, “Pitfalls of ultrasound guided vascular access: the use of three/four-dimensional ultrasound,” *Anaesthesia*, vol. 63, no. 8, pp. 806–813, 2008, [Online]. Available: <https://onlinelibrary.wiley.com/doi/abs/10.1111/j.1365-2044.2008.05513.x>.
- [7] “Field ii simulation program: Calculation of b-mode image of synthetic kidney,” Field II, April 2012, [Online]. Available: http://field-ii.dk/?examples/kidney_example/kidney_example.html.
- [8] “Field ii simulation program: Calculation of b-mode image of synthetic fetus,” Field II, April 2012, [Online]. Available: http://field-ii.dk/?examples/fetus_example/fetus_example.html.
- [9] A. Ibrahim, P. A. Hager, A. Bartolini, F. Angiolini, M. Arditi, J.-P. Thiran, L. Benini, and G. De Micheli, “Efficient sample delay calculation for 2d and 3d ultrasound imaging,” *IEEE Transactions on Biomedical Circuits and Systems (TBCAS)*, vol. 11, no. 4, pp. 815–831, Aug 2017.

Bibliography

- [10] P. A. Hager, C. Risser, P.-K. Weber, and L. Benini, "LightProbe: a 64-channel programmable ultrasound transducer head with an integrated front-end and a 26.4 Gb/s optical link," in *Proceedings of the 2017 IEEE International Symposium on Circuits and Systems (ISCAS 2017)*, 2017.
- [11] Daylite Designs, "Body diagram for professional massage chart: front, back, left and right views," [Online]. Available: <https://en.99designs.ch/icon-button-design/contests/body-diagram-professional-massage-chart-front-back-left-210696>.
- [12] L. Nouaille, N. Smith-Guérin, G. Poisson, and P. Arbeille, "Optimization of a 4 dof tele-echography robot," in *Intelligent Robots and Systems (IROS), 2010 IEEE/RSJ International Conference on*. IEEE, 2010, pp. 3501–3506.
- [13] B. I. Lessard S, Bigras P, "A new medical parallel robot and its static balancing optimization," *Journal of Medical Devices*, vol. 1, no. 4, pp. 272–278, 2007.
- [14] M. Rueda, C. Riga, and M. Hamady, "Robotics in interventional radiology: Past, present, and future," *The Arab Journal of Interventional Radiology*, vol. 2, no. 2, pp. 56–63, 2018.
- [15] "Long-distance ultrasound: Made for astronauts, now reaching hospitals," The European Space Agency (ESA), 2016, [Online]. Available: http://www.esa.int/Our_Activities/Space_Engineering_Technology/Long-distance_ultrasound_made_for_astronauts_now_reaching_hospitals.
- [16] P. Vieyres, G. Poisson, F. Courreges, O. Merigeaux, and P. Arbeille, "The TERESA project: from space research to ground tele-echography," *Industrial Robot: An International Journal*, vol. 30, no. 1, pp. 77–82, 2003.
- [17] K. Mathiassen, J. E. Fjellin, K. Glette, P. K. Hol, and O. J. Elle, "An ultrasound robotic system using the commercial robot UR5," *Frontiers in Robotics and AI*, vol. 3, p. 1, 2016, [Online]. Available: <https://www.frontiersin.org/article/10.3389/frobt.2016.00001>.
- [18] "HD15 purewave ultrasound system," Philips Healthcare, 2018, [Online]. Available: <https://www.philips.ca/healthcare/product/HC795066/hd15-ultrasound-system>.
- [19] Samsung Electronics Co., Ltd., "Samsung WS80A with elite," 2018, [Online]. Available: <http://www.samsung.com/global/business/healthcare/healthcare/ultrasound/USS-WS8AF4K/WR>.
- [20] "Butterfly iq," Butterfly Network Inc., 2018, [Online]. Available: <https://www.butterflynetwork.com/index.html>.
- [21] "Lumify," Philips Healthcare, 2018, [Online]. Available: <https://www.lumify.philips.com/web/>.
- [22] "Clarius: Handheld wireless ultrasound scanner," Clarius Mobile Health, 2018, [Online]. Available: <https://www.clarius.me/products/>.

-
- [23] “Sonosite,” FujiFilm SonoSite Inc., 2018, [Online]. Available: <https://www.sonosite.com/>.
- [24] “Vscan portfolio,” GE Healthcare, 2017, [Online]. Available: http://www3.gehealthcare.com/en/products/categories/ultrasound/vscan_portfolio.
- [25] “Sonic window,” BK Ultrasound, 2016, [Online]. Available: <http://bkultrasound.com/products/sonic-window-handheld-ultrasound>.
- [26] “Sonix tablet,” BK Ultrasound, 2016, [Online]. Available: <http://bkultrasound.com/products/sonix/systems/sonixtabletq-ultrasound-system>.
- [27] G. Healthcare, “Vivid i,” 2018, [Online]. Available: http://www3.gehealthcare.com.sg/en-gb/products/categories/ultrasound/vivid/vivid_i.
- [28] MobiSante, “Mobisante ultrasound,” 2017, [Online]. Available: <http://www.mobisante.com/>.
- [29] H. Hewener and S. Tretbar, “Mobile ultrafast ultrasound imaging system based on smartphone and tablet devices,” in *2015 IEEE International Ultrasonics Symposium (IUS 2015)*, Nov 2015.
- [30] J. Kang, C. Yoon, J. Lee, S.-B. Kye, Y. Lee, J. H. Chang, Gi-DuckKim, YangmoYoo, and T. kyong Song, “A system-on-chip solution for point-of-care ultrasound imaging systems: Architecture and ASIC implementation,” *IEEE Transactions on Biomedical Circuits and Systems*, vol. 10, no. 2, pp. 412 – 423, April 2016.
- [31] U. Bencharit, J. L. Kaufman, N. M. Bilgutay, and J. Saniie, “Frequency and spatial compounding techniques for improved ultrasonic imaging,” in *IEEE 1986 Ultrasonics Symposium*, Nov 1986, pp. 1021–1026.
- [32] Xilinx Inc., “Ultrascale FPGA: Product tables and product selection guide,” 2016, [Online]. Available: <http://www.xilinx.com/support/documentation/selection-guides/ultrascale-fpga-product-selection-guide.pdf#KU>.
- [33] C. Sumi and S. Uga, “Effective ultrasonic virtual sources which can be positioned independently of physical aperture focus positions,” *Reports in Medical Imaging*, 2010.
- [34] B. Steinberg, “Digital beamforming in ultrasound,” *Ultrasonics, Ferroelectrics, and Frequency Control, IEEE Transactions on*, vol. 39, no. 6, pp. 716–721, Nov. 1992.
- [35] E. A. Howard, M. Brandestini, J. Powers, S. Taheri, M. E. Eyer, D. J. Phillips, and E. B. Weiler, *Combined Two-Dimensional Tissue/Flow Imaging*. Boston, MA: Springer US, 1980, pp. 533–544.
- [36] J. E. Powers, D. J. Phillips, M. A. Brandestini, and R. A. Sigelmann, “Ultrasound phased array delay lines based on quadrature sampling techniques,” *IEEE Transactions on Sonics and Ultrasonics*, vol. 27, no. 6, pp. 287–294, Nov 1980.

Bibliography

- [37] E. Kaleva, J. Toyras, J. S. Jurvelin, T. Viren, and S. Saarakkala, "Effects of ultrasound frequency, temporal sampling frequency, and spatial sampling step on the quantitative ultrasound parameters of articular cartilage," *IEEE Transactions on Ultrasonics, Ferroelectrics, and Frequency Control*, vol. 56, no. 7, pp. 1383–1393, July 2009.
- [38] K. Thomenius, "Evolution of ultrasound beamformers," in *Ultrasonics Symposium, 1996. Proceedings., 1996 IEEE*, vol. 2, Nov 1996, pp. 1615–1622 vol.2.
- [39] J. A. Jensen, "Ultrasound imaging and its modeling," in *Imaging of Complex Media with Acoustic and Seismic Waves. Topics in Applied Physics*, M. Fink, W. A. Kuperman, J.-P. Montagner, and A. Tourin, Eds. Heidelberg: Springer, Berlin, 2002, vol. 84, pp. 135–166.
- [40] T. L. Szabo, "Chapter 6 - beamforming," in *Diagnostic Ultrasound Imaging: Inside Out (Second Edition)*, 2nd ed., T. L. Szabo, Ed. Boston: Academic Press, 2014, pp. 167 – 207, [Online]. Available: <http://www.sciencedirect.com/science/article/pii/B9780123964878000069>.
- [41] P. 't Hoen, "Aperture apodization to reduce the off-axis intensity of the pulsed-mode directivity function of linear arrays," *Ultrasonics*, vol. 20, no. 5, pp. 231 – 236, September 1982.
- [42] C. Daft and W. Engeler, "Windowing of wide-band ultrasound transducers," in *Ultrasonics Symposium, 1996. Proceedings., 1996 IEEE*, vol. 2. IEEE, 1996, pp. 1541–1544.
- [43] S.-T. Lin and J. P. Scheib, "Direct demodulation in ultrasound instruments," Jan. 14 1992, US Patent 5482044A.
- [44] J. H. Chang, J. T. Yen, and K. K. Shung, "A novel envelope detector for high-frame rate, high-frequency ultrasound imaging," *IEEE Transactions on Ultrasonics, Ferroelectrics, and Frequency Control*, vol. 54, no. 9, pp. 1792–1801, September 2007.
- [45] M. Ali, D. Magee, and U. Dasgupta, "Signal processing overview of ultrasound systems for medical imaging," *Texas Instruments, White Paper*, 2008, [Online]. Available: <http://k-space.org/ymk/sprab12.pdf>.
- [46] K. MacCallum, "Pros and cons of two popular ultrasound signal processing techniques," 2018, [Online]. Available: <https://starfishmedical.com/2015/02/19/pros-cons-two-popular-ultrasound-signal-processing-techniques/>.
- [47] J. Kirkhorn, "Introduction to iq-demodulation of rf-data," 1999, [Online]. Available: <http://folk.ntnu.no/htorp/Undervisning/TTK10/IQdemodulation.pdf>.
- [48] H. Zhou and Y.-f. Zheng, "An efficient quadrature demodulator for medical ultrasound imaging," *Frontiers of Information Technology & Electronic Engineering*, vol. 16, no. 4, pp. 301–310, April 2015, [Online]. Available: <https://doi.org/10.1631/FITEE.1400205>.

-
- [49] J.-Y. Lu, "Experimental study of high frame rate imaging with limited diffraction beams," *Ultrasonics, Ferroelectrics, and Frequency Control, IEEE Transactions on*, vol. 45, no. 1, pp. 84–97, Jan 1998.
- [50] M. Tanter and M. Fink, "Ultrafast imaging in biomedical ultrasound," *IEEE Trans. Ultrason., Ferroelectr., Freq. Control.*, vol. 61, no. 1, pp. 102–119, January 2014.
- [51] T. G. Bjåstad, "High frame rate ultrasound imaging using parallel beamforming," *NTNU PhD Dissertation*, 2009.
- [52] K. Üstüner, "High information rate volumetric ultrasound imaging," *Siemens Healthcare sector, White paper*, 2008.
- [53] J. A. Jensen, S. I. Nikolov, K. L. Gammelmark, and M. H. Pedersen, "Synthetic aperture ultrasound imaging," *Ultrasonics*, vol. 44, Supplement, no. 0, pp. e5 – e15, 2006, proceedings of Ultrasonics International (UI05) and World Congress on Ultrasonics (WCU).
- [54] D. Napolitano, B. DeBusschere, G. McLaughlin, L. Mo, C. Chou, T. Ji, and R. Steins, "Continuous transmit focusing method and apparatus for ultrasound imaging system," Aug. 23 2011, US Patent 8,002,705.
- [55] G. McLaughlin, "Zone sonography®: What it is and how it's different," ZONARE Medical Systems, Inc., Tech. Rep., 2012, [Online]. Available: www.gehealthcare.com.
- [56] T. Jedrzejewicz, D. Napolitano, D. DeBusschere, C.-H. Chou, and G. McLaughlin, "Two-way continuous transmit and receive focusing in ultrasound imaging," ZONARE Medical Systems, Inc., Tech. Rep., 2013, [Online]. Available: http://res.mindray.com/Documents/2016-12-14/d2dd8ebd-a052-482a-8541-b8de227d4ee6/K90127_two_way_transmit_receive.pdf.
- [57] G. Montaldo, M. Tanter, J. Bercoff, N. Benech, and M. Fink, "Coherent plane-wave compounding for very high frame rate ultrasonography and transient elastography," *IEEE Trans. Ultrason., Ferroelectr., Freq. Control.*, vol. 56, no. 3, pp. 489–506, March 2009.
- [58] V. Chan and A. Perlas, "Basics of ultrasound imaging," in *Atlas of Ultrasound-Guided Procedures in Interventional Pain Management*, S. N. Narouze, Ed. New York: Springer-Verlag, 2011, ch. 2, pp. 13–19.
- [59] M. A. Averkiou, D. N. Roundhill, and J. E. Powers, "A new imaging technique based on the nonlinear properties of tissues," in *1997 IEEE Ultrasonics Symposium Proceedings. An International Symposium (Cat. No.97CH36118)*, vol. 2, Oct 1997, pp. 1561–1566 vol.2.
- [60] T. Uppal, "Tissue harmonic imaging 13.2 pmc. may 2018." *Australasian Journal of Ultrasound in Medicine*, vol. 13, no. 2, pp. 29 – 31, 2010.
- [61] A. Anvari, F. Forsberg, and A. E. Samir, "A primer on the physical principles of tissue harmonic imaging," *RadioGraphics*, vol. 35, no. 7, pp. 1955–1964, 2015, PMID: 26562232.

Bibliography

- [62] I. Trots, A. Nowicki, M. Lewandowski, and Y. Tasinkevych, "Synthetic aperture method in ultrasound imaging," in *Ultrasound Imaging*, M. Tanabe, Ed. Rijeka: InTech, 2011, ch. 3, [Online]. Available: <https://doi.org/10.5772/15986>.
- [63] J. Kortbek, J. A. Jensen, and K. L. Gammelmark, "Sequential beamforming for synthetic aperture imaging," *Ultrasonics*, vol. 53, no. 1, pp. 1 – 16, 2013.
- [64] J. T. Ylitalo and H. Ermert, "Ultrasound synthetic aperture imaging: monostatic approach," *IEEE Transactions on Ultrasonics, Ferroelectrics, and Frequency Control*, vol. 41, no. 3, pp. 333–339, May 1994.
- [65] J. Larson, "2-d phased array ultrasound imaging system with distributed phasing," Jul. 20 1993, uS Patent 5,229,933.
- [66] B. Savord and R. Solomon, "Fully sampled matrix transducer for real time 3D ultrasonic imaging," in *Ultrasonics, 2003 IEEE Symposium on*, vol. 1. IEEE, 2003, pp. 945–953.
- [67] J.-Y. Um, Y.-J. Kim, S.-E. Cho, M.-K. Chae, B. Kim, J.-Y. Sim, and H.-J. Park, "A single-chip 32-channel analog beamformer with 4-ns delay resolution and 768-ns maximum delay range for ultrasound medical imaging with a linear array transducer," *IEEE Transactions on Biomedical Circuits and Systems*, vol. 9, no. 1, pp. 138 – 151, February 2015.
- [68] G. Frey and R. Chiao, "4Z1c real-time volume imaging transducer," *Siemens Healthcare Sector, White Paper*, 2008.
- [69] H. g. Kang, S. Bae, P. Kim, J. Park, G. Lee, W. Jung, M. Park, K. Kim, W. Lee, and T. K. Song, "Column-based micro-beamformer for improved 2D beamforming using a matrix array transducer," in *Proceedings of the 2015 Biomedical Circuits And Systems (BioCAS) Conference*, 2015.
- [70] J. Um, Y. Kim, S. Cho, M. Chae, J. Song, B. Kim, S. Lee, J. Bang, Y. Kim, K. Cho, B. Kim, J. Sim, and H. Park, "An analog-digital hybrid RX beamformer chip with non-uniform sampling for ultrasound medical imaging with 2D CMUT array," *IEEE Transactions on Biomedical Circuits and Systems*, vol. 8, no. 6, December 2014.
- [71] A. Austeng and S. Holm, "Sparse 2-d arrays for 3-d phased array imaging - design methods," *IEEE Trans. Ultrason., Ferroelectr., Freq. Control.*, vol. 49, no. 8, pp. 1073–1086, Aug 2002.
- [72] J. T. Yen, J. P. Steinberg, and S. W. Smith, "Sparse 2-D array design for real time rectilinear volumetric imaging," *IEEE Trans. Ultrason., Ferroelectr., Freq. Control.*, vol. 47, no. 1, pp. 93–110, Jan 2000.
- [73] J. Zhou, S. Wei, R. Sampson, R. Jintamethasawat, O. D. Kripfgans, J. B. Fowlkes, T. F. Wenisch, and C. Chakrabarti, "High volume rate 3d ultrasound imaging based on synthetic aperture sequential beamforming," in *2017 IEEE International Ultrasonics Symposium (IUS)*, Sept 2017, pp. 1–4.

-
- [74] T. M. Carpenter, M. W. Rashid, M. Ghovanloo, D. Cowell, S. Freear, and F. L. Degertekin, "Time-division multiplexing for cable reduction in ultrasound imaging catheters," in *Proceedings of the 2015 Biomedical Circuits And Systems (BioCAS) Conference*, 2015.
- [75] J. T. Yen and S. W. Smith, "Real-time rectilinear 3-d ultrasound using receive mode multiplexing," *IEEE Trans. Ultrason., Ferroelectr., Freq. Control.*, vol. 51, no. 2, pp. 216–226, Feb 2004.
- [76] C. H. Seo and J. T. Yen, "A 256 x 256 2-d array transducer with row-column addressing for 3-d rectilinear imaging," *IEEE Trans. Ultrason., Ferroelectr., Freq. Control.*, vol. 56, no. 4, pp. 837–847, April 2009.
- [77] C. E. M. Demore, A. W. Joyce, K. Wall, and G. R. Lockwood, "Real-time volume imaging using a crossed electrode array," *IEEE Trans. Ultrason., Ferroelectr., Freq. Control.*, vol. 56, no. 6, pp. 1252–1261, June 2009.
- [78] C. Ceroici, T. Harrison, and R. J. Zemp, "Fast orthogonal row-column electronic scanning with top-orthogonal-to-bottom electrode arrays," *IEEE Trans. Ultrason., Ferroelectr., Freq. Control.*, vol. 64, no. 6, pp. 1009–1014, June 2017.
- [79] H. Bouzari, M. Engholm, M. B. Stuart, E. V. Thomsen, and J. A. Jensen, "Improved focusing method for 3-d imaging using row-column-addressed 2-d arrays," in *2017 IEEE International Ultrasonics Symposium (IUS)*, Sept 2017, pp. 1–4.
- [80] H. Bouzari, M. Engholm, C. Beers, M. B. Stuart, S. I. Nikolov, E. V. Thomsen, and J. A. Jensen, "3-d imaging using row-column-addressed 2-d arrays with a diverging lens: Phantom study," in *2017 IEEE International Ultrasonics Symposium (IUS)*, Sept 2017, pp. 1–4.
- [81] N. Wagner, Y. C. Eldar, and Z. Friedman, "Compressed beamforming in ultrasound imaging," *IEEE Transactions on Signal Processing*, vol. 60, no. 9, pp. 4643–4657, Sept 2012.
- [82] H. Liebgott, A. Basarab, D. Kouame, O. Bernard, and D. Friboulet, "Compressive sensing in medical ultrasound," in *2012 IEEE International Ultrasonics Symposium*, Oct 2012, pp. 1–6.
- [83] R. E. Carrillo, J. D. McEwen, D. V. D. Ville, J. P. Thiran, and Y. Wiaux, "Sparsity averaging for compressive imaging," *IEEE Signal Processing Letters*, vol. 20, no. 6, pp. 591–594, June 2013.
- [84] C. Quinsac, A. Basarab, D. Kouamé, and J. M. Grégoire, "3d compressed sensing ultrasound imaging," in *2010 IEEE International Ultrasonics Symposium*, Oct 2010, pp. 363–366.
- [85] O. Lorintiu, H. Liebgott, M. Alessandrini, O. Bernard, and D. Friboulet, "Compressed sensing reconstruction of 3d ultrasound data using dictionary learning," in *2014 IEEE International Conference on Image Processing (ICIP)*, Oct 2014, pp. 1317–1321.

Bibliography

- [86] —, “Compressed sensing reconstruction of 3d ultrasound data using dictionary learning and line-wise subsampling,” *IEEE Transactions on Medical Imaging*, vol. 34, no. 12, pp. 2467–2477, Dec 2015.
- [87] A. Besson, R. E. Carrillo, O. Bernard, Y. Wiaux, and J. P. Thiran, “Compressed delay-and-sum beamforming for ultrafast ultrasound imaging,” in *2016 IEEE International Conference on Image Processing (ICIP)*, Sept 2016, pp. 2509–2513.
- [88] A. Besson, D. Perdios, F. Martinez, Z. Chen, R. E. Carrillo, M. Arditi, Y. Wiaux, and J. P. Thiran, “Ultrafast ultrasound imaging as an inverse problem: Matrix-free sparse image reconstruction,” *IEEE Transactions on Ultrasonics, Ferroelectrics, and Frequency Control*, vol. 65, no. 3, pp. 339–355, March 2018.
- [89] A. Burshtein, M. Birk, T. Chernyakova, A. Eilam, A. Kempinski, and Y. C. Eldar, “Subnyquist sampling and fourier domain beamforming in volumetric ultrasound imaging,” *IEEE Transactions on Ultrasonics, Ferroelectrics, and Frequency Control*, vol. 63, no. 5, pp. 703–716, May 2016.
- [90] S. I. Nikolov, J. A. Jensen, and B. Tomov, “Recursive delay calculation unit for parametric beamformer,” in *Medical Imaging. International Society for Optics and Photonics*, 2006, pp. 61 470D–61 470D.
- [91] J. Jensen, H. Holten-Lund, R. Nilsson, M. Hansen, U. Larsen, R. Domsten, B. Tomov, M. Stuart, S. Nikolov, M. Pihl, Y. Du, J. Rasmussen, and M. Rasmussen, “Sarus: A synthetic aperture real-time ultrasound system,” *IEEE Trans. Ultrason., Ferroelectr., Freq. Control.*, vol. 60, no. 9, pp. 1838–1852, Sep 2013.
- [92] P. Vogel, A. Bartolini, and L. Benini, “Efficient parallel beamforming for 3D ultrasound imaging,” in *Proceedings of the 24th Edition of the Great Lakes Symposium on VLSI*, ser. GLSVLSI ’14. New York, NY, USA: ACM, 2014, pp. 175–180, [Online]. Available: <http://doi.acm.org/10.1145/2591513.2591599>.
- [93] Cephasonics, “Receive RX Beamformer, CSC2032,” 2015, [Online]. Available: <http://www.cephasonics.com>.
- [94] P. A. Hager, P. Vogel, A. Bartolini, and L. Benini, “Assessing the area/power/performance tradeoffs for an integrated fully-digital, large-scale 3d-ultrasound beamformer,” in *2014 IEEE Biomedical Circuits and Systems Conference (BioCAS) Proceedings*, Oct 2014, pp. 228–231.
- [95] S. Nikolov, J. Jensen, and B. Tomov, “Fast parametric beamformer for synthetic aperture imaging,” *IEEE Trans. Ultrason., Ferroelectr., Freq. Control.*, vol. 55, no. 8, pp. 1755–1767, August 2008.
- [96] J. Park, J. Lee, D.-H. Kim, M. Kim, J. H. Chang, T.-K. Song, and Y. Yoo, “Efficient implementation of a real-time dynamic synthetic aperture beamformer,” in *IEEE Symposium on Ultrasonics*, Oct 2012, pp. 2250–2253.

-
- [97] Philips Electronics N.V., “Philips iU22 ultrasound with xMATRIX system specifications,” 2012, [Online]. Available: <http://trisonics.com/ckfinder/userfiles/files/Philips%20iU22%20xMATRIX%20G-CART%20Specification.pdf>.
- [98] Koninklijke Philips Electronics N.V., “iE33 xMATRIX echocardiography system,” 2012, [Online]. Available: <http://www.snoveverestmm.com/pdf/Ultrasound/iE33-Brochure.pdf>.
- [99] GE Healthcare, “Voluson i,” 2017, [Online]. Available: http://www3.gehealthcare.co.uk/en-gb/products/categories/ultrasound/voluson/voluson_i.
- [100] Samsung Healthcare, “HM70A with plus,” 2017, [Online]. Available: <http://www.samsung.com/global/business/healthcare/healthcare/ultrasound/USS-HM7AF1K/WR>.
- [101] KPI Healthcare, “Samsung UGEO HM70A ultrasound machine,” 2017, [Online]. Available: <http://www.kpiultrasound.com/medical-equipment/ultrasound-scanners/samsung-ultrasound/samsung-ugeo-hm70a-portable/>.
- [102] —, “Samsung MySono U6 ultrasound machine,” 2017, [Online]. Available: <http://www.kpiultrasound.com/medical-equipment/ultrasound-scanners/samsung-ultrasound/samsung-mysono-u6-portable/>.
- [103] Chison Medical Imaging Co., Ltd., “Chison q9,” 2014, [Online]. Available: http://www.chison.com/products_detail.asp?id=168.
- [104] Philips Healthcare, “Cx50 xMATRIX,” 2017, [Online]. Available: <http://www.usa.philips.com/healthcare/product/HC795076CA/cx50-xmatrix-cardiology-ultrasound-machine>.
- [105] G. Wayne Moore, “Ultrasound beamformation and image reconstruction,” in the 51st American Association of Physicists in Medicine Annual Meeting (AAPM 2009), 2009, [Online]. Available: <https://vimeo.com/88175266>.
- [106] Cephasonics, “cQuest Griffin - Product Brief,” Catalog, 2015, [Online]. Available: http://pdf.medicalexpo.com/pdf/cephasonics/cquest-griffin/92255-171445-_2.html.
- [107] R. J. Tobias and M. E. Schafer, “System development improvements using stackable high-channel-count ultrasound hardware,” in *2014 IEEE International Ultrasonics Symposium (IUS 2014)*, Sept 2014.
- [108] “256 channel ultrasound image processing,” Xilinx Inc., 2018, [Online]. Available: <https://www.xilinx.com/applications/medical/256-channel-ultrasound.html>.
- [109] E. Boni, L. Bassi, A. Dallai, F. Guidi, V. Meacci, A. Ramalli, S. Ricci, and P. Tortoli, “ULA-OP 256: A 256-channel open scanner for development and real-time implementation of new ultrasound methods,” *IEEE Trans. Ultrason., Ferroelectr., Freq. Control.*, in press 2016.

Bibliography

- [110] R. Sampson, M. Yang, S. Wei, C. Chakrabarti, and T. Wenisch, "Sonic millipede: A massively parallel 3d-stacked accelerator for 3d ultrasound," in *High Performance Computer Architecture (HPCA2013), 2013 IEEE 19th International Symposium on*, Feb 2013, pp. 318–329.
- [111] R. Sampson, M. Yang, S. Wei, R. Jintamethasawat, B. Fowlkes, O. Kripfgans, C. Chakrabarti, and T. Wenisch, "FPGA implementation of low-power 3D ultrasound beamformer," in *2015 IEEE International Ultrasonics Symposium (IUS 2015)*, Nov 2015.
- [112] M. Tsakalakis and N. G. Bourbakis, "Designing of a low-cost, volumetric multi-transducer phased array ultrasound system," in *2015 IEEE 15th International Conference on Bioinformatics and Bioengineering (BIBE)*, Nov 2015, pp. 1–7.
- [113] Y.-J. Kim, S.-E. Cho, J.-Y. Um, M.-K. Chae, J. Bang, J. Song, T. Jeon, B. Kim, J.-Y. Sim, and H.-J. Park, "A single-chip 64-channel ultrasound RX-beamformer including analog front-end and an LUT for non-uniform ADC-sample-clock generation," *IEEE Transactions on Biomedical Circuits and Systems*, vol. PP, pp. 1 – 11, August 2016.
- [114] Y.-F. Li and P.-C. Li, "Software beamforming: Comparison between a phased array and synthetic transmit aperture," *Ultrasonic Imaging*, vol. 33, no. 2, pp. 109 – 118, April 2011.
- [115] B. Yiu, I. Tsang, and A. Yu, "GPU-based beamformer: fast realization of plane wave compounding and synthetic aperture imaging," *Ultrasonics, Ferroelectrics, and Frequency Control, IEEE Transactions on*, vol. 58, no. 8, pp. 1698–1705, August 2011.
- [116] J. Ma, K. Karadayi, M. Ali, and Y. Kim, "Ultrasound phase rotation beamforming on multi-core DSP," *Ultrasonics*, vol. 54, no. 1, pp. 99 – 105, January 2014.
- [117] C. Lee, H.-Y. Sohn, D.-H. Han, and T.-K. Song, "Real-time implementation of the echo signal processing and digital scan conversion for medical ultrasound imaging with a single TMS320C6416 DSP," in *Proceedings of SPIE - The International Society for Optical Engineering*, vol. 6920, March 2008.
- [118] D. N. Truong and B. M. Baas, "Massively parallel processor array for mid-/back-end ultrasound signal processing," in *2010 Biomedical Circuits and Systems Conference (BioCAS)*, Nov 2010, pp. 274–277.
- [119] C. Risser, H. J. Welsch, H. Fonfara, H. Hewener, and S. Tretbar, "High channel count ultrasound beamformer system with external multiplexer support for ultrafast 3D/4D ultrasound," in *2016 IEEE International Ultrasonics Symposium (IUS)*, Sept 2016, pp. 1–4.
- [120] P. A. Hager, A. Bartolini, and L. Benini, "Ekho: A 30.3w, 10k-channel fully digital integrated 3-d beamformer for medical ultrasound imaging achieving 298m focal points per second," *IEEE Transactions on Very Large Scale Integration (VLSI) Systems*, vol. 24, no. 5, pp. 1936–1949, May 2016.

- [121] R. E. Daigle, "Ultrasound imaging system with pixel oriented processing," Oct. 16 2012, US Patent 8,287,456.
- [122] "Matlab," The MathWorks, Inc., 2018, [Online]. Available: <https://ch.mathworks.com/products/matlab.html>.
- [123] MathWorks, *MATLAB version 9.1.0.441655 (R2016b)*, The MathWorks Inc., Natick, Massachusetts, United States, 2016.
- [124] "The first telesonography-capable system - source code: the matlab processing pipeline and the single-FPGA design," Integrated Systems Laboratory (LSI), École Polytechnique Fédérale de Lausanne (EPFL), 2018, [Online]. Available: <https://github.com/ibrahimaya/ustogo-lsi>.
- [125] J. Jensen, "Field: A program for simulating ultrasound systems," in *10th Nordic-Baltic Conference on Biomedical Imaging Published in Medical and Biological Engineering and Computing*, vol. 34, Supplement 1, 1996, pp. 351–353.
- [126] J. Jensen and N. Svendsen, "Calculation of pressure fields from arbitrarily shaped, apodized, and excited ultrasound transducers," *Ultrasonics, Ferroelectrics, and Frequency Control, IEEE Transactions on*, vol. 39, no. 2, pp. 262–267, March 1992.
- [127] J. A. Jensen, "A multi-threaded version of field ii," in *2014 IEEE International Ultrasonics Symposium*, Sept 2014, pp. 2229–2232.
- [128] S. Holm, "Digital beamforming in ultrasound imaging," in *proceedings Nordic Signal Processing Symposium*, June 1994.
- [129] D. DeTurck, "Power series and taylor series," University of Pennsylvania, 2018, [Online]. Available: <http://personal.ee.surrey.ac.uk/S.Gourley/series.pdf>.
- [130] S. Gourley, "Binomial expansion, power series, limits, approximations, fourier series," 2007, [Online]. Available: <http://personal.ee.surrey.ac.uk/S.Gourley/series.pdf>.
- [131] "Taylor expansion of $\sqrt{1 + x}$," PlanetMath, 2013, [Online]. Available: <http://planetmath.org/TaylorExpansionOfsqrt1x>.
- [132] A. Ibrahim, P. A. Hager, A. Bartolini, F. Angiolini, M. Arditì, L. Benini, and G. De Micheli, "Tackling the bottleneck of delay tables in 3D ultrasound imaging," in *Proceedings of the 2015 Design Automation and Test in Europe (DATE 2015) Conference*, March 2015, pp. 1683 – 1688.
- [133] I. K. Holfort, A. Austeng, J. Synnevåg, S. Holm, F. Gran, and J. A. Jensen, "Adaptive receive and transmit apodization for synthetic aperture ultrasound imaging," in *2009 IEEE International Ultrasonics Symposium*, Sept 2009, pp. 1–4.

Bibliography

- [134] J. Zhao, Y. Wang, X. Zeng, J. Yu, B. Y. S. Yiu, and A. C. H. Yu, "Plane wave compounding based on a joint transmitting-receiving adaptive beamformer," *IEEE Transactions on Ultrasonics, Ferroelectrics, and Frequency Control*, vol. 62, no. 8, pp. 1440–1452, August 2015.
- [135] C. H. Seo and J. T. Yen, "Sidelobe suppression in ultrasound imaging using dual apodization with cross-correlation," *IEEE Transactions on Ultrasonics, Ferroelectrics, and Frequency Control*, vol. 55, no. 10, pp. 2198–2210, October 2008.
- [136] J. Bhattacharyya, P. Mandal, R. Banerjee, and S. Banerjee, "Real time dynamic receive apodization for an ultrasound imaging system," in *VLSI Design, 2006. Held jointly with 5th International Conference on Embedded Systems and Design., 19th International Conference on*, Jan 2006, pp. 4 pp.–.
- [137] B. Tomov and J. Jensen, "Compact implementation of dynamic receive apodization in ultrasound scanners," in *Medical Imaging 2004, in Progress in Biomedical Optics and Imaging - Proceedings of SPIE*, Feb 2004, pp. 260–271.
- [138] A. Ibrahim, D. Doy, C. Loureiro, E. Pignat, F. Angiolini, M. Arditi, J.-P. Thiran, and G. De Micheli, "Inexpensive 1024-Channel 3D teleonography system on FPGA," in *Proceedings of the IEEE Biomedical Circuits and Systems Conference (BioCAS)*, 2017.
- [139] A. Ibrahim, W. Simon, D. Doy, E. Pignat, F. Angiolini, M. Arditi, J.-P. Thiran, and G. De Micheli, "Single-FPGA complete 3D and 2D medical ultrasound imager," in *Proceedings of the Conference on Design and Architectures for Signal and Image Processing (DASIP 2017)*, 2017.
- [140] Analog Devices Inc., "ADV7511: 225 mhz, high performance hdmi® transmitter with arc," 2017, [Online]. Available: <http://www.analog.com/en/products/audio-video/analoghdmidvi-interfaces/hdmidvi-transmitters/adv7511.html#product-overview>.
- [141] H. S. Søren K. Jespersen, Jens E. Wilhjelm, "Multi-angle compound imaging," *Ultrasonic Imaging*, vol. 20, no. 2, pp. 81–102, April 1998.
- [142] R. R. Entekin, B. A. Porter, H. H. Sillesen, A. D. Wong, P. L. Cooperberg, and C. H. Fix, "Real-time spatial compound imaging: Application to breast, vascular, and musculoskeletal ultrasound," *Seminars in Ultrasound, CT and MRI*, vol. 22, no. 1, pp. 50 – 64, 2001, [Online]. Available: <http://www.sciencedirect.com/science/article/pii/S0887217101900186>.
- [143] A. Perperidis, "Postprocessing approaches for the improvement of cardiac ultrasound b-mode images: A review," *IEEE Trans. Ultrason., Ferroelectr., Freq. Control.*, vol. 63, no. 3, pp. 470–485, March 2016.
- [144] H. G. Heng and W. R. Widmer, "Appearance of common ultrasound artifacts in conventional vs. spatial compound imaging," *Veterinary Radiology & Ultrasound*, vol. 51,

- no. 6, pp. 621–627, 2010, [Online]. Available: <https://onlinelibrary.wiley.com/doi/abs/10.1111/j.1740-8261.2010.01724.x>.
- [145] J. E. Wilhjelm, M. S. Jensen, S. K. Jespersen, B. Sahl, and E. Falk, “Visual and quantitative evaluation of selected image combination schemes in ultrasound spatial compound scanning,” *IEEE Transactions on Medical Imaging*, vol. 23, no. 2, pp. 181–190, Feb 2004.
- [146] Xilinx Inc., “Xilinx kintex ultraScale FPGA KCU105 evaluation kit,” 2017, [Online]. Available: <https://www.xilinx.com/products/boards-and-kits/kcu105.html>.
- [147] —, “Aurora 8B/10B,” 2017, [Online]. Available: <https://www.xilinx.com/products/intellectual-property/aurora8b10b.html>.
- [148] HiTech Global LLC, “2-port QSFP+ (40G or 56G) FMC module (vita57.1),” [Online]. Available: http://www.hitechglobal.com/FMCMModules/FMC_2QSFP+.htm.
- [149] Xilinx Inc., “Aurora 64B/66B,” 2017, [Online]. Available: <https://www.xilinx.com/products/intellectual-property/aurora64b66b.html>.
- [150] STMicroelectronics Inc., “iNemo-M1 System-On-Board,” 2017, [Online]. Available: <https://www.digikey.com/en/product-highlight/s/stmicroelectronics/inemo-m1-system-on-board>.
- [151] —, “INEMO-M1 Discovery: STEVAL-MKI121V1,” 2017, [Online]. Available: <http://www.st.com/en/evaluation-tools/steval-mki121v1.html>.
- [152] CHRobotics LLC., “Using accelerometers to estimate position and velocity,” [Online]. Available: <http://www.chrobotics.com/library/accel-position-velocity>.
- [153] x-io Technologies, “Open source IMU and AHRS algorithms,” 2012, [Online]. Available: <http://x-io.co.uk/open-source-imu-and-ahrs-algorithms/>.
- [154] S. Madgwick, A. Harrison, and R. Vaidyanathan, “Estimation of IMU and MARG orientation using a gradient descent algorithm,” in *Proceedings of the 2011 IEEE International Conference on Rehabilitation Robotics (ICORR)*, 2011.
- [155] Xilinx Inc., “Vivado,” 2018, [Online]. Available: <https://www.xilinx.com/support/university/vivado.html#overview>.
- [156] —, “Vivado design suite user guide: Getting started (v2017.2),” 2017, [Online]. Available: <http://www.farnell.com/datasheets/2353622.pdf>.
- [157] —, “Vivado design suite tutorial: Power analysis and optimization,” 2017, [Online]. Available: https://www.xilinx.com/support/documentation/sw_manuals/xilinx2017_2/ug997-vivado-power-analysis-optimization-tutorial.pdf.
- [158] —, “Best practices for ultraScale power measurement using the KCU105,” [Online]. Available: <https://www.xilinx.com/video/fpga/best-practices-ultrascale-power-kcu105.html>.

Bibliography

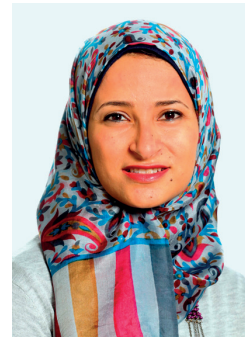
- [159] M. D'Urbino, C. Chen, Z. Chen, Z. Chang, J. Ponte, B. Lippe, and M. Pertijs, "An element-matched electromechanical $\Delta\Sigma$ ADC for ultrasound imaging," *IEEE Journal of Solid-State Circuits*, vol. 53, no. 10, pp. 2795–2805, Oct 2018.
- [160] L. S. Smith, R. S. Lewandowski, B. H. Haider, C. E. Baumgartner, G. C. Sogoian, C. S. Yetter, D. G. Wildes, S. R. Kaiser, S. Bergstoel, R. Bruestle, T. Icoz, S. Bjaerum, and C. F. Saj, "System and method for actively cooling an ultrasound probe," Jul. 2 2013, US Patent 8,475,375B2.
- [161] R. E. Davidsen, S. R. Freeman, and B. J. Savord, "Matrix ultrasound probe with passive heat dissipation," Aug. 15 2017, US Patent 9,730,677B2.
- [162] R. E. Davidson, M. Scarsela, J. C. Taylor, and A. L. Robinson, "Ultrasonic matrix array probe with thermally dissipating cable," Jan. 16 2018, US Patent 9,867,592B2.
- [163] H. Risbakk, "Cooling of transducer array used for ultrasound radiation force," *NTNU PhD Dissertation*, 2015.
- [164] "Kinect for windows," Microsoft, 2018, [Online]. Available: <https://developer.microsoft.com/en-us/windows/kinect>.
- [165] Virtopsy Project, "Virtopsy - potential use of gesture control in medicine using the microsoft kinect camera," Institute of Forensic Medicine, University of Bern, Switzerland, 2010, [Online]. Available: <https://www.youtube.com/watch?v=b6CT-YDChmE>.
- [166] "Virtopsy," Institute of Forensic Medicine, University of Bern, Switzerland, [Online]. Available: <https://virtopsy.com/about-virtopsy/>.
- [167] J. B. Hill, "Calculus - notes on taylor polynomial error bounds," Department of Mathematics - University of Colorado, 2010, [Online]. Available: http://math.jasonbhill.com/sites/default/files/fall2010math2300_10-4-error-bounds-notes.pdf.
- [168] "Lagrange remainder," Wolfram Mathworld, 2018, [Online]. Available: <http://mathworld.wolfram.com/LagrangeRemainder.html>.

AYA IBRAHIM

Rue de Crissier 3b · CH-1020 Renens · VAUD · Switzerland · (+41) 0788-989-086

PERSONAL

BIRTH October 5, 1988
NATIONALITY Egyptian
GENDER Female
RESIDENCE Renens · Vaud · Switzerland (B permit)
E-MAIL aya.naguib.ibrahim@gmail.com, aya.ibrahim@epfl.ch
LINKEDIN [Aya Ibrahim](#)
ORCID ID <https://orcid.org/0000-0001-9548-2433>
GOOGLE SCHOLAR [Aya Ibrahim](#)
SKYPE [aya_m._naguib](#)
PHONE (+41) 0788-989-086



AWARDS AND HONORS

- **Winner - Xilinx University Competition 2018:** “First Telesonography-Capable System: First Single-FPGA, 5 Watt, and Inexpensive, 1024-channel Medical 3D and 2D Ultrasound Imager” project, Xilinx Open Hardware Design Competition 2018, PhD category.
- **Best Paper Award:** “Single-FPGA Complete 3D and 2D Medical Ultrasound Imager” paper (first author) in the 2017 Design and Architectures for Signal and Image Processing (DASIP 2017) Conference, Germany.
- **Bronze Leaf Award:** “Apodization Scheme for Hardware-Efficient Beamformer” paper (first author) in the 12th Conference on PhD Research in Microelectronics and Electronics (PRIME 2016), Portugal.

FIELDS OF EXPERIENCE AND INTEREST

Image and Signal Processing	Image Analysis	Biomedical Systems
Low-power HW/SW Co-design	Medical Imaging (especially Ultrasound)	

TECHNICAL SKILLS

PROGRAMMING LANGUAGES	Matlab, C, C#, Java, Python, PHP, HTML
EMBEDDED SYSTEMS	VHDL, Verilog, FPGA, Microcontrollers
IDEs	Xilinx Vivado, Xilinx SDK, Microsoft Visual Studio, Android Studio, Netbeans, and Eclipse
OSes	Microsoft, Macintosh, and Linux OS
TYPOGRAPHY	Latex, and Microsoft Office
OTHERS	Git, Omnigraffle, SQL, MySQL, and Microsoft project

TRANSFERABLE SKILLS

Research Skills	Communication Skills	Teamwork Skills	Commitment
Persistence	Time Management	Presentation Skills	Resilience

LANGUAGES

ENGLISH	C1
FRENCH	A2
ARABIC	Mother tongue

EDUCATION AND ACADEMIC DEGREES

Ph.D. Electrical Engineering

October 2014 · October 2018

Integrated Systems Laboratory · School of Electrical Engineering · École Polytechnique Fédérale de Lausanne (EPFL)
Lausanne · Switzerland

Thesis Title: 3-Dimensional Ultrasound Imaging For Medical Telesonography: Algorithms and Architectures

Supervisors : Prof. Giovanni De Micheli and Dr. Federico Angiolini

Summary : The Ph.D. aims to develop a portable, low-power, and affordable 3D medical ultrasound imaging system that enables for the first time telemedicine in ultrasound. This has been successfully achieved by proposing smart algorithms, efficient techniques, and optimized implementation that lead to an unprecedented prototype; portable and inexpensive, supports 1024-channel (state-of-the-art) processing, and operates in battery-power budget. The Ph.D. research results in 2 awards, a winning project, 2 journal papers, 11 conference papers, 5 demo-night presentations, and video recording to the media.

M.Sc. Biomedical Engineering

September 2010 · September 2013

Systems and Biomedical Engineering Department · School of Engineering · Cairo University
Cairo · Egypt

GPA : 3.73/4.0 · Distinction with Honors

Thesis Title: Retrieval of Color Fundus Images Based on Their Content of Diabetic Macular Edema

Supervisors : Prof. Bassel S. Tawfik and Assoc. Prof. Ahmed S. Fahmy

Summary : The thesis aim was to develop a Content Based Image Retrieval (CBIR) system that retrieves color fundus images of diabetic macular edema based on the quantity and location of exudates. The macula has been segmented into three concentric regions; fovea, parafovea and perifovea, instead of working on the macula as a whole. The proposed approach of dividing the macula into several regions, the developed feature vector, and the multistage retrieval criterion enhance the performance of retinal CBIR systems. The thesis results in 1 conference paper.

B.Sc. Biomedical Engineering

September 2005 · July 2010

Systems and Biomedical Engineering Department · School of Engineering · Cairo University
Cairo · Egypt

GPA : 3.89/4.0 · Distinction with Honors (Rank: 3rd/200)

Thesis Title: Management of Woman Healthcare via the Use of Google Health Platform and Smart Pen Technology

Supervisor : Assoc. Prof. Ahmed A. Morsy

PREVIOUS TRAINING AND WORKSHOPS

- **Teaching Assistant:** Image Processing · Medical Equipment · Ultrasound Physics · Biophysics · Electrical Circuits (Lab) · EDA Lab · Measurements.
- **Courses:** Advanced Biomedical Imaging Methods and Instrumentation · Practical Aspects In Mixed-Signal Design · Co-design of Systems-on-Chip on Reconfigurable Hardware · Design Technologies for Integrated Systems.
- Trained at the Integrated Systems Laboratory (LSI), EPFL, Switzerland (April - Sept., 2014).
- Trained at Bio-Business company (July - Aug., 2009).
- Trained at Childrens Cancer Hospital Egypt CCHE 75375 (June - Aug. 2008).
- Trained at National Research Centre in Egypt - Engineering Research Division (July, 2007).

INTERNATIONAL EVENTS ORGANIZATION AND VOLUNTEERING WORK

- Shared on the organization of The Emerging Trends in Computing Symposium 2016, Montreux, Switzerland.
- A session chair on The First IEEE EMBS International Students Conference, Cairo, Egypt (Oct., 2013).
- Shared on the organization of 4th, 5th and 6th Cairo International Biomedical Engineering Conference CIBEC 2008, CIBEC 2010 and CIBEC 2012.
- Member in Kiva non-profit organization (2015 - currently). Member in Resala association for charity in 2007 and 2008.

Journal Papers:

1. A. Ibrahim, P. A. Hager, A. Bartolini, F. Angiolini, M. Arditi, J.-P. Thiran, L. Benini, and G. De Micheli, "Towards Ultrasound Everywhere: A Portable 3D Digital Back-End Capable of Zone and Compound Imaging", *In IEEE Transactions on Biomedical Circuits and Systems (TBioCAS)*, vol. 12, no. 5, pp. 968-981, 2018.
2. A. Ibrahim, P. A. Hager, A. Bartolini, F. Angiolini, M. Arditi, J.-P. Thiran, L. Benini, and G. De Micheli, "Efficient sample delay calculation for 2D and 3D ultrasound imaging", *In IEEE Transactions on Biomedical Circuits and Systems (TBioCAS)*, vol 11, no 4, pp. 815-831, August 2017.

Conference Papers:

1. A. Ibrahim, W. Simon, D. Doy, E. Pignat, F. Angiolini, M. Arditi, J.-P. Thiran, and G. De Micheli, "Single-FPGA complete 3D and 2D medical ultrasound imager", *In The Proceedings of the 2017 Design and Architectures for Signal and Image Processing (DASIP 2017) Conference*, Germany.
2. A. Ibrahim, D. Doy, C. Loureiro, E. Pignat, F. Angiolini, M. Arditi, J.-P. Thiran, and G. De Micheli, "Inexpensive 1024-Channel 3D Telesonography System on FPGA", *In The Proceedings of the 2017 IEEE Biomedical Circuits and Systems (BioCAS 2017) Conference*, Italy.
3. F. Angiolini, A. Ibrahim, W. Simon, A.C. Yüzügüler, M. Arditi, J.-P. Thiran, and G. De Micheli, "1024-Channel 3D Ultrasound Digital Beamformer in a Single 5W FPGA", *In The Proceedings of the 2017 Design Automation and Test in Europe (DATE 2017) Conference*, Switzerland.
4. A. Ibrahim, W. Simon, A.C. Yüzügüler, F. Angiolini, M. Arditi, J.-P. Thiran, and G. De Micheli, "1024-Channel Single 5W FPGA Towards High-quality Portable 3D Ultrasound Platform", *A PhD-Forum Paper In the 2017 Design Automation and Test in Europe (DATE 2017) Conference*, Switzerland.
5. A. Ibrahim, F. Angiolini, M. Arditi, J.-P. Thiran, and G. De Micheli, "Apodization scheme for hardware-efficient beamformer", *In The Proceedings of the 12th Conference on PhD Research in Microelectronics and Electronics (PRIME 2016)*, Portugal.
6. A. C. Yüzügüler, W. Simon, A. Ibrahim, F. Angiolini, M. Arditi, J.-P. Thiran, and G. De Micheli, "Demo: Efficient Delay and Apodization for on-FPGA 3D Ultrasound", *A Demo-Night Paper In the 2016 Design and Architectures for Signal and Image Processing (DASIP 2016) Conference*, France.
7. W. Simon, A. C. Yüzügüler, A. Ibrahim, F. Angiolini, M. Arditi, J.-P. Thiran, and G. De Micheli, "Single-FPGA, scalable, low-power, and high- quality 3D ultrasound beamformer", *A PhD-Forum Paper In The 26th International Conference on Field-Programmable Logic and Applications (FPL 2016)*, Switzerland.
8. A. C. Yüzügüler, W. Simon, A. Ibrahim, F. Angiolini, M. Arditi, J.-P. Thiran, and G. De Micheli, "Single-FPGA 3D ultrasound beamformer", *A Demo-Night Paper in the 26th International Conference on Field-Programmable Logic and Applications (FPL 2016)*, Switzerland.
9. A. Ibrahim, A. Simalatsar, S. Skalistis, F. Angiolini, M. Arditi, J.-P. Thiran, G. De Micheli, "Assessment of image quality vs. computation cost for different parameterizations of ultrasound imaging pipelines", *The 6th Workshop on Medical Cyber-Physical Systems*, 2015, USA.
10. A. Ibrahim, P. A. Hager, A. Bartolini, F. Angiolini, M. Arditi, L. Benini, and G. De Micheli, "Tackling the bottleneck of delay tables in 3D ultrasound imaging", *In The Proceedings of the 2015 Design Automation and Test in Europe (DATE 2015) Conference*, France.
11. Aya M. Naguib, Ahmed M. Ghanem and Ahmed S. Fahmy, "Content Based Image Retrieval of Diabetic Macular Edema Images", *In The 26th IEEE International Symposium on Computer-Based Medical Systems (CBMS 2013)*, Portugal.

Open Access Code:

1. Complete matlab US imaging pipeline for 2D (linear and phased) and 3D (phased) imaging: <https://github.com/ibrahimaya/ustogo-lsi>
2. Complete single-FPGA design including both the hardware side (two custom IPs and top-level block design) and the software side (MicroBlaze controller software and C#-based GUI): <https://github.com/ibrahimaya/ustogo-lsi>

Demo Recordings:

1. *UltrasoundToGo* project demo recording to the media - EPFL (Aya Ibrahim) and ETHZ (Pascal Hager): <https://www.youtube.com/watch?v=onD8atJ7EHk&t=2s>
2. *First single-FPGA digital 3D US imager* - Xilinx Open Hardware 2018 Competition recording: <https://www.youtube.com/watch?v=Z-K2kl7vwzs>